Constitutive Behaviour and Formability of Pre-aged AA7075 Sheet in a Warm Forming Process

By

Hossein Pishyar

A thesis
presented to the University of Waterloo
in fulfillment of the
thesis requirement for the degree of
Master of Applied Science
in
Mechanical and Mechatronics Engineering

Waterloo, Ontario, Canada, 2021

Author’s Declaration

I hereby declare that I am the sole author of this thesis. This is a true copy of the thesis, including any required final revisions, as accepted by my examiners.

I understand that my thesis may be made electronically available to the public.

Abstract

Warm constitutive and formability characterization of a high strength aluminum alloy (AA7075) was performed for a range of pre-aged (*i.e.* under-aged) tempers, strain rates and temperatures. The pre-aging processes were composed of a solution treatment process and a natural aging period of 2 days, followed by aging at temperatures of 80, 100 and 120 °C for durations of 1, 2, and 4 hours. The peak-aged T6 temper condition was also considered for comparison purposes.

Warm constitutive characterization was performed at strain rates of 0.01, 0.1, and 1 s^{-1}, and temperatures of 150, 175 and 200 °C. Room temperature and warm formability tests were performed using a Nakazima [1] tooling geometry with a plane strain specimen for the same temperatures, considering a range of tooling stroke rates from 0.5-63 mm/s. The formability results were assessed utilizing limit strains based on the ISO 12004-2:2008 [2] necking detection method, as well as the measured dome heights at failure. In addition, the effect of heating rate prior to elevated temperature constitutive and formability testing was considered.

The room temperature constitutive results revealed that the pre-aged tempers exhibit superior work hardening response and elongation compared to the peak-aged T6 temper. However, serrated flow, attributed to PLC effects, was observed in the flow response of the tempers with reduced/insufficient pre-aging schedules (*e.g.* 1 hour at 80 and 100 °C pre-age schedules). This behaviour induced a negative strain rate sensitivity and reduced the repeatability of the tensile flow response and room temperature formability limits.

In response to elevated temperature deformation, the T6 tensile samples exhibited clear thermal softening effects. This response, however, was accompanied by early onset of diffuse necking, although the elevated temperature strain rate sensitivity is high which results in increased elongation to failure. The pre-aged tempers, in contrast, also responded positively to the thermal softening effect and exhibited a delay in the onset of diffuse necking, compared to T6. Interestingly, the elevated temperature strain rate sensitivity of the pre-aged tempers was quite low compared to the T6 samples, part of which is attributed to aging during the lower rate (longer duration) tensile tests.

The room temperature formability results revealed improvements in forming limits with the pre-aged tempers, as compared to the peak-aged T6 temper. At elevated temperatures, thermal softening resulted in higher forming limits for all evaluated tempers, with the T6 temper at 200 °C having the highest limit strain, closely followed by the 100 °C 4 hour and 80 °C 4 hour aged tempers formed at 175 °C. Interestingly, the high limit strain exhibited by the warm formed T6 temper was not fully reflected in its limit dome height, since the early onset of diffuse necking prevented a globally uniform strain distribution along the surface of the specimen. In contrast, the pre-aged tempers in contrast resulted in superior dome height limits, which is attributed to their higher extent of work hardening prior to onset of diffuse necking.

Both the tensile elongation and forming limit strains were shown to decrease with test speed. Further, the faster heating rates considered in this study resulted in mildly superior forming limits, since the extent of pre-aging during heating to the warm forming temperatures was reduced.

A limited study on the hardness of the warm formed specimens before and after a paint bake cycle (PBC) revealed a notable increase in hardness values in response to the PBC for all tested conditions. Interestingly, the T6 temper exhibited a mild drop in hardness following warm forming, however, the loss in hardness was largely recovered after the PBC, which may be due to retrogression and re-aging effects.

For the range of initial tempers and forming conditions considered herein, the specimens heat-treated at 100 °C for 4 hours, and warm formed at 175 °C (utilizing the rapid heating method) resulted in one of the best overall performances. This process route (evaluated at the slow forming speeds of 1 mm/s) resulted in an increase of approximately 42% in dome height (from 19 to 27 mm), and 77% in major limit strain (from 14.5 to 25.7%), compared to the room temperature limits of the T6 temper. Moreover, the repeatability of this process route proved to be superior compared to the majority of the other under-aged processing routes. In addition, the hardness values of this pre-aged temper, following warm forming and a paint bake cycle (PBC) were within 97% of the as-received T6 temper.

Finally, a numerical model was devised, using the Hockett-Sherby [3] constitutive model to fit the warm tensile data. The numerical simulations demonstrated accurate predictions for the tensile experiments and fair predictions for the warm forming experiments.

Acknowledgements

The work done in this thesis would not have been possible without the help and guidance of the members of the forming and crash lab and the engineering technical teams at the University of Waterloo. First and foremost, I would like to profoundly thank my supervisor, Professor Michael Worswick, for granting me an excellent opportunity to take part in this industrial project. During my studies, he provided exceptional support and contributed significantly to a rewarding experience. His openness for novel and exciting solutions, or at times ventures, has provided a rare and delightful experience. Additionally, I wish to express my gratitude to Professor Clifford Butcher for sharing his vast knowledge, expertise and tools in the field of constitutive modelling and material characterization.

I would like to extend my sincere thanks to Ryan George, his guidance and experimental expertise in the lab with the design and integration of the new apparatuses helped me vastly. This thesis has also benefited greatly from the assistance of Kenneth Wong through experimental analysis of the warm forming tests, especially during the time of limited access to the lab due to the current pandemic. The warm forming experiments were also performed with the help of Ryan and Kenneth, and I take this opportunity to thank them.

I must also thank Jaqueline Noder, and Amir Zhumagulov for all their generous help with the other experimental work. Jacqueline, thank you for being my lab-buddy, and helping me complete my experiments in a timely manner. Additionally, Mark Whitney has provided tremendous support with the Gleeble apparatus, teaching me everything I needed to know to fly solo.

I am deeply thankful to Professor Shahrzad Esmaeili and her team, Negar Baghbanaghaie and Atekeh Abolhasani who helped me gain a deeper understanding of the precipitation behaviour of the alloys. I also wish to thank Massimo DiCiano and Sante DiCecco for getting me ramped up on this project. Sante was of great help, especially when time was of essence! Many thanks to the offline support from Pedram Samadian, Jaqueline Noder, Armin Abedini, Cameron Tolton and Taamjeed Rahmaan who have aided me throughout my theoretical and numerical studies which helped me gain a deeper understanding of my research topic.

I gratefully acknowledge the efforts of Eckhard Budziarek, we worked together on a lot of unique projects in the lab, some of them flourished and became standard for experimental procedures. It was a pleasure working alongside my friends and colleagues Raphael Boulis, Steven Lee, Matthew Tummers,

Stan Lu, Reza Tangestani, Ahmed Ibrahim, Zohreh Asaee, Dylan Budnick, Farzad Sharifpour, Farinaz Jeyranpourkhameneh, and Ramin Chitsaz - thank you for the great times. Thanks also to Tom Gawel, Mark Kuntz, Andy Barber, Neil Griffett and Richard Gordon for sharing their technical expertise in the lab.

I also want to recognize the financial and technical support provided from our industrial supporters, Honda R&D Americas Inc., Arconic Group, and Promatek Research Centre (Magna), as well as from the Natural Sciences and Engineering Research Council, Ontario Centres for Excellence and the Ontario Advanced Manufacturing Consortium.

Last but not least, I would like to thank my parents (Mohammad and Azar) and my siblings (Paria, Sara, and Maria) for their support during my studies. Moreover, I want to express my appreciation to my amazing partner, Yara Khalaf, for the love and support throughout the ups and downs as a grad student.

Dedication

To my parents. I hope this achievement satisfies the dream of a better future you had in mind for me.

Table of Contents

List of Figures

List of Tables

1. Introduction

Global warming and climate change remain as one of the most critical challenges of this generation, and perhaps generations to come [1]. Canada has been at the forefront of awareness campaigns and has established several initiatives in various fields to mitigate the further worsening of global warming and climate change, as set by Canada's greenhouse gas emission regulations [2], [3].

Figure 1 and Figure 2 display the historical development of carbon dioxide emissions over the past thirty years. Figure 1 shows the sector-wise distribution of CO_2 emissions in Canada, which highlights the increasing emissions due to transportation in Canada. Further, Figure 2 depicts the emissions caused by each fuel source, with oil being the increasingly higher pollutant.

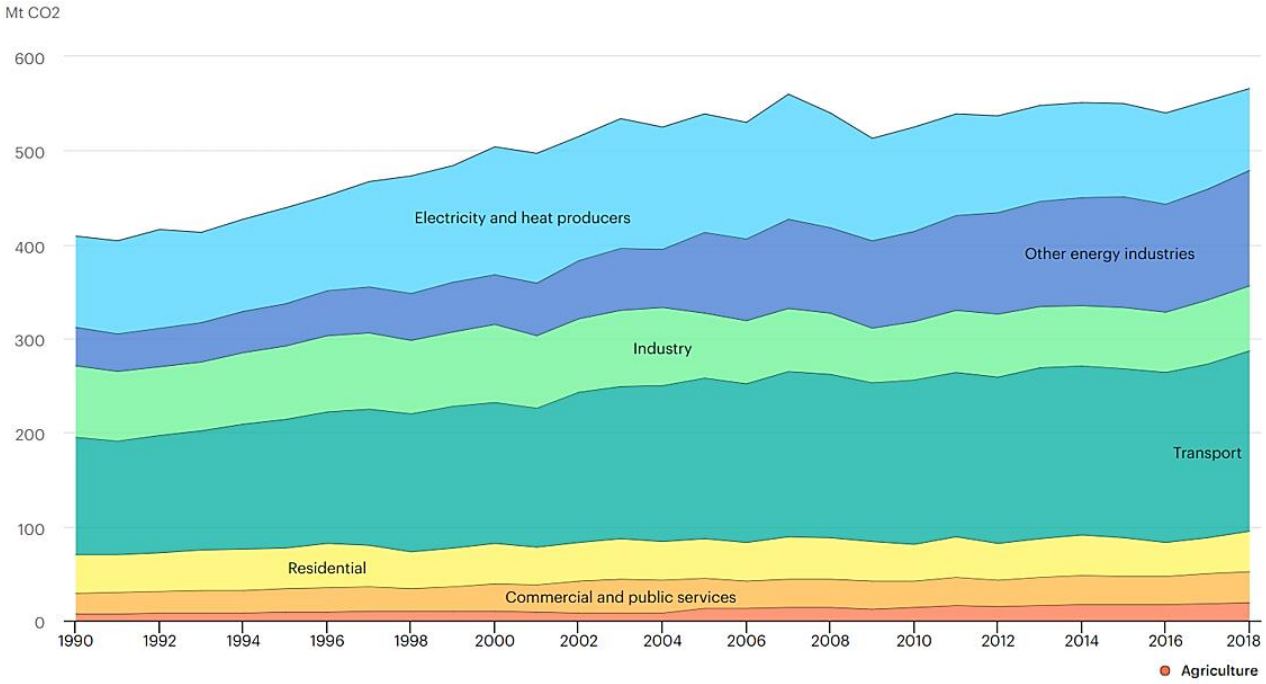

Figure 1. Canada's CO_2 emissions produced in different sectors [4].

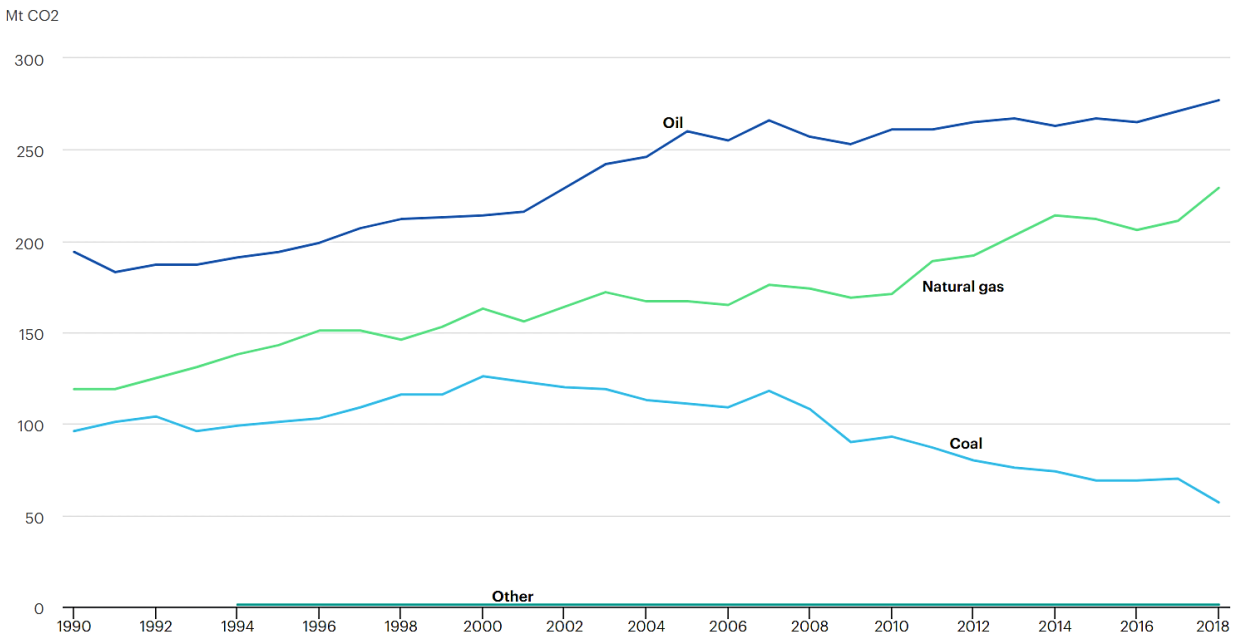

Figure 2. Canada's CO2 emissions produced from different energy sources [4].

Furthermore, Canada and the US are ranked last globally, amongst 50 participating countries, in vehicle efficiency [5]. This is associated with factors such as the vast landscape, climate, urban design, and demographics. Figure 3 lists the top 15 countries as characterized by a) Emissions in gCO_2/km, b) Fuel consumption in L/100km, c) Curb weight in kg, and d) Engine displacement in cm^3. As can be seen, the United States and Canada are the bottom two in each of the four charts, indicating that the heaviest vehicles are being used, powered by the largest engines, producing the most greenhouse gas.

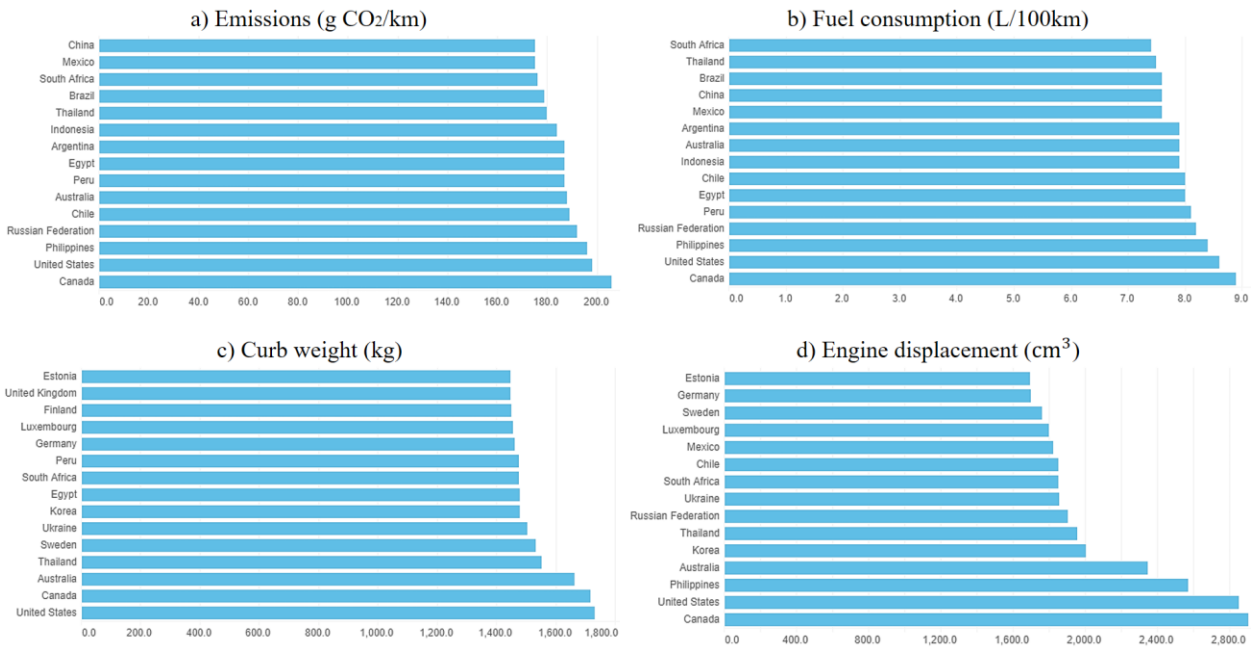

Figure 3. Top 15 countries listed by the characteristics of the average personal vehicles [5] ,[6].

This trend is further worsened by the recent growing consumer demand for larger vehicles. Data from Statistics Canada, Figure 4, shows the rapid upsurge in the number of newly registered trucks, increasing from 50% to 70% of total newly registered vehicles across Canada. The division labelled as trucks includes light and heavy trucks, sport-utility vehicles (SUVs), minivans, vans, and buses.

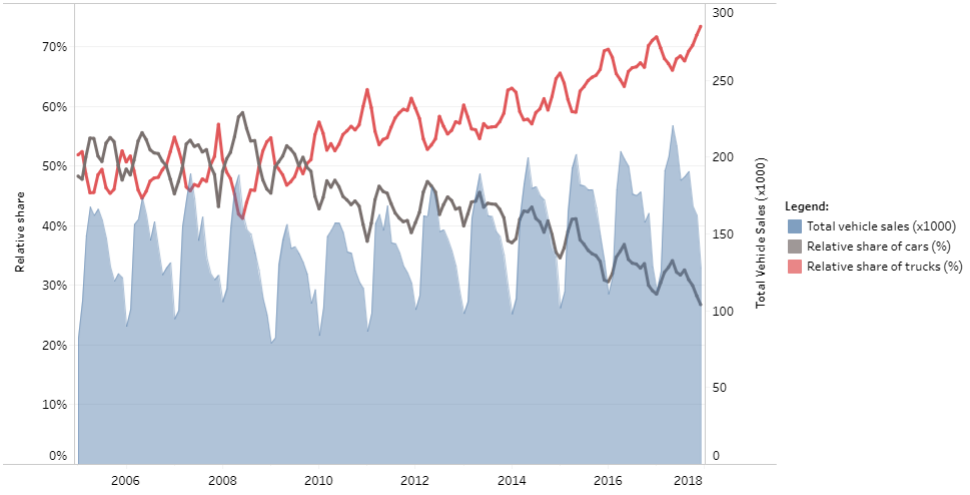

Figure 4. The total number of new vehicles and the relative comparison between consumer cars and trucks [7] [8].

In response, Canada's fuel consumption of light-duty vehicles is set to be reduced by approximately 40% over the period 2011 to 2025, which is in line with the US CAFE [9] goals of

reducing the fuel consumption of road vehicles in an effort to alleviate the concerns raised by global warming [10], [11]. Figure 5 displays the calculated trend in fuel consumption as expected to be achieved by 2025.

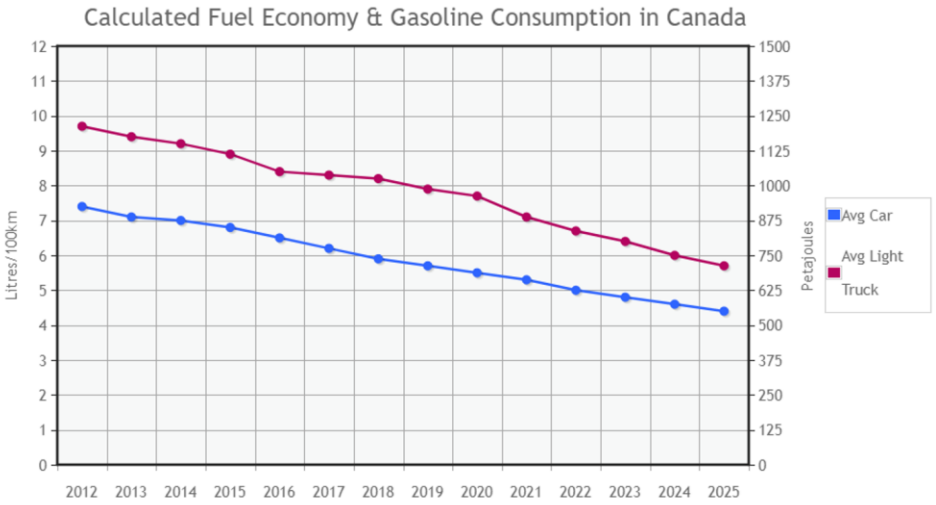

Figure 5. Calculated fuel consumption of cars and trucks across Canada [12] [13] [14].

With the abovementioned goals in mind, two primary paths can be taken: (i) altering the fuel source (propulsion systems); or (ii) improving the general efficiency of the vehicle. The first path has been a subject of substantial interest in the automotive industry but requires more time and effort to achieve energy storage density and accessibility similar to that of current fossil-fuel powered propulsion systems.

The second path can be achieved by improving various factors such as the aerodynamics of the exterior shell, drivetrain, vehicle autonomy, and a major contributor, the overall weight of the vehicle [15].

A study by the International Energy Agency (IEA), Figure 6, displays the relationship between fuel consumption and vehicle weight, for the common powertrains in the market. It is shown that an increase of curb weight corresponds to an exponential increase of fuel consumption for the fossil fuel based propulsion systems.

Moreover, despite the reduced effect of curb weight on the overall emissions of the electric vehicles (EVs) - partly owing to the regenerative technologies [16], EVs can also benefit from a

reduction in body weight. The lowered center of gravity helps with the general driving and handling experience, and more importantly provides additional passive safety improvements (*e.g.* rollover) [17]. Also, the reduced weight can help compensate the added battery weight to gain further range, resulting in an improved practicality for a wide range of consumers [18].

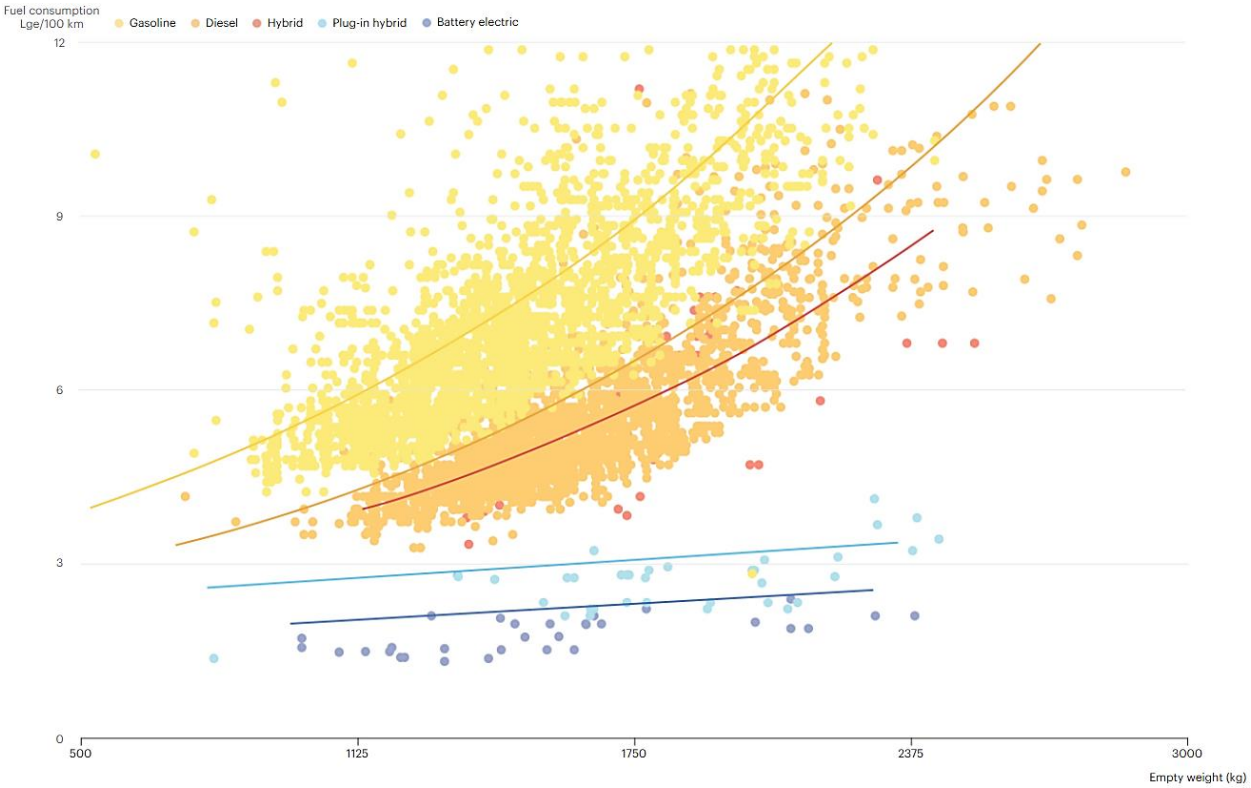

Figure 6. Automobile fuel consumption vs. vehicle weight for the different powertrains in 2017 [19].

The body structures of automobiles, which comprises approximately 35% of the total curb weight [20], has been an appealing candidate to consider for weight reduction. In this regard, the substitution of lighter materials, such as high strength grades of aluminum alloys, for heavy steels in car bodies has become more prevalent amongst automakers. Needless to say, such implementation must also uphold the overall comfort and safety requirements associated with modern vehicles.

Being the most abundant metallic element on earth, aluminum was initially introduced as a symbol of luxury due to its refinement complexities from ore [21], [22]. Henri Sainte-Claire Deville [23], a chemist involved in the rapid refinement of aluminum, aware of the great potentials of the industrialization of this new metal, has reportedly said:

"There is nothing more difficult than to make people use a new metal. Luxury items and ornaments cannot be the only sphere of its application. I hope the time will come when aluminum will serve to satisfy the needs of daily application" [24].

Consequently, upon the development of its rapid and cost-effective purification methods in the late 1800s, the first industry to flourish from its excellent formability (ability of the material to be formed to the desired shapes without visible defects) and density characteristics, was the culinary industry. At the time, the majority of the manufactured aluminum products were utensils and cookware [25].

It was not until the early 1900s when Wilm [26] evaluated the age hardening behaviour of aluminum alloys, determining the excellent strength potentials of this element. Wilm saw that after quenching, a widely known process for hardening iron alloys, given some 'aging' time, aluminum alloys develop further strength. This process was later referred to as precipitation (or age) hardening.

The discovery of this behaviour promoted great interest in aluminum since it had a much better strength-to-weight ratio compared to common steels, with other inherent advantages such as superior electrical and thermal conductivity and better corrosion resistance for a variety of new applications and industries, most predominantly aeronautics and astronautics, and recently, the automotive industry. Furthermore, given the relatively higher cost of this metal, the ease of recyclability has also proven to be advantageous. Such characteristics have improved with further efforts in the development of new alloys of aluminum and continue to enable the industry to reach new milestones with today's evolving world.

High strength 7000-series aluminum alloys have been shown to exhibit higher specific strength, the ratio of tensile strength to density, than the majority of commonly-used steels in industry, since they have one-third the density of steel. In the automotive industry, it has been calculated that if every 2 kg of steel were to be replaced by 1 kg of aluminum, a reduction of approximately 10 kg in CO_2 emissions over the average life cycle of vehicles will result [27]. Thus, the 7000-series alloys are a compelling option, even compared to the current automotive aluminum solutions which predominantly employ 5000- and 6000-series alloys.

However, at their peak strength, the AA7000-series aluminum alloys display relatively low formability, as shown in several studies by Wang *et al.* [28], Sotirov *et al.* [29], Polak *et al.* [30] and Österreicher *et al.* [31]. This drawback has been a topic of research in the industry and academe during the past few decades. The current study aims to address this problem for one of the well-established and widely-used alloys in the 7000-series designation, namely, AA7075.

The formability enhancing warm-forming process, as one of the most prevalent solutions, is the focus of the current work. This process takes advantage of the thermal softening response of aluminum alloys at temperatures above 150 °C and below the recrystallization temperature [29]. Additionally, the pre-aged (or partially heat-treated) conditions of this alloy (AA7075), previously examined by Österreicher *et al.* [31] and Lee *et al.* [32] with some promising results, will be considered in this thesis.

This research will focus on understanding the effect of warm forming of pre-aged tempers, in conjunction with rapid heating and rapid forming techniques, on the formability of AA7075. Efforts are made to identify desirable thermo-mechanical processing routes for this alloys. As part of the constitutive response evaluation, the alloy is characterized during warm forming. Lastly, the effect of the processing route on the final hardness (strength) is assessed.

The balance of this thesis is organized as follows. Chapter 2 presents a concise literature review addressing the constitutive and precipitation hardening behaviour of this alloy and explores recent efforts in evaluating and resolving the formability concerns with this alloy series. Chapter 3 provides a brief description of experimental procedures and equipment along with some background information on the AA7075 alloy under analysis; Chapter 4 presents results on the measured constitutive behaviour for each temper, temperature and strain rate, providing constitutive models for some selected conditions; Chapter 5 presents a numerical simulation study to evaluate the constitutive models, supported by experimental validation; and finally Chapter 6 provides the conclusions drawn from this research and presents an optimal forming process route satisfying the formability and final strength enhancement goals as set forth for this thesis. Additional information on specific setup calibrations, troubleshooting and description of corrective measures is provided in the appendices.

2. Literature Review

The outstanding specific strength of AA7075 aluminum alloy sheet has led to consideration of its application for use in anti-intrusion components within the automotive industry. However, to justify the implementation, various factors should be taken into account, such as the manufacturability, the in-service strength and the stability of the final temper.

This chapter provides a summary of the relevant literature concerning the aging response, and constitutive and formability characterization of AA7075 aluminum alloy sheet, in response to various forming process routes. The precipitation behaviour is studied to evaluate the aging response as a function of processing time, temperature and deformation (associated with warm forming processes). Further, the current literature constitutive characterization and modeling efforts for this alloy are also presented as a function of temperature and plastic deformation for multiple temper conditions of this alloy. Lastly, some existing studies are presented to outline the current findings of the formability response of this alloy and the advantages and drawbacks of the various formability improvement approaches.

2.1. Metallurgy and Mechanics of Precipitate Hardening in 7000-Series Aluminum Alloys

Aluminum matrix is comprised of a face centred cubic arrangement of atoms with 12 slip systems promoting enhanced formability [33]. With the addition of small amounts of alloying elements and an age-hardening cycle, the alloys can gain a considerable amount of strength as compared to pure aluminum.

Precipitation (or age) hardening is a result of a phenomenon in which finely-distributed particles, present in the base matrix of the alloy material, provide resistance to material deformation by blocking dislocation motion. It has been shown that depending upon the precipitation hardening heat treatment cycles, the Al-Zn-Mg (7000-series aluminum) alloys exhibit a substantial increase in mechanical strength as a consequence of precipitate formation in

the matrix of the alloy [34]. The following sections will discuss the nature of such response in 7000-series aluminum alloys from metallurgical and mechanical viewpoints.

2.1.1. Phase Transformation

The phase transformation of 7000-series aluminum alloys during aging is comprised of a multi-step precipitate formation and evolution. The precipitation sequence is generally described as: Supersaturated Solid Solution (SSS) $\rightarrow$ Guinier-Preston (G.P.) zones $\rightarrow \eta'$ (MgZn) $\rightarrow \eta$ ($MgZn_2$) [35], in which each state leads to a more stable *(in terms of aging)* and, therefore, a lower free energy condition [32], [36].

The aforementioned multi-step phase transformation is initiated by the solution treatment process, in which the temperature of the sample is increased to the solution treatment temperature, *i.e.* 470 °C in the case of 7000-series aluminum [36]. This treatment causes existing precipitates (mainly comprised of Zn and Mg) to dissolve within the aluminum matrix. Solution treatment is followed by a rapid reduction of the temperature (*i.e.* water-quenching), resulting in a supersaturated state for both vacancies and solute atoms. This state is referred to as the Supersaturated Solution State (SSS), which has a high thermodynamic potential to form fine precipitates. Following the solution treatment process, extended aging at lower temperatures results in the formation of precipitates in order to lower the energy of the system, leading (with time at temperature) to the peak (T6) and slightly overaged (T76) conditions. For use in an exterior automotive body panel, the effect of the subsequent paint bake heat-treatment cycle (PBC) should also be taken into account, normally comprising 160-185 °C for approximately 30 minutes [31], [37], [38].

Precipitates are considered material hardening elements, creating obstacles to dislocation glide. The T6 temper is the peak aged state, exhibiting the highest mechanical strength with a typical room temperature (RT) ultimate tensile strength (UTS) of approximately 572 MPa [39] for AA7075. The slightly over-aged T76 temper, for comparison, has a UTS of roughly 503 MPa, but provides an enhanced corrosion resistance response which is also a desirable quality for structural components [40]–[42].

The development of the precipitates in a study by Lee *et al*. [32] is shown in Figure 7. Images (a), (c) and (e) in Figure 7 display the development and growth of the finer GP zones following natural aging (NA, aging at room temperature), as well as subsequent artificial aging (AA) at 120 °C for either 30 or 240 min. The diffraction pattern in these pre-aged (PA) conditions (here, PA refers to an aging state preceding the T6 temper) conditions show the GP-zones to be the main phase in the aluminum matrix. With a subsequent paint-bake cycle (PBC) at a higher temperature of 180 °C for a period of 30 minutes (images (b), (d), and (f)) after each PA condition (images (a), (c) and (e) respectively), coarser η' precipitates were observed to become the dominant phase. Figure 7 (b) displays the larger and coarser η' precipitates developing without the need of an intermediate pre-aging treatment. However, by presenting the pre-aging treatments, the η' precipitates were shown to become finer with increasingly higher volume fractions, ultimately leading to more resilient temper conditions, as seen in Figure 8.

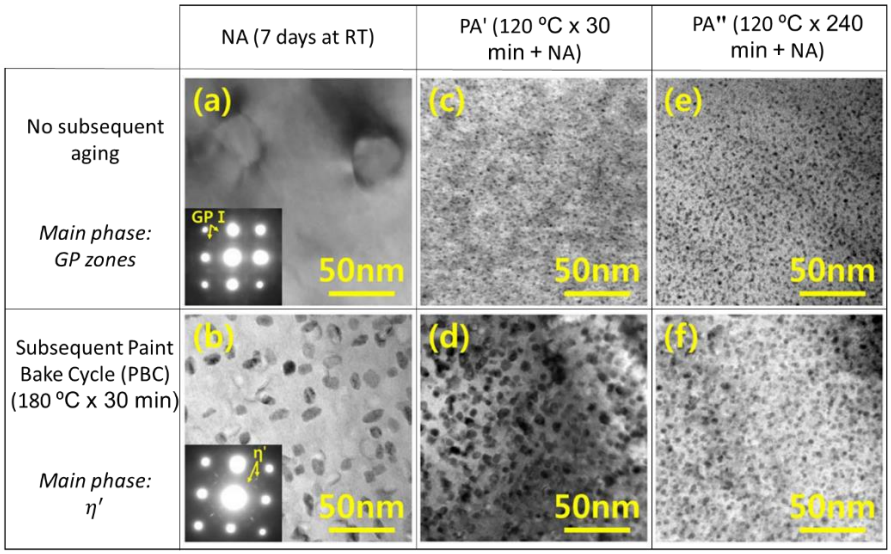

Figure 7. TEM (Bright-field) Micrographs of aging evolution in AA7075 alloy in the <001> zone axis, including selected area diffraction patterns [32].

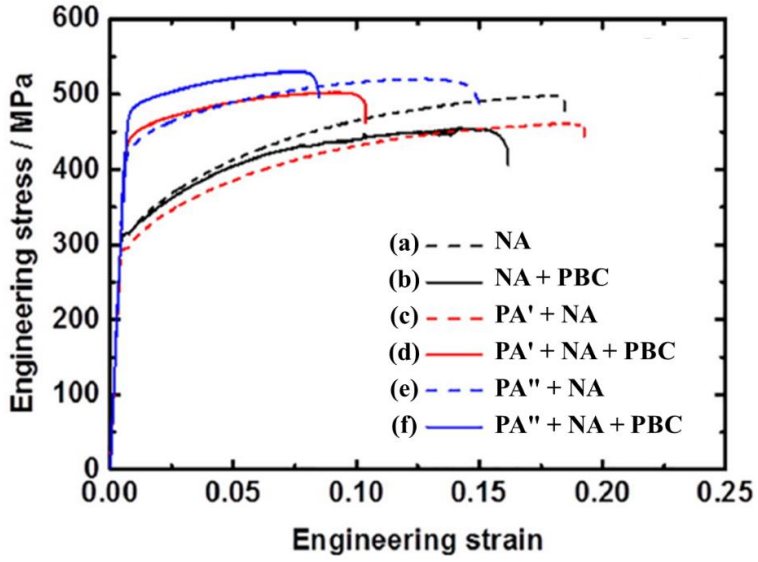

Figure 8. The corresponding Engineering Stress-Strain curves for each of the precipitation states in Figure 7 [32]. ***NA**: 7 Days at Room Temperature. **PA'**: (120 °C x 30 min + NA). **PA"**: (120 °C x 240 min + NA). Paint Bake Cycle (**PBC**): (180 °C x 30 min)*

It is reported that the combination of GP zones and η'precipitates are responsible for the maximum strength of the metastable T6 condition [34]. However, Wang *et al*. [43] showed that for a similar alloy (AA7050), the addition of a pre-straining step, prior to the artificial aging involved in the development of the T6 temper, results in an increase in the number of η'precipitates after the full aging treatment. The higher resultant precipitation hardening, together with the work-hardening (*the entanglement of dislocations*) effect caused by pre-straining is responsible for the enhancement of the mechanical properties beyond what was previously achieved for the T6 temper. Such a modified version of the T6 temper treatment is referred to as the T651 temper [34],[43]. A comparison of the peak age and the pre-strained peak-age, along with the slightly overaged temper (T76) of AA7050 is presented in Figure 9.

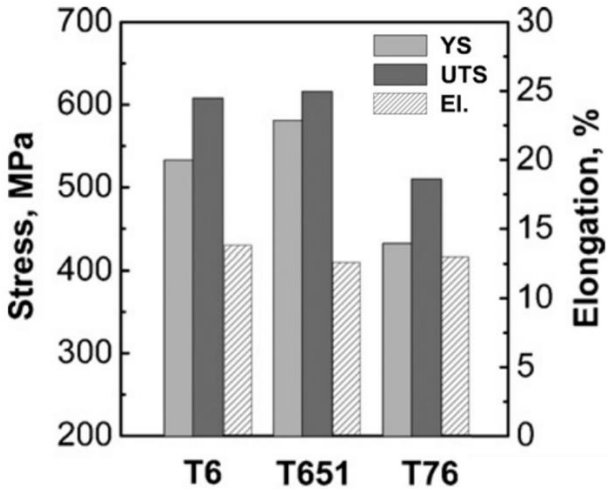

Figure 9. The tensile properties of the peak-aged tempers of AA7050 [43].

The addition of a deformation step in the aging heat treatment can alter the precipitation behaviour in various ways. Deformation-induced dislocations are favourable heterogeneous nucleation sites that result in faster and coarser precipitation. On the other hand, dislocations are also vacancy sinks in which vacancies can be annihilated, which would adversely affect the precipitation strengthening process, as assessed by Deschamps *et al.* [44]. Emani *et al.* [45] also reported that the deformation between two aging steps (*Thermo-Mechanical Double Ageing with a higher temperature assigned to the second ageing step*) leads to an improvement in mechanical properties, attributed to a combination of work hardening and refinement of intermediate phases due to precipitate nucleation on dislocations [45]. Behrens *et al*. [46] , Lee *et al.* [32] and Österreicher *et al.* [31] explored the response of deformation imposed on a few pre-aged conditions. While significant improvements have been seen regarding the alloy's general formability, several mechanical instabilities were also operative in this material condition that adversely affected the repeatability (*i.e. consistency)* of the forming behaviour [47]. The Portevin–Le Chatelier (PLC) phenomenon is shown to be promote such instabilities and will be discussed in the following section.

2.1.2. PLC - A Flow Curve Instability

The dynamic interaction between solute atoms and developing dislocations in the matrix during deformation is referred to as Dynamic Strain Aging (DSA). This phenomenon is a

propagative instability within the material that leads to the jerky motion of dislocations and transient softening [48]. DSA occurs in many polycrystalline dilute alloys, including mild steels with nitrogen and carbon as solute elements and other industrial alloys with only a few percentages of solutes such as magnesium, copper, chromium, and manganese [49],[50]. The macroscopic perspective of DSA was first examined by Portevin and Le Chatelier [51] and is, therefore, known as the PLC effect.

An adverse consequence of the PLC effect is the negative strain-rate sensitivity imposed by the erratic plastic flow and rapid softening, leading to an inconsistent reduction in ductility [48]. This behaviour will, thus, result in undesirable reduced repeatability during forming processes.

Cottrell *et al.* [49] demonstrated the dependency between the diffusion rate of the solutes and PLC effect. Additionally, Halim *et al*. [52] recently reported that the amplitude of the serrations in the flow response is a factor of the strain rate since decreasing the strain rate increases the blockage time at forest dislocations [53],[54].

The PLC behaviour is divided into three general types, as illustrated in Figure 10. Type A is the most irregular pattern with the smallest stress drops. More orderly serrations, characterized by "hopping" patterns with reduced amplitude, are known as Type B PLC bands. With reduced temperature and increased strain rate, a cyclic serration pattern with larger strain drops is observed, which is referred to as a Type C PLC band.

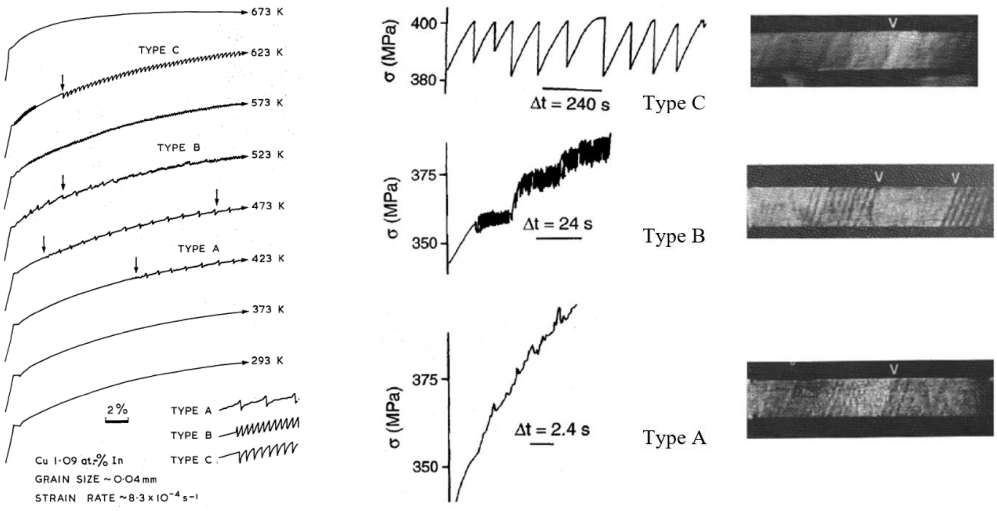

Figure 10. Schematic stress-strain curves showing different PLC serration patterns and resulting shear bands on specimen surfaces [50], [55].

Thus, the amplitude and wave pattern of the PLC bands are functions of the solute characteristics; in particular their diffusion rates, as determined by the temperature and precipitation state, and the subsequent waiting times between the pinning (sticking) and unpinning (slipping) of dislocations [52].

2.1.3. Stability of Pre-Aged (PA) Tempers

Pre-aged tempers are generally susceptible to unintended aging between testing steps, or in the case of industry, manufacturing operations. Österreicher *et al.* [56] have studied the stability of several pre-aged conditions of the AA7075 alloy at room temperature. They have found that following the solution treatment process, an artificial aging time of two hours at temperatures above 90 °C is adequate to stabilize the PA conditions over a three-week period, as illustrated in Figure 11 with dark green diamond markers. Such findings help to identify the time sensitivity of similar tempers for lab or industrial use.

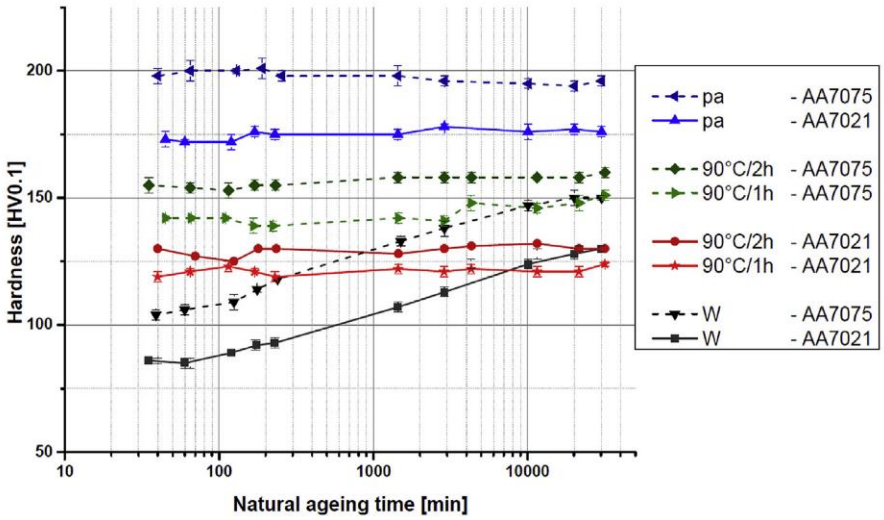

Figure 11. The natural aging response of the pre-aged AA7075 alloy. Error bars represent the standard deviations.[56]
***pa**: peak aged temper. **W**: as quenched temper. **90°C/1h(2h)**: artificially aged at 90 °C for one hour (two hour) immediately after solutionizing process.*

2.2. Constitutive Characterization of 7000-Series Aluminum Alloys

Some high aerospace-grade aluminum alloys (primarily the 7000-series in the context of this thesis) are currently under consideration for application in the automotive industry. Efforts are currently underway, including the current research in this thesis, to identify suitable manufacturing process parameters for these alloys for high volume automotive applications. In the case of AA7075, there are a relatively small number of published studies in the literature that have evaluated the constitutive behaviour of this alloy at room and elevated temperatures in either the pre-aged or peak-aged conditions, as discussed in the following.

Rahmaan *et al.* [57], [58] presented a comprehensive report on the constitutive behaviour of the AA7075-T6 temper for a range of strain rates from 0.001 s^{-1} to 1000 s^{-1} at room temperature. Moreover, Wang *et al*. [28], Sotirov *et al*. [29], Polak *et al*. [30] and Österreicher *et al*. [31] evaluated the constitutive characteristics and formability of the AA7075-T6 at elevated temperatures. Such studies demonstrated the high forming potential of this alloy given the thermal softening effect with reduced flow stresses and extended elongations. However, at the elevated testing temperatures, extended aging beyond the peak aged condition (T6) led to a loss in strength and ductility, since the material aged beyond the peak age condition [28], [30], [31], [37].

Lee *et al.* [32] delved deeply into the effect of pre-aging of AA7075, which includes a constitutive response study at a constant strain rate. As displayed in Figure 12, they revealed that the pre-aged conditions have a high work-hardening rate (WHR) and work hardening exponent (n-value, more in Section 2.2.2), which is indicative of the higher formability potential. Figure 12 [Right] highlights the reduction of total elongation and the n-value with extended aging. Such results provide motivation for the constitutive characterization of pre-aged AA7075 in the current study.

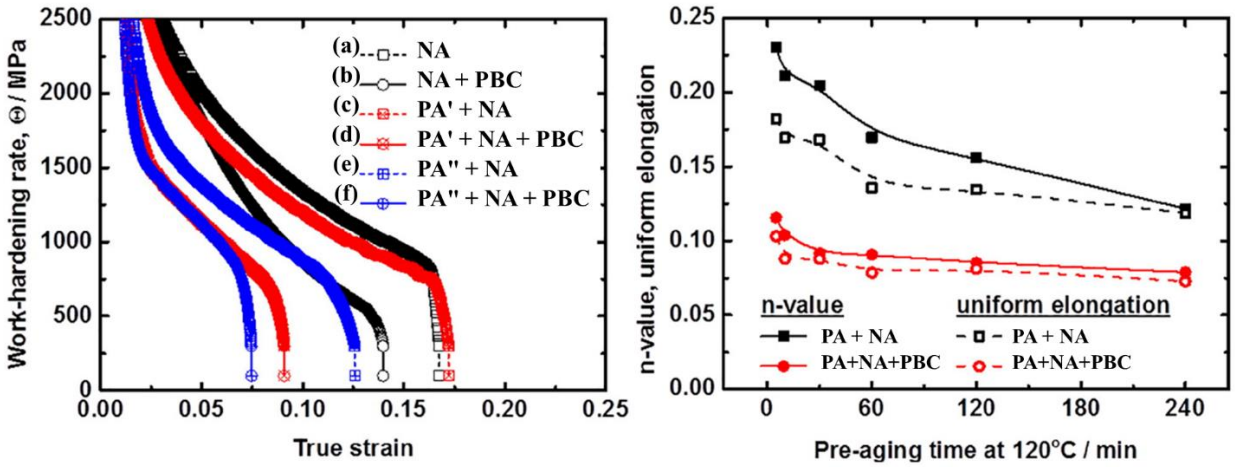

Figure 12. [Left] Work-hardening rate vs. true strain response, corresponding to the pre-aged conditions introduced in Figure 8. [Right] n-value and uniform elongation vs. pre-aging period (min) at 120 °C for two pre-aged conditions.
***NA**: 7 Days at Room Temperature. **PA'**: (120 °C x 30 min + NA). **PA"**: (120 °C x 240 min + NA). Paint Bake Cycle (**PBC**): (180 °C x 30 min)* [32]

As a side note, it should be mentioned that in addition to the instantaneous WHR and the averaged n-values, evaluated in the work by Lee *et al.* [32], given the availability of proper data acquisition technology, the instantaneous n-values are also regarded as valuable indicators of formability response in the literature [59], [60]. Ratke and Welch [61] defined this metric, independent of hardening laws (briefly described in Section 2.2.2) for a specific single stress-strain curve, as:

$$n_i(\varepsilon) = \frac{dln(\sigma)}{dln(\varepsilon)} \qquad \text{Eq [1]}$$

in which $n_i(\varepsilon)$ is the instantaneous work (strain) hardening exponent, and σ and ε are the true stress and strains, respectively. This equation can further be simplified as:

$$n_i(\varepsilon) = \frac{\left(\frac{d\sigma}{\sigma}\right)}{\left(\frac{d\varepsilon}{\varepsilon}\right)} = \frac{\varepsilon d\sigma}{\sigma d\varepsilon} \qquad \text{Eq [2]}$$

This simplified equation can be utilized to assess the full history of the formability behaviour over the duration of a test as a function of the work hardening exponent, given the experimental flow curve.

Recently, a relevant study by Österreicher *et al*. [31] on the formability of AA7075, motivated by Lee *et al*. [32], has assessed the effectiveness of forming a pre-aged temper at elevated temperatures. The work hardening exponent calculated by Österreicher *et al*. [31] at different temperatures, as a measure of formability, are shown in Figure 13.

Considering the fact that faster aging kinetics are at play in the warm forming process, a lower amount of subsequent aging during the PBC is required to achieve a final peak strength. In addition, the evident superiority of the formability responses corresponding to the respective pre-aged condition versus the peak-aged T6 temper, supports use of this process route, at temperatures ranging from 25 °C to approximately 175 °C [31], according to Figure 13.

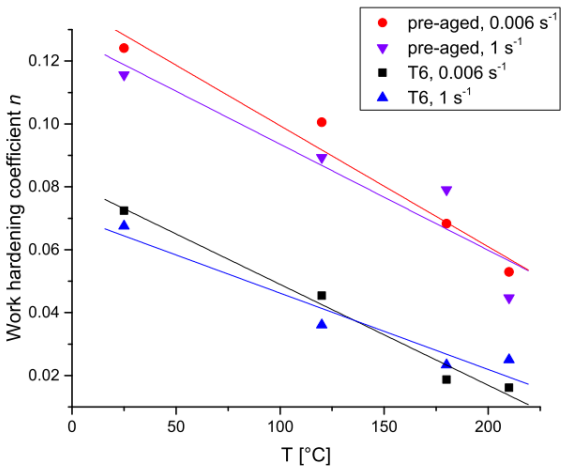

Figure 13. The n-values of the pre-aged temper versus the T6 temper at various temperatures [31]*.*
***pre-aged**: 120 °C for 2 hours, following the solution treatment process.*

With further aging at paint-bake temperatures, the pre-aged alloy reached strength levels almost 95% of the peak (T6) strength, mitigating the larger reduction of strength as observed using the T6 temper condition [31].

2.2.1. Modelling of Precipitation Strengthening

Numerous studies have been conducted on the precipitation hardening of the 6000 and 7000-series aluminum alloys subjected to various heat treatment cycles. Deschamps *et al.* [36] introduced a yield strength prediction model given the shearable, non-shearable obstacle strength contributions.

A yield strength model was calibrated by Esmaeili *et al*. [62] for 6000-series aluminum alloys, in which the contributions of the solid solution strengthening (σ_{ss}), due to the solute concentration, and the precipitation hardening (σ_{ppt}), are added to the intrinsic strength of the aluminum (σ_i) [63]–[65]. This additive, which includes the summation of a handful of strong and a large aggregate of small obstacles attributable to the precipitate and solute atoms [64], [65], is given by:

$$\sigma_y = \sigma_{ppt} + \sigma_{ss} + \sigma_i \qquad \text{Eq [3]}$$

The average obstacle strength was found to be linearly correlated with the growing radius of the precipitates until the peak aged condition, followed by a power law correlation, given shearable obstacles.

Cheng *et al.* [66] presented a flow stress model that integrates the dislocation-induced strengthening (work hardening or plastic work), σ_{dis}^n, into the existing precipitation hardening model, as follows:

$$\sigma_{flow} = \sigma_{\mathrm{i}} + \sigma_{ss} + \left(\sigma_{\mathrm{ppt}}^n + \sigma_{dis}^n\right)^{\frac{1}{n}} \qquad \text{Eq [4]}$$

in which the exponent *n* describes the interplay between the precipitation and dislocation stress contributions.

Omer *et al.* [67] combined the existing efforts into a union of precipitation hardening models (Eq [5]) to predict the flow stress of the die-quenched specimen following a successive aging treatment.

$$\sigma = \sigma_{\mathrm{i}} + \sigma_{0ss}(1 - f_r)^{\frac{2}{3}} + \left(\left(C_1 f_r^{\frac{1}{2}} \right)^{1.5+0.5\tanh\left(\frac{\frac{R}{R_C}-1}{\chi}\right)} + \left(\sigma_s \left(1 - \frac{\theta}{\theta_0} \right) \right)^{1.5+0.5\tanh\left(\frac{\frac{R}{R_C}-1}{\chi}\right)} \right)^{\frac{1}{1.5+0.5\tanh\left(\frac{\frac{R}{R_C}-1}{\chi}\right)}} \quad \text{Eq [5]}$$

in which σ_{0ss} represents the SSS yield strength, and f_r is the relative volume fraction of the precipitates [68]; C_1 is a function of the peak aged yield strength [62]; R is the average precipitate radius as a result of the heat treatment process, $\mathrm{R_C}$ is the average precipitate radius, corresponding to the threshold between the shearable and non-shearable states, and χ is the abruptness measure of the shearable to non-shearable transition [68]. Lastly, σ_s is a factor taking the absence of precipitates into account, θ_0 correlates to the initial rate of hardening of the material, and θ is the instantaneous work-hardening rate [68].

This amalgamation resulted in an accurate prediction model of the hardening behaviour of pre-aged and peak-aged initial conditions [67].

2.2.2. Modelling of Plasticity Response

To model the plasticity of a material, the determination of a yield surface (which distinguishes the elastic and plastic behaviour of the material) is one of the first requirements. The first yield criterion was introduced by Tresca in 1984, where a maximum shear threshold is defined as the initiation point of plastic flow. The von Mises model was another yield criterion, which assumed

that the material yielding occurs when maximum shear stress on the octahedral plane reaches a critical value. The Tresca and von Mises yield functions, however, presume isotropic behaviour. To consider the anisotropy of materials like aluminum alloys, several anisotropic yield functions have been thus far proposed. The Barlat YLD2000 [69] equation is one of most widely-used anisotropic yield models. Rahmaan *et al.* [58] have calibrated the YLD2000 yield function of the AA7075-T6 sheet based on tensile testing at every 15° increment from the principal rolling direction of the material, as well as shear and through-thickness compression testing [57].

With further deformation, yield surfaces are subjected to change. Isotropic hardening is the simplest hardening model which assumes the uniform (proportional) expansion of yield surfaces within a stress domain with accumulation of plastic work. To mathematically determine such hardening response, knowledge about the relation (constitutive equation) between flow stress and strain is required, which is acquired by conducting uniaxial-tension tests and then modelling the stress-strain response using a suitable hardening law. The most common hardening law is the power-law function, Eq [6], with the hardening exponent, *n* (or *n-value*), being a commonly adopted indicator of the formability response of a given material.

$$\sigma_{flow} = K \cdot \varepsilon^{n} \qquad \text{Eq [6]}$$

in which K is referred to as the strength coefficient, and n is the hardening, or power law, exponent.

Furthermore, the Hockett-Sherby [70] hardening model , Eq [7], has shown to be an excellent representative of the plastic hardening behaviour of AA7075-T6, as determined by Rahmaan *et al.* [58].

$$\sigma_{flow} = \sigma_{ss} - (\sigma_{ss} - \sigma_{Y}) \cdot \exp(-N \cdot \varepsilon^{P}) \qquad \text{Eq [7]}$$

in which, σ_{ss} and σ_{Y} are the steady state and yield stresses, and N and P are material constants.

Lastly, a concise assessment of a number of strain-rate and temperature dependant models, namely the Extended Nadai, the Bergström, and the Nes models, was undertaken by Kurukuri *et al*. [71] for AA3003 sheet material. Additionally, Omer *et al*. [70] performed a comprehensive study on the constitutive response of AA7075 and a developmental 7000-series alloy during hot

forming using the modified Voce model, Eq [8], with a good agreement with the experimental results.

$$\sigma = A + \left(B + C\sqrt{\varepsilon^p}\right) \cdot (1 - e^{-D\varepsilon^p}) \qquad \text{Eq [8]}$$

in which, the parameters A, B, C, and D correspond to polynomial equations as a function of temperature and strain rate.

The models were verified against various strain rate and temperature stress-strain curves, as shown in Figure 14.

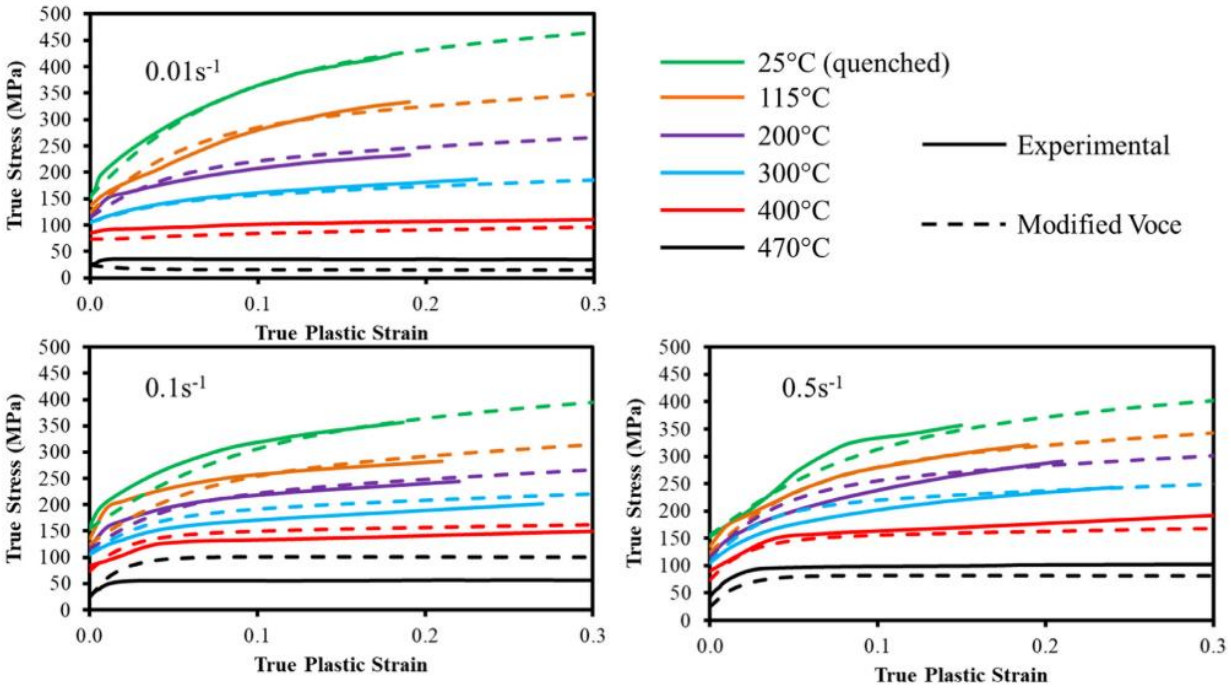

Figure 14. Constitutive modelling using modified Voce fitting model [72].

2.2.3. Characterization Methods for Large Tensile Strains

One of the main concerns with tensile tests performed at elevated temperatures is the thermal uniformity along the gauge length of the tested specimens, as well as the onset of diffuse necking, both of which tend to promote a heterogeneous strain field. Thus, a localized stress-strain extraction method is required since the existence of a uniform strain within the gauge section rarely persists beyond a few per cent strain. One approach to extracting the stress-strain using a local technique was proposed by Omer *et al.* [73] and is referred to as the Area Reduction Method

(ARM). This method uses Digital Image Correlation (DIC) technology to extract the instantaneous local lengthwise and width-wise dimensions of the specimen in the pull-direction of the tensile test. Furthermore, using the thickness strains obtained from the volume conservation assumption, the instantaneous cross-sectional area is obtained for each frame (image) of the captured data. This area is then utilized in combination with the load data from load cells to determine the true stress and logarithmic (area) strain at each frame.

The limits of the validity of ARM, mainly imposed by the requirement to reduce strain-rate variation and the intrinsic deviation of the stress state from uniaxial to plane strain, was considered by Omer *et al.* [72]. The proposed solution was to discard values beyond which the strain rates or strain paths had deviated from the intended and nominal input parameter.

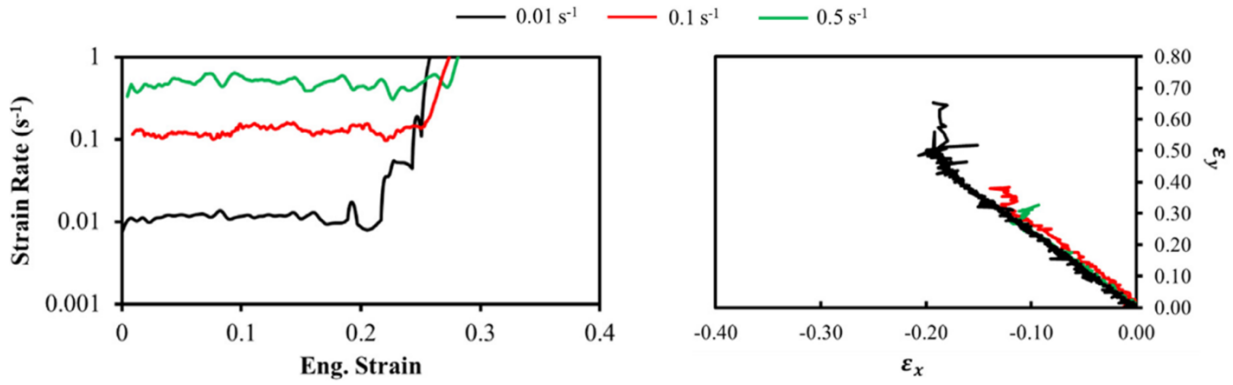

Figure 15. Limits of validity of the area reduction method (ARM). The deviations of [Right] Strain rates, and [left] strain paths, from the nominal input parameters [72].

Alternatively, the phenomenological ARM corrective measures proposed by Choung *et al.* [74], following the work of Scheider *et al.* [75], have shown to limit the discrepancies caused by the increased strain rate and the altered loading condition. These efforts can help utilize the full extent of the extracted data using the ARM, but use isotropic and power-law flow response assumptions, which may not be applicable to all materials.

Choung *et al.'s* [74] correction factor, to be multiplied with the ARM stresses, is presented in Eq [9].

$$\zeta(\varepsilon_p) = \begin{cases} 1, & \varepsilon_p \leq 1.4n \\ \alpha\varepsilon_p^2 + \beta\varepsilon_p + \gamma, & \varepsilon_p > 1.4n \end{cases} \qquad \text{Eq [9]}$$

in which, n is the power-law work hardening exponent, $\alpha = -0.0704n - 0.0275$, $\beta = 0.4550n - 0.2926$, and $\gamma = 0.1592n + 1.024$. These relations are valid for materials with an n-value of 0.10 – 0.30.

2.3. Formability of 7000-series Aluminum Alloys

The Forming Limit Diagram (FLD) is a tool to determine the intrinsic extent of deformation of a specific material (or temper in this study) over a range of loading conditions (strain states), from drawing to stretching [76]. The FLD is used to mark the limit strains during metal forming in order to avoid non-uniform thinning, *i.e.* necking, local thinning of the material leading to fracture, or in some cases, excessive surface roughening.

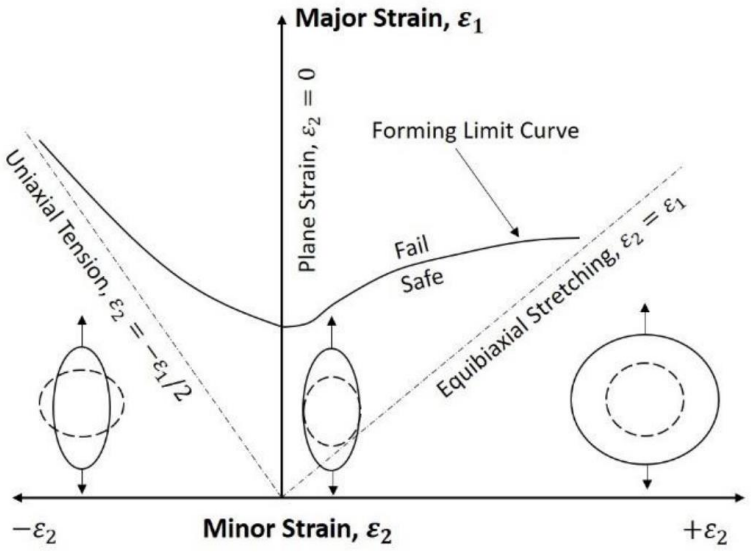

Figure 16. A representation of a forming limit diagram (FLD) corresponding to different loading conditions [77].

A forming limit curve (FLC), consequently, is the curve that demarks the boundary between uniform straining and localized necking (solid curve in Figure 16). The work-hardening and strain-rate ($\dot{\varepsilon}$) sensitivity exponents (*n* and *m*, respectively) are known as representative parameters influencing the formability response of materials. The power law equation modified to accommodate the strain rate effects is defined as:

$$\sigma_{flow} = K \cdot \varepsilon^n \cdot \dot{\varepsilon}^m \qquad \text{Eq [10]}$$

Considering a power-law model, Hill [78] showed that the left-hand side of FLDs is controlled by the material work-hardening exponent (see Figure 17). The strain rate sensitivity can vary forming limits by influencing the speed at which local necks can grow. A positive strain rate sensitivity (i.e. positive *m*) results in the extension of deformation after the ultimate-tensile-strength (UTS) point and, therefore, improves formability. Figure 17 shows schematically the effects of the *n* and *m* parameters on the FLC. As can be seen, the higher the *n* and *m* values are, the higher the material formability is.

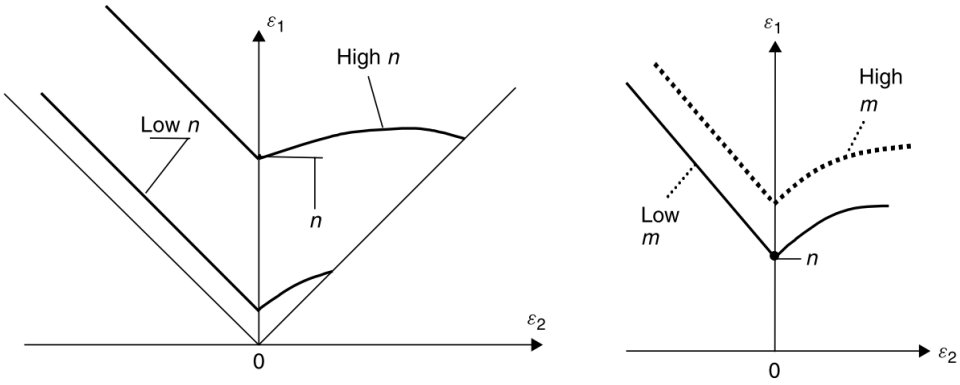

Figure 17. The effect of work-hardening index (n) [left] and the strain rate sensitivity exponent (m) [right] on the forming limit curve. [79]

Moreover, another major parameter commonly affecting the formability behaviour is temperature, as discussed in Section 2.2. Bagheriasl *et al*. [80] evaluated the warm forming response of the AA3003 brazed sheet with an AA4045 clad layer. They found a 229% improvement in formability at forming temperatures of 250 °C compared to room temperature forming. Boba *et al.* [81] also found significant improvements (of nearly tenfold) for the AZ31B alloy, with more complex forming mechanisms due to reduced number of slip planes.

Further, Li *et al*. [82] have compared the warm-forming response of two automotive aluminum sleet alloys, AA6011-T4 and AA5754 (see Figure 18), and have highlighted the reduced formability gains at higher temperatures for the 6000-series alloy. DiCecco *et al.* [83] have also confirmed this behaviour on the AA6013-T6 sheet alloy, shown in Figure 18. This response can

be attributed to the age hardening characteristics of the 6000-series alloys, which are absent in the 3000-, 4000-, and 5000-series aluminum alloys [84].

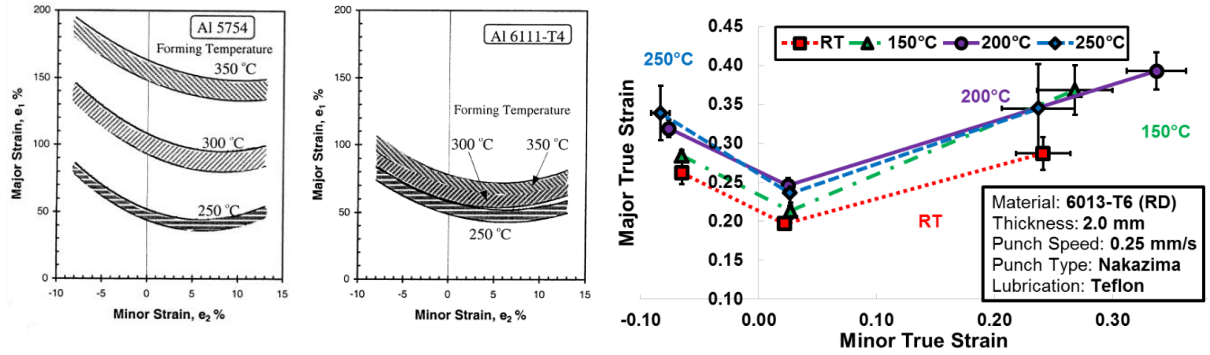

Figure 18. Warm forming response of 5000 and 6000-series aluminum alloys [82], [83].

While the 7000-series aluminum alloys show a lower formability at RT, an increased potential for warm forming has been observed (Figure 19) in the studies of Pishyar *et al*. [85] and Sotirov *et al*. [29]. Such findings demonstrate the higher general thermal softening effects on the 7000-series alloys, compared to that of the 6000-series aluminum alloys.

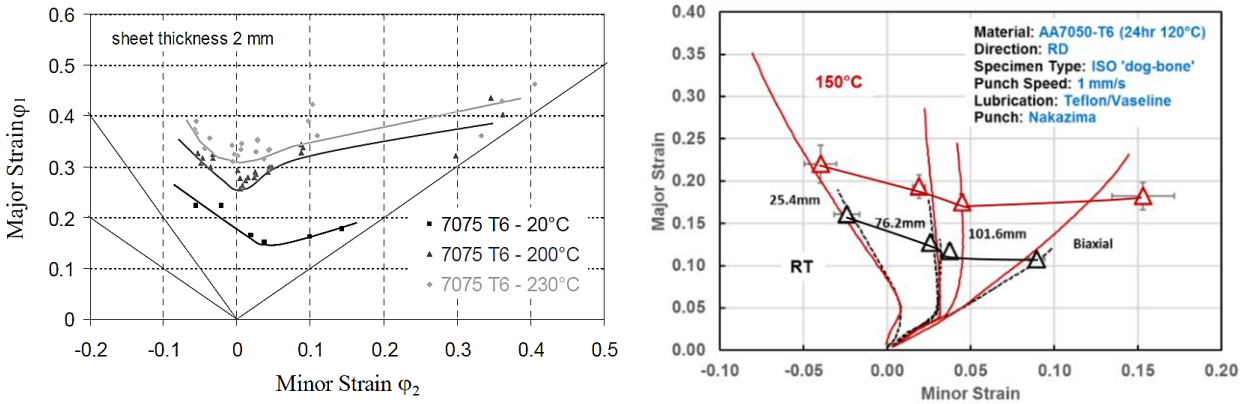

Figure 19. Warm formability of high strength aluminum alloys, [Left] AA7075-T6 [29] *, [Right] AA7050-T6* [85]*, as a function of forming temperature.*

Other factors influencing the general formability response of metals include, but are not limited to imperfections within the matrix of the alloy and the fracture behaviour of the material.

2.3.1. Evaluation Methods of Formability

The early methods of the visual evaluation of formability consisted of etching (circular or square shaped) grids on the test specimen and then estimate their local strains based on the physical

measurement of their initial and final sizes. Such methods have been standardized using various test apparatus including the Nakazima [86] and Marciniak [87] forming tool sets, and are used to capture local instabilities as opposed to a global instability in the case of deep drawing.

More advanced methods incorporate the use of non-intrusive data acquisitions methods, such as image capturing and analysis, for recording the full history of deformation during the forming process [88][89]. The Digital Image Correlation (DIC) technique is one of these methods that has led to the development of various necking detection methods, with far greater accuracy and precision. A representation of the strain distribution obtained using the DIC method is presented in Figure 20 [Left].

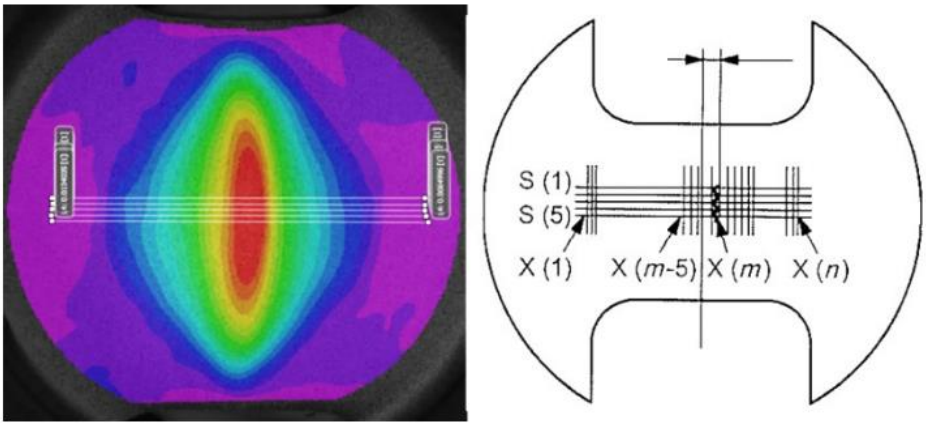

Figure 20. The major strain distribution using DIC [Left] [90]*, and strain extraction method as outlined in ISO12004-2:2008 [Right]* [91].

Conventionally, two main schools of thought exists in the field of necking detection methods. The ISO12004-2:2008 standard utilizes a *spatial analysis* in which the strain *vs.* specimen length is fit using a parabolic equation, and the local peak strain point (within the parabola) defines the maximum major strain [91]. The second method utilizes a *temporal analysis*, in which the rapid growth of the strain rate or thinning rate of the material (amongst other temporal detection methods) defines the initiation of localized necking [92], [93]. However, a comparison study by Min *et al.* [94] concluded that methods combining both temporal and spatial analysis provide the most robust outcomes, since the necking is a material instability resulting from both of these factors [94].

In recent years, DiCecco *et al.* [83] and Min *et al.* [95],[96] explored a surface-geometry characterization method to detect the initiation of localized necking given the instantaneous change in the specimen surface curvature during Marciniak and Nakazima tests. Wang *et al*. [97] also developed a spatio-temporal method in which a sudden increase in the height of the specimen surface topology, indicated by the through-thickness strains at the location of necking versus a point in the neighbouring uniform deformation region during the forming process, defines the localized necking initiation point.

Most recently, Noder *et al.* [98] explored a cost and time efficient stress-based forming limit prediction method utilizing the constitutive behaviour of the material under analysis, which has led to an accurate and universal analytical prediction model. This prediction model was initially proposed by Stoughton *et al.* [99], [100] as a method of circumventing the inaccuracies caused by complex non-linear strain paths, independent of the load path.

Furthermore, with the emergence of artificial intelligence, new algorithms have been trained to predict the forming limits of an unknown and untrained forming condition. Examples of which include the work of Elangovan *et al*. [101] and Kotkunde [102].

2.4. Summary of Literature Review and Objectives of Current Study

The formability of the high strength aluminum alloy AA7075 has been the topic of previous research, due to its excellent strength-to-weight ratio, for use in complex-shaped automotive components. A review of the existing literature has revealed that the formability of this material can significantly be improved at elevated temperatures; however, if a peak aged specimen is warm formed, over-aging can occur, resulting in deterioration of the final properties. Of particular interest, recent work has demonstrated that forming of this material in so-called pre-aged conditions can result in improved formability under both room temperature and warm forming conditions [31], [32]. It has also been determined that subsequent heat treatment steps, such as introduction of an automotive paint bake cycle can also result in good final properties within the as-formed part.

To date, however, there has been only limited study of the warm constitutive behaviour of pre-aged AA7075 during the actual warm forming process. In addition, there has been very little

systematic study of the formability of this alloy and temper under warm forming conditions. Both of these topics require attention in order to support numerical simulation of warm forming of pre-aged AA7075; the current thesis aims to address these gaps in the published literature. Additionally, the post-PBC properties of a selection of optimal warm forming conditions are evaluated to address the objective of achieving a high final strength or temper.

3. Material & Experimental Procedure

This chapter presents the material and the experimental procedures used in this research. Section 3.1 presents the alloy and composition, while Section 3.2 describes the overall test matrices and the ranges of thermo-mechanical processing routes considered. The various mechanical testing apparatus are documented in Sections 3.3 to 3.5, which include the individual test settings. Some additional information on the test settings and equipment validations are also provided in Appendices A and B, as also referenced in the appropriate sections in text.

3.1. Material Properties

The material considered in the current study was AA7075 aluminum alloy sheet, a heat-treatable and work-hardenable alloy with the chemical composition listed in Table 1. The as-received sheet material, with a thickness of 2 mm, was manufactured by Kaiser Aluminum and received in the T6 temper condition.

Table 1. AA7075 Chemical composition as measured

Element	**Mn**	**Si**	**Cr**	**Mg**	**Ti**	**Cu**	**Zn**	**Fe**	**Zr**	**Al**
Weight %	0.04	0.08	0.19	2.27	0.03	1.38	5.63	0.15	0.01	90.22

The typical mechanical properties of the alloy are presented in Table 2. The O temper (annealed condition) is also listed in addition to the T6 (peak aged) condition, for reference.

Table 2. The typical mechanical characteristics of AA7075 [103].

Temper	**Tensile Strength (MPa)**	**Yield Strength (MPa)**	**Elongation (%)**
O	227.5	103.4	18
T6	572.3	503.3	12

Furthermore, due to the rolling process employed during the manufacturing process of this sheet material, anisotropy in the crystal structure (rolling texture) causes differences in the mechanical properties when the material is tested in different (rolling *vs*. transverse) directions. This anisotropy is commonly defined by the Lankford coefficient (r-value) and is obtained from Eq [11],

$$r = \frac{\varepsilon_w}{\varepsilon_t} \qquad \text{Eq [11]}$$

in which ε_w and ε_t are the true width and thickness strains during uniaxial tensile testing. The r-value of AA7075 ranges from 0.78 to 1.34 [57]. Lower r-value materials are commonly expected to have lower resistance to thinning in a forming process.

The anisotropy of the AA7075 alloy was shown to remain relatively unchanged for various pre-aged conditions (except the O- temper) as determined by Leacock *et al.* [104]. This behaviour is graphically presented in Figure 21.

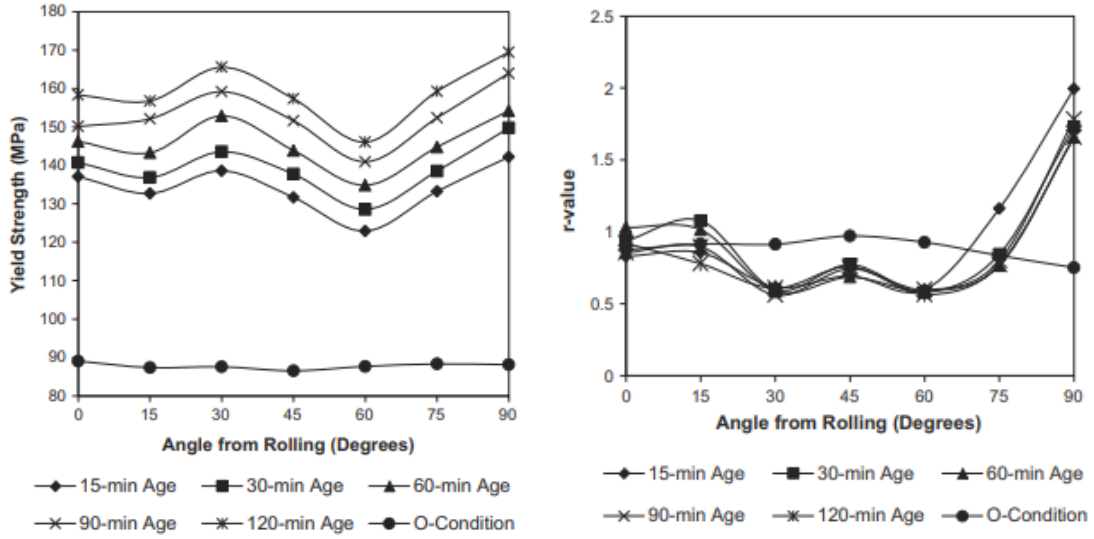

Figure 21. [Left] the yield strength of various tempers of AA7075 versus the test orientation. [Right] The uniaxial anisotropy (r-value) of the different tempers as a function of test orientation. The heat treatment temperature was set to 120 °C [104].

3.2. Thermo-Mechanical Processing Routes

Several pre-aging heat treatment schedules were considered at temperatures of 80 °C, 100 °C and 120 °C, for heat treatment periods of either 1, 2, or 4 hours. An additional as-quenched condition with a subsequent natural aging period of two days, as well as the as-received T6 temper, were also evaluated to determine the mechanical response of this alloy between the extremes of the nearly as-quenched condition and the peak aged condition.

The experimental program was divided into four "stages" comprising:

- Stage 1 – Pre-aging followed by room temperature tensile and formability testing;
- Stage 2 – Pre-aging of selected processing routes followed by warm constitutive characterization at various temperatures, heating rates and strain rates;
- Stage 3 – Pre-aging of selected processing routes, followed by warm formability characterization at various temperatures, heating rates and forming speeds;
- Stage 4 – Paint bake processing of selected as-formed specimens, followed by hardness characterization.

The initial scope in Stage 1 was quite broad, however, a down-selection of material conditions was undertaken to reduce the considered tempers and test conditions for each subsequent stage, with the general objectives of improving formability, forming stability (absence of PLC effect), and achieving a peak final temper (strength). The testing performed in each stage is outlined in the following text.

The heat treatment process for all tensile dog-bone specimens (Figures 30 and 36) used in the constitutive characterization experiments was performed in a fluidized (sand) furnace. However, due to their larger overall dimensions, the plane strain specimens (Figure 32), used to evaluate the warm formability response, were heat-treated in a separate convection furnace. Studies of the thermal response for the two furnaces are presented in Appendix A, Sections A.1 and A.2 . After heat treatment, the specimens were stored in dry-ice within a low temperature freezer (set to -40 °C) to minimize the precipitation kinetics of the specimens between the pre-aging and testing processes.

3.2.1. Stage 1 – Preliminary Room Temperature Temper Evaluation

The process schedule adopted for the first stage is shown in Figure 22. As illustrated, the as-received T6 temper specimens were first solution treated at approximately 472 °C for 30 minutes, followed by water-quenching – which placed the specimen at a Supersaturated Solid Solution State (SSSS). The specimens were then allowed to naturally age for two days (2 day N.A.). This period

represents a nominal material handling time in industry and promotes the growth of fine and closely spaced GP zones, as observed by Lee *et al*. [32]. Some specimens were placed in dry-ice for testing at this specific aging state. The remaining specimens underwent the artificial aging processes at the aforementioned pre-aging temperatures and duration. These specimens were then placed in dry-ice until tested at room temperature (RT).

A summary of all conditions evaluated in this stage, is given in Figure 23, and involved a pool of 9 pre-aged conditions, as well as the T6 and 2 day N.A. tempers for reference. This range of conditions served to provide a general understanding of constitutive behaviour and formability limits as a function of pre-aged condition. The mechanical testing for this first stage was performed at room temperature and comprised tensile testing, at a strain rate of 0.01 s^{-1}, and Nakazima dome testing, with a punch speed of 0.5 mm/s. Each test condition included four repeats to evaluate the repeatability of the results. The testing methodologies for the room temperature tensile and formability experiments are given in Sections 3.3.1and 3.3.2, respectively.

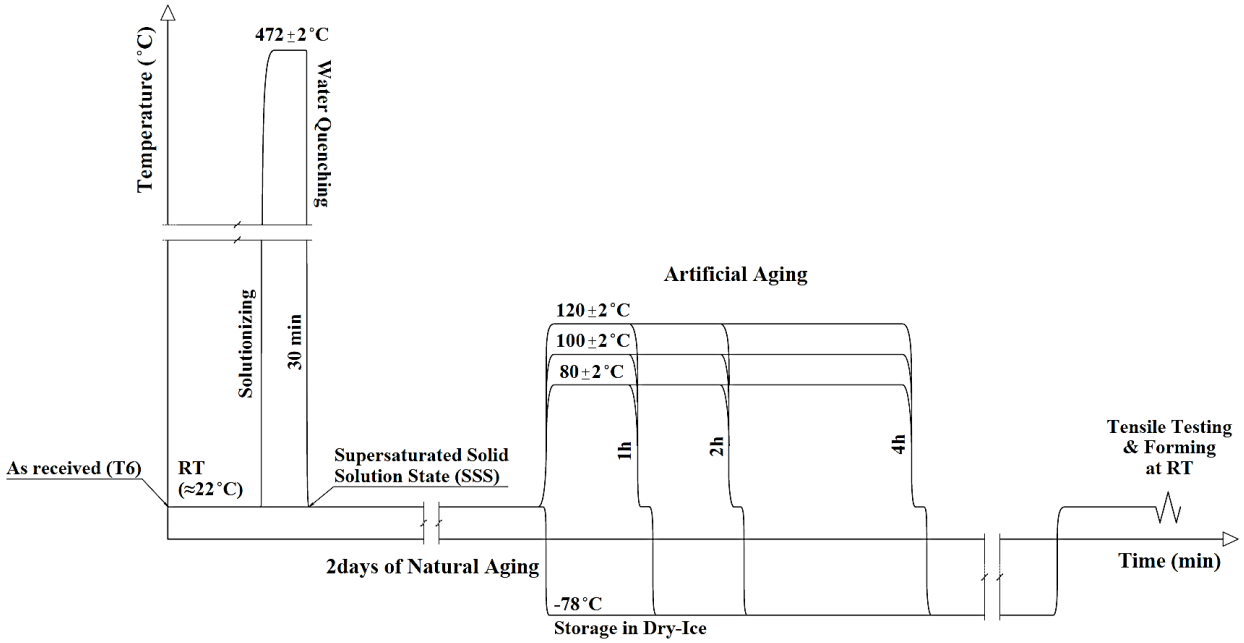

Figure 22. Preliminary (Stage 1) AA7075 pre-aging heat treatment and room temperature testing process parameters.

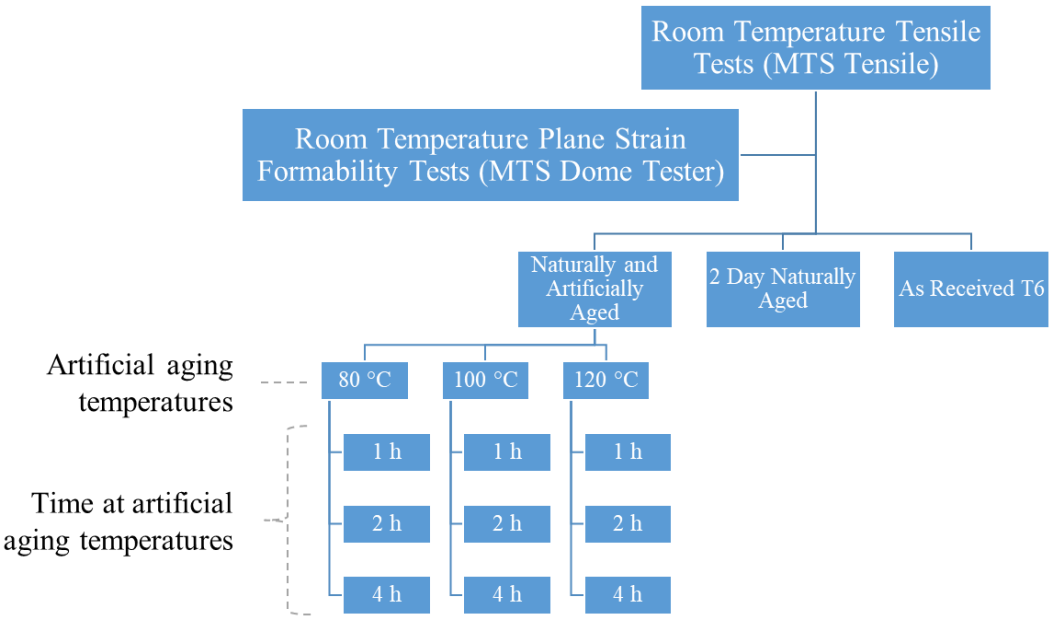

Figure 23. Stage 1 – preliminary *room temperature temper evaluation test matrix.*

The terminology used to refer to each one of these PA temper conditions is comprised of the aging temperature followed by the aging time at this temperature (*i.e.* 120C1h refers to the temper aged at 120 °C for the duration of 1 hour).

3.2.2. Stage 2 – Warm Constitutive Characterization of Selected Tempers

Stage 2 comprised the warm constitutive characterization of selected tempers. In this stage, the pre-aged tempers were limited to a 4 hour pre-age duration at either 80 or 100 °C (the rationale behind these choices will be presented in Chapter 4). Here, a more comprehensive constitutive characterization study was undertaken (Figure 24) at multiple forming temperatures (150, 175 and 200 °C), heating rates (20 ~ 0.83 °C/s) and deformation rates (0.01, 0.1 and 1.0 s^{-1}, corresponding to typical warm forming conditions). The tensile experiments were performed on a Gleeble 3500 thermo-mechanical simulator and the Gleeble test matrix is presented in Figure 25. The details of the methodology for these experiments are given in Section 3.4.1. Similar to the Stage 1 tests at room temperature, each test condition was repeated a minimum of four times to evaluate the repeatability of results.

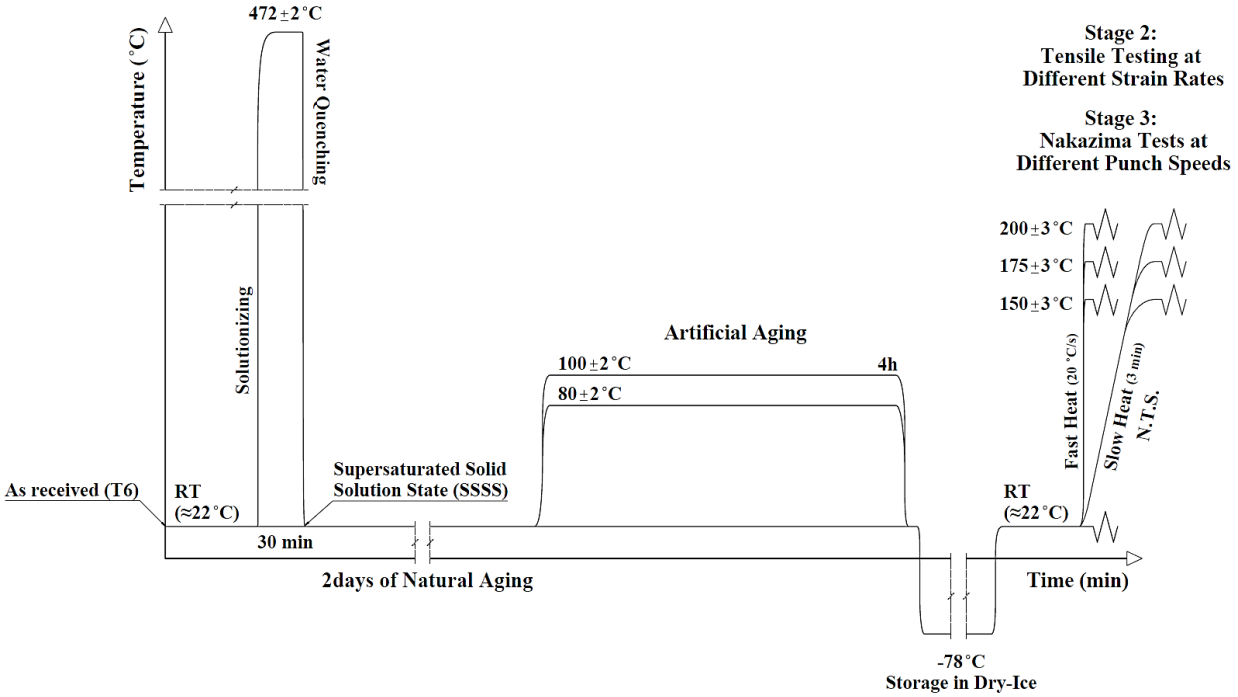

Figure 24. Stage 2/3 (Gleeble/Warm Nakazima) – AA7075 pre-aging heat treatment and constitutive/formability characterization process parameters.

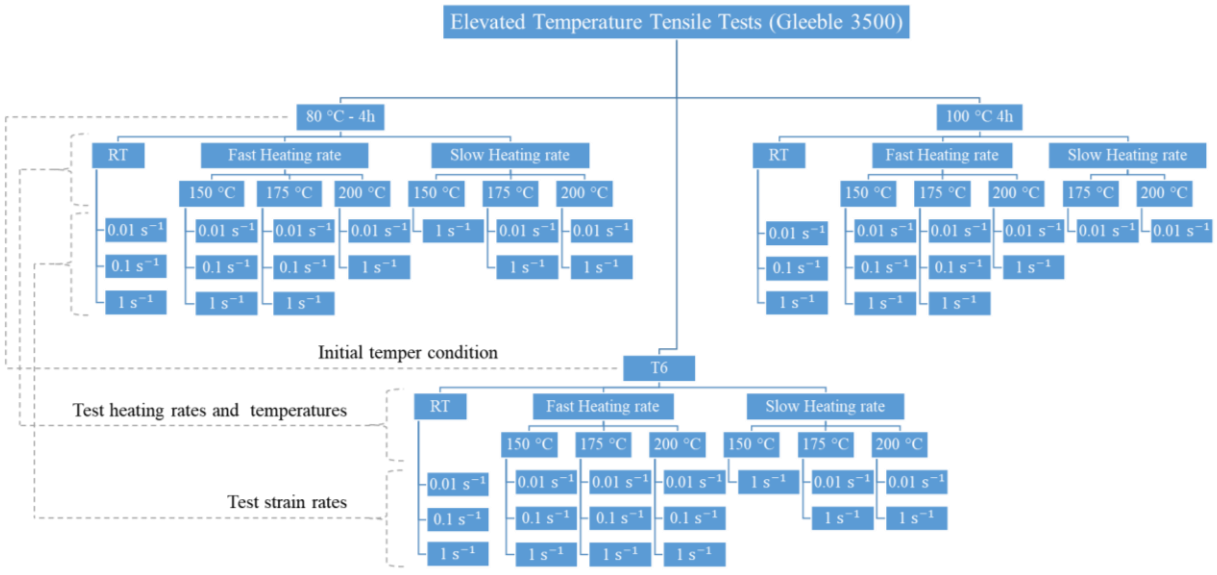

Figure 25. Stage 2 – Gleeble test matrix for the warm constitutive characterization experiments.

In the Stage 2 experiments, two heating rates were examined to evaluate the effect of aging during heating corresponding to a slower conventional heating method and a newly available fast contact heating method, utilized in the Nakazima warm forming experiments (Stage 3, Section 3.4.2). The slow heating parameters were obtained from a pre-existing test apparatus, which used

the heated tool and die-set to gradually heat up the specimens in an average time of roughly 3 minutes. The new fast heating method, was capable of achieving heating times as low as 8 seconds to reach the maximum testing temperature of 200 °C. Therefore, a conservative heating rate of 20 °C/s was adopted for the fast heating process, which was used for all warm tensile tests.

The Gleeble apparatus was programed to mimic the two heating rates under consideration. The fast heating experiments included a dwell period of approximately 10 seconds at the warm forming temperatures to simulate the sample transfer and clamping period in the warm forming process (discussed in Section 3.4.2). Moreover, this added time also served as a stabilization period allowing the Gleeble test specimens to achieve a more uniform temperature distribution across the gauge region. The dwell period was not considered necessary for the slow heating cycle. The detailed thermal cycle for the Gleeble tests are illustrated in Figure 26.

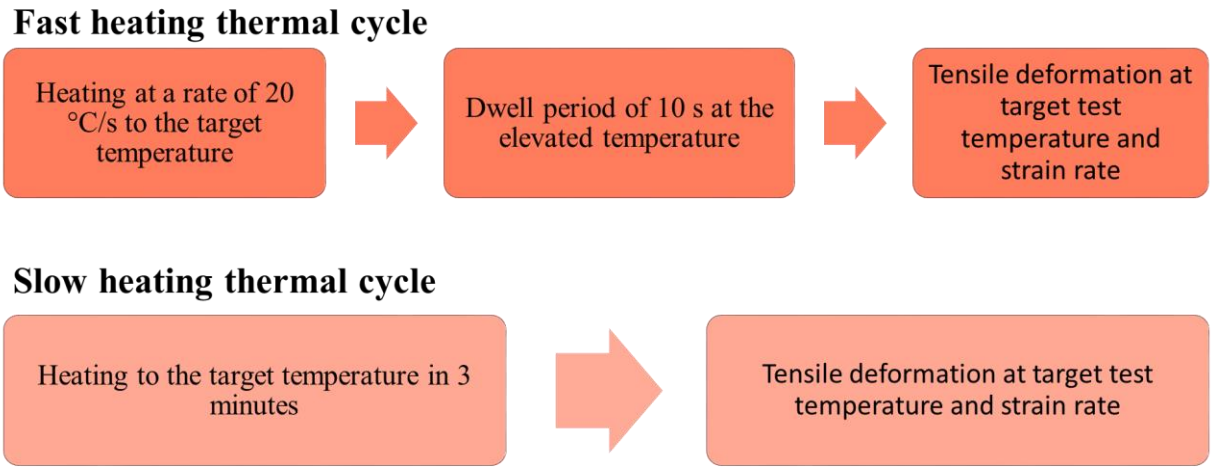

Figure 26.Thermal cycles in the Gleeble tests.

The abbreviations for these test conditions (or process routes) comprise the corresponding test temperature, followed by the temper, the heating rate, and lastly, the strain rate, in this specific order. For example, 150C-100C4h-F-0.01 corresponds to the test performed on the 100C4h temper, fast-heated to 150 °C and tested at a strain rate (SR) of 0.01 s^{-1}.

3.2.3. Stage 3 – Warm Formability Characterization

In the third stage of the experimental program, a narrowed selection of the Gleeble testing conditions were adopted to perform warm forming experiments using plane strain Nakazima specimens in order to assess the effect of temper, forming temperature and heating rate, and punch speed on warm formability. The thermo-mechanical process history for the selected forming experiments is common to that considered in the Gleeble experiments in Stage 2 (Figure 24), with the exception that punch speed replaces strain rate in the diagram. Figure 27 shows the test matrix corresponding to the Stage 3 experiments, in which the different punch stroke rates, temperatures and heating rates for the three temper conditions are outlined. The motivations for the selection of these test conditions is presented in Section 4.2. Up to four repeats were done for each condition (only three repeats if the first three experiments exhibited good repeatability).

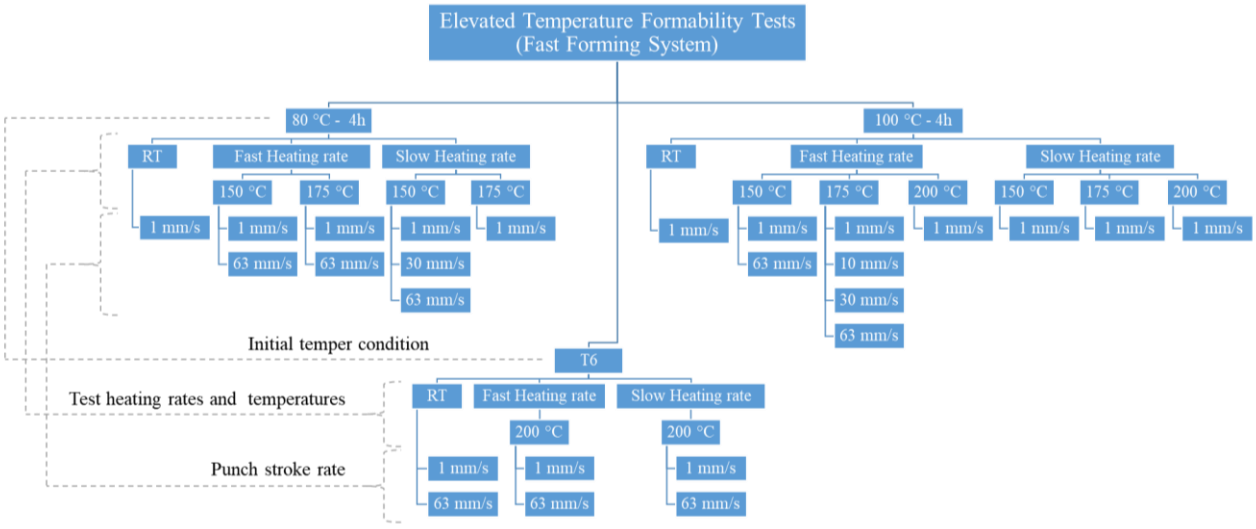

Figure 27. Stage 3 – warm forming test matrix.

Similar abbreviations were used to describe the test conditions of this stage, except the strain rate designation was replaced by the appropriate stroke rate. For instance, 175C-80C4h-S-1 (mm/s) refers to the (Nakazima) formability test, performed on a (plane-strain) specimen with an 80C4h temper, slow-heated to 175 °C and tested at a stroke rate of 1 mm/s.

3.2.4. Stage 4 – Final Hardness Following PBC

As the fourth and final stage of this investigation, hardness tests were performed on selected pre-and post-paint baked warm formed specimens, extracted from the flange and formed (10% strain) regions of the Nakazima samples. The process diagram and test matrix for this final stage are shown in Figures 29 and 28, respectively. The paint bake cycle comprised a single heat-treatment step at a temperature of 177 °C for a duration of 30 minutes.

Further, the specimens were exposed to an additional one day of natural aging prior to the micro-hardness testing. This period at room temperature corresponds to the curing time of specimen holders (epoxy pucks), necessary for mounting the specimen on the test apparatus. This aging step , however, can be neglected given the findings on the stability of similar tempers evaluated by Österreicher *et al.* [56] (discussed in Section 2.1.3).

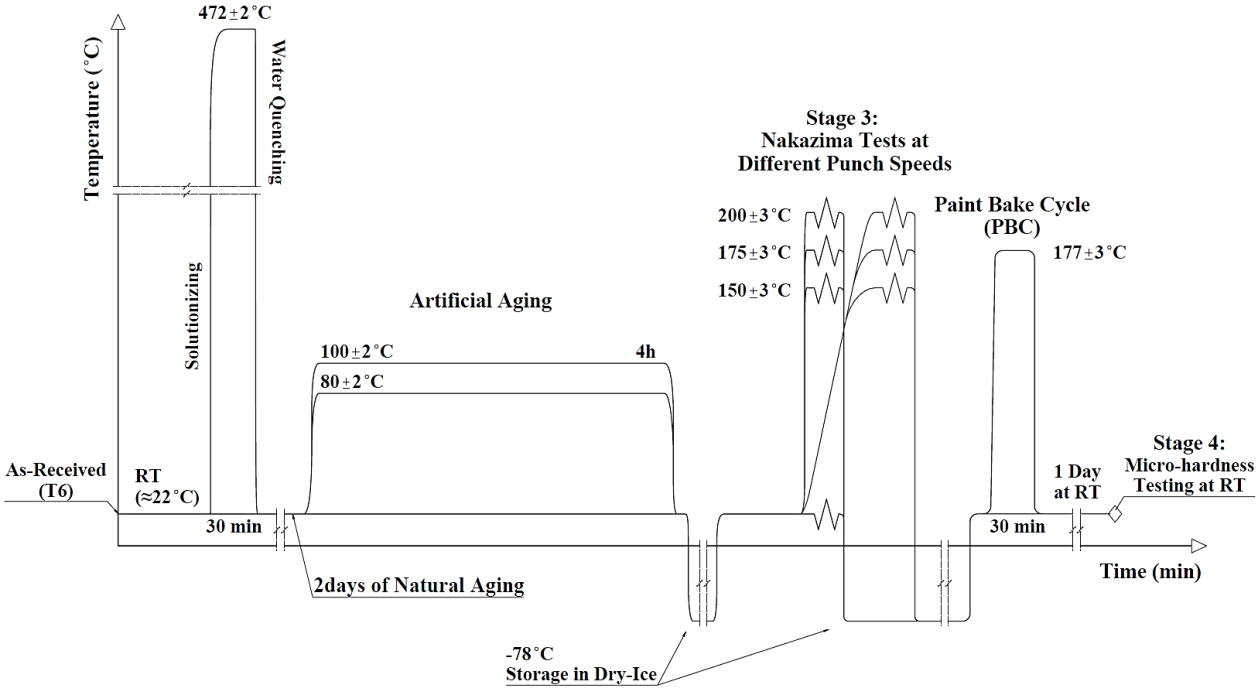

Figure 28. Stage 4 – Process diagram of the hardness evaluation tests following the warm forming process.

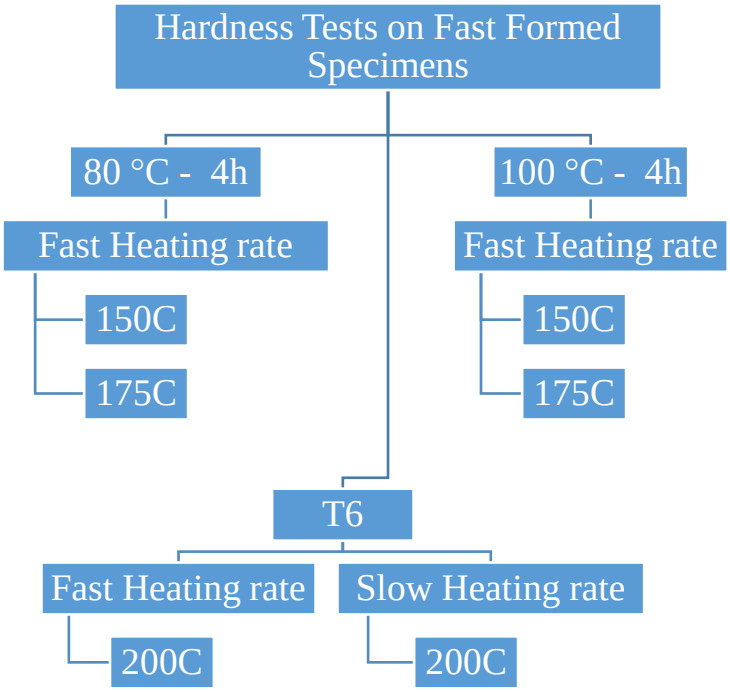

Figure 29. Stage 4 - final hardness test matrix.

3.3. Room Temperature Mechanical Testing Methods

3.3.1. MTS Tensile Testing Apparatus

Room temperature tensile testing for the Stage 1 experiments was performed on a 100 kN MTS Criterion 45 servo-electric tensile frame, equipped with a 3D DIC system, as shown in Figure 29. Note that the DIC system is described in Section 3.5.

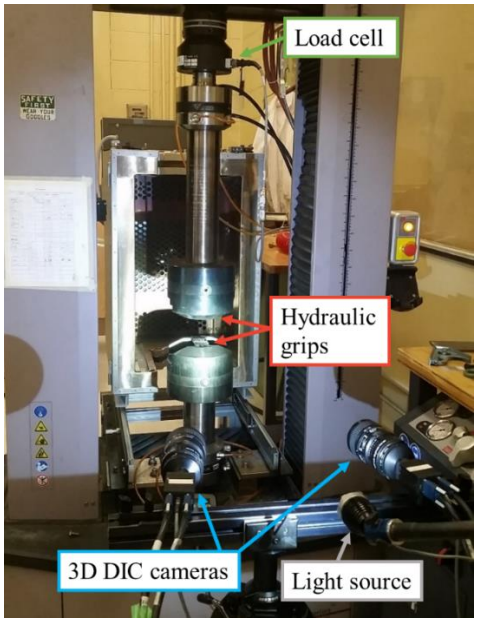

Figure 30. Room temperature tensile frame.

The standard ASTM E8 geometry [105] was utilized for room temperature tensile tests. This geometry is displayed in Figure 30. The rolling direction was oriented along the tensile straining direction, as specified in the ASTM standard. The crosshead speed for the MTS tensile frame was adjusted to achieve a nominal strain rate of 0.01 s^{-1}.

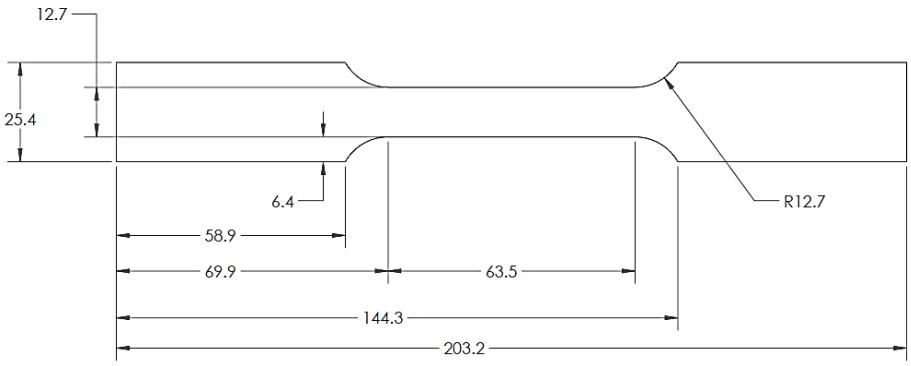

Figure 31. ASTM E8 tensile specimen [105] *used for the room temperature tensile experiments in Stage 1.*

3.3.2. MTS Dome Tester Apparatus

The room temperature formability studies (Stage 1) were performed on the MTS formability press (dome tester) shown in Figure 31. A 3D DIC system was also available with this hydraulic apparatus to extract the full field strain distribution on the formed specimen.

A Nakazima [86] punch with a diameter of 101.6 mm (4”) was used in a flat (no lock-bead) die-set with binder and die opening diameters of 116 mm and 105.6 mm, respectively. The die entry radius was approximately 6 mm. A clamping force of 640 kN was input into the supervisory (LabVIEW) software, and the punch speed was set to 0.5 mm/s.

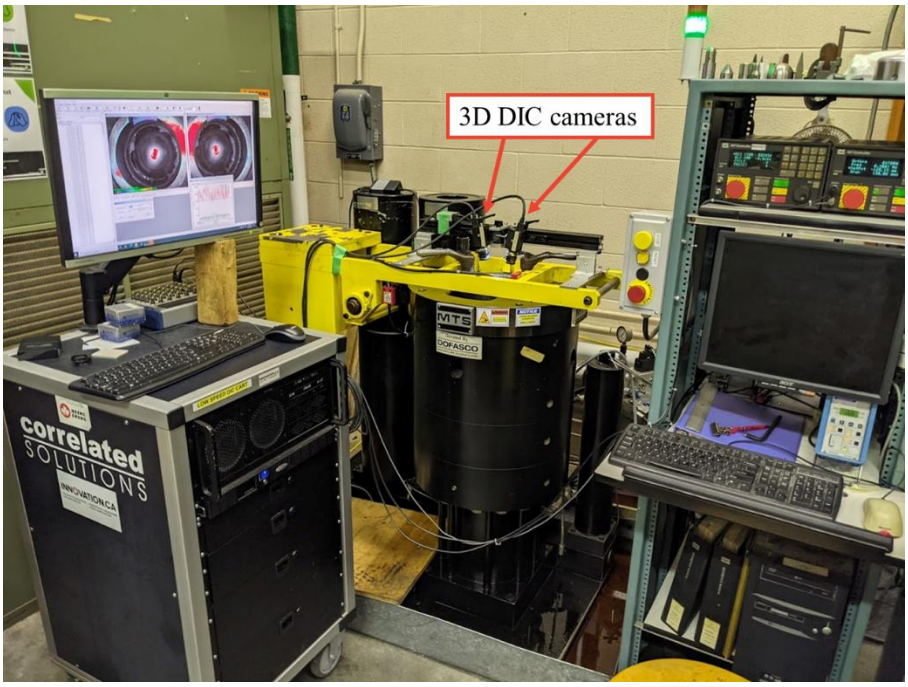

Figure 32. MTS dome tester apparatus.

The plane-strain (PS) loading state, normally signifying the limiting state (lowest formability) of a typical forming process (as illustrated in Figure 16), along with the standard ISO12004-2:2008 [91] necking detection method, were selected to compare the formability of the different tempers and forming conditions. To reduce friction, four layers of Teflon sheets with Vaseline lubrication between each layer was used between the punch surface and the blank.

The adopted specimen geometry, shown in Figure 32, was utilized in accordance with the ISO 12004-2: 2008 recommendations [91], and was used to capture the plane strain loading condition. This design was optimized to achieve improved geometrical stability, avoiding failure at the die entry radius, as verified by experimental results. Furthermore, the specimen major axis was selected to be aligned with respect to the transverse direction, since experimental results from DiCecco [106] and Pishyar *et al.* [85] demonstrated that the transverse direction was the limiting direction.

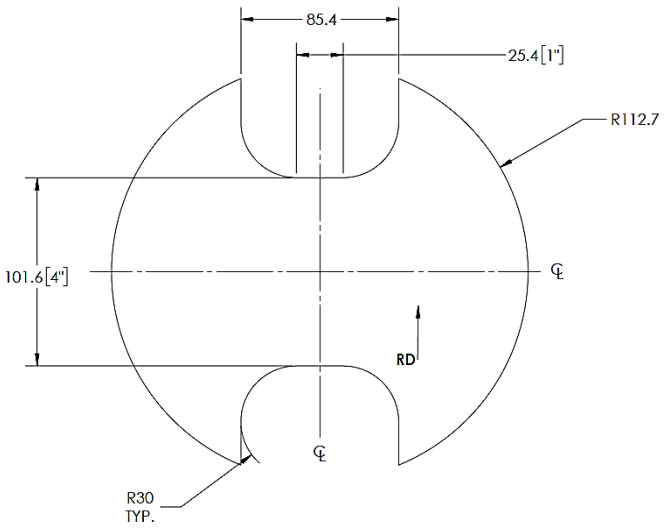

Figure 33. Nakazima dome specimen geometry (referred to as the "Batarang" geometry) [91].

3.4. Elevated Temperature Mechanical Testing Methods

3.4.1. Gleeble 3500 Tensile Testing Apparatus

Elevated temperature tensile testing (Stage 2), considering a range of testing temperatures, heating rates and strain rates, was performed using a Gleeble 3500 thermomechanical simulator. This apparatus utilizes a closed-loop electrical heating circuit with the capability of rapidly increasing the specimen temperature. In addition, to achieve a more constant strain rate, the high-pressure mode was activated for all of the tests performed on this setup. The Gleeble apparatus is shown in Figure 33.

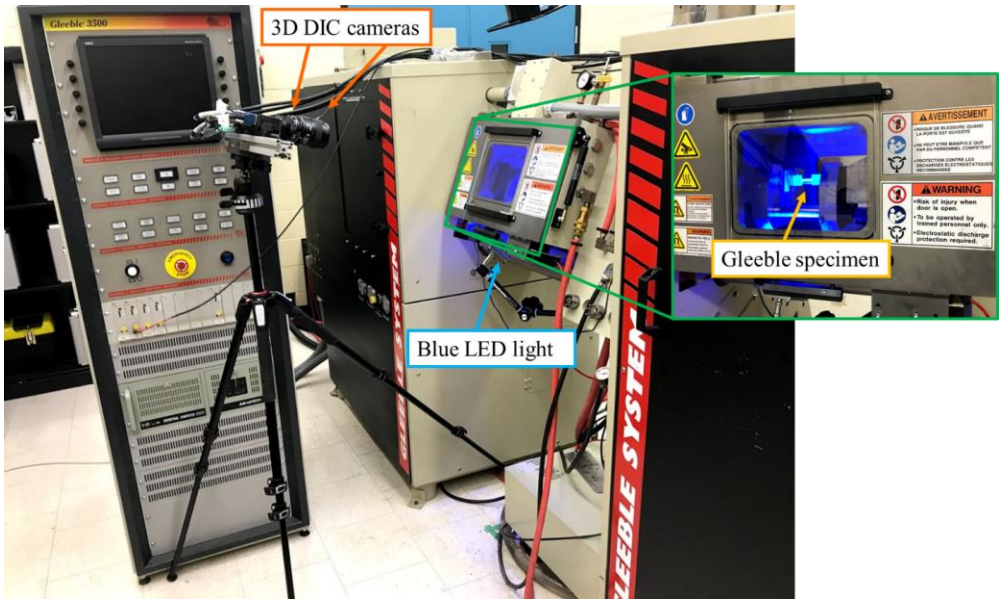

Figure 34. The Gleeble 3500 with the DIC system.

The Gleeble apparatus utilizes a resistive heating method in which AC current flows into the specimen through the cooled grips. This gripping and heating arrangement, along with the high thermal conductivity of the aluminum samples, introduces an undesirable thermal boundary condition, resulting in a significant gradient in temperature along the length of the specimen. Typically, the temperature at the centre of the specimen is roughly 20 °C higher than at the grip regions, as shown in Figure 34 – left hand graph. This temperature gradient results in a lack of strain uniformity within the gauge section of the specimen. Therefore, modifications to the boundary conditions (gripper contacts) were made, resulting in noticeable improvements as shown in Figure 34. The details of the corrective measures are discussed in further detail in Appendix B.1.

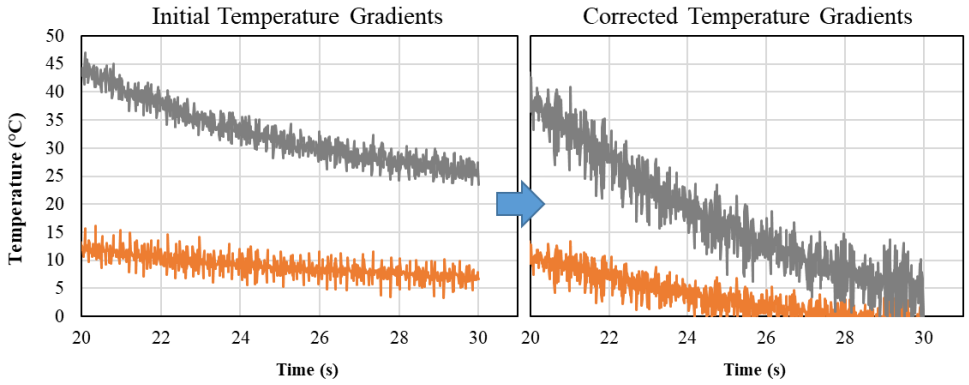

Figure 35. The difference in temperature between the set/desired temperature (which is achieved at the center of the specimen), 5 mm away from the center (Orange), and the furthest end of the gauge region (Grey). The improved temperature difference in response to the boundary condition modifications are displayed in the right-hand graph.

Given the adverse effects of the temperature gradient along the length of the specimen on the resulting strain distribution, the Area Reduction Method (ARM) was implemented to obtain localized strain data at the centre of the specimen. This implementation and validation of the ARM strain measurements are presented in Appendix B.2.

Additionally, given the thermal softening effect (presented in Chapter 4.2) and the resulting high sensitivity to minor setup misalignments, a modified version of the standard mini JIS (MJIS) tensile specimen was designed in collaboration with Lu [107]. Figure 36 displays the dimensions of this modified JIS geometry. The methodology for ensuring representative data is further discussed in Appendix B.

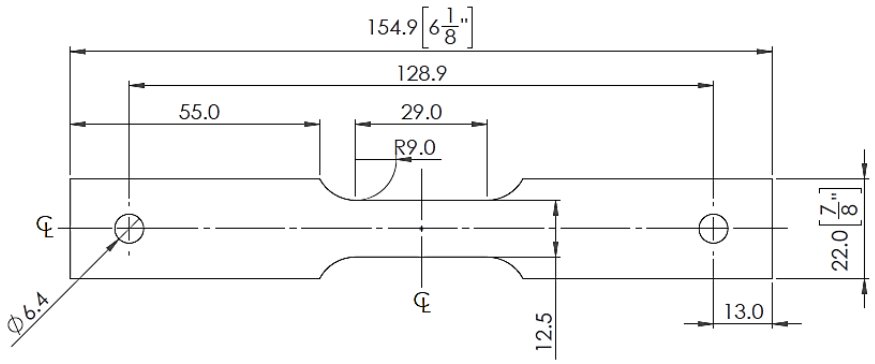

Figure 36. Modified JIS geometry utilized on the Gleeble apparatus.

3.4.2. Warm Forming Experiments

The elevated temperature formability experiments (Stage 3 experiments) utilized the warm Fast Forming System (FFS) that was recently developed at the University of Waterloo by George [108], shown in Figures 37 and 38. This system was used to evaluate the warm formability of a range of pre-aged tempers and test conditions, listed in Figure 27. Two furnaces are available to achieve different heating rates, namely a conventional DelTech convention furnace and a Can-Eng platen (or contact) furnace. Furthermore, an ABB robotic arm was used to rapidly and consistently load/unload the specimens into/out of either furnace, and subsequently load into to the heated forming tooling.

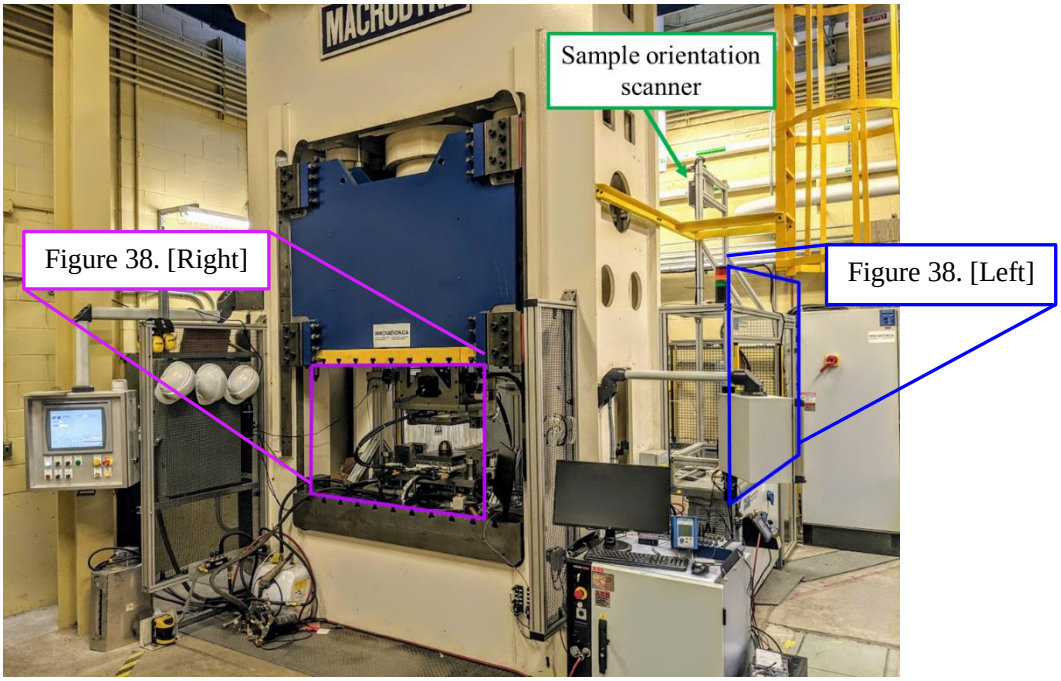

Figure 37. The automated warm forming system, George [108].

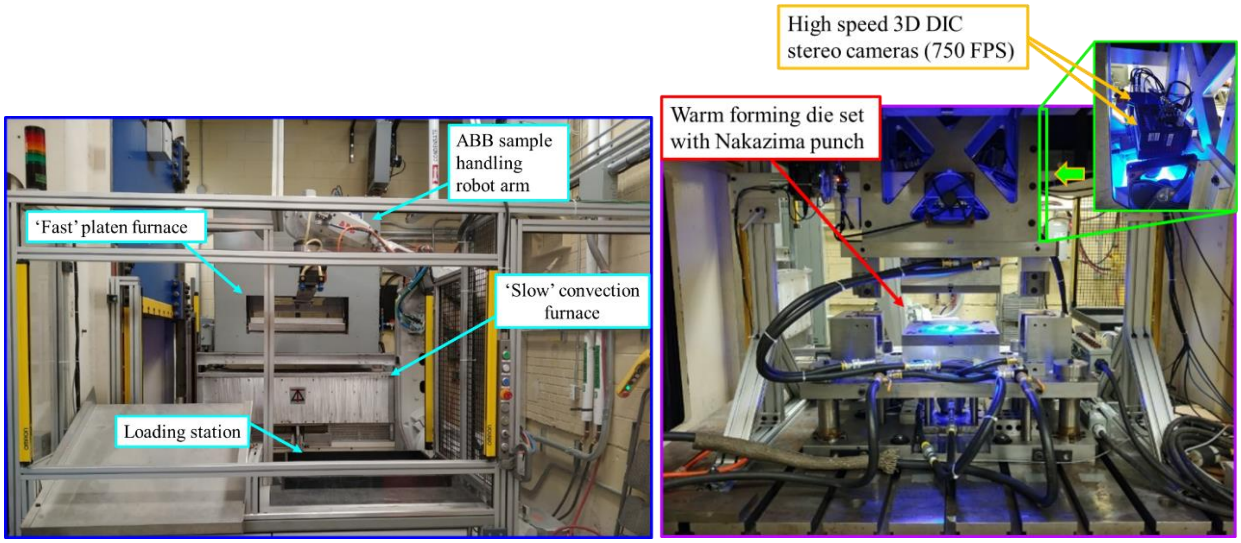

Figure 38. [Left] Furnaces and the sample transfer system. [Right] Forming and data acquisition systems, George [108], *DiCecco*[106].

The warm forming tooling (Figure 39) utilized a heated Nakazima punch, with a diameter of 101.6 mm (4”), that matches the punch diameter used in the room temperature MTS dome tester setup (Section 3.3.2). The plane strain specimen geometry, Figure 32, was also common to the room and elevated temperature forming experiments. The die and binder opening diameters were both 112 mm with a die entry radius of 8 mm.

The tooling is actuated within a high speed hydraulic press (manufactured by Macrodyne). The press has a 600 Ton main slide and a 300 Ton outer slide. The outer slide was not used in the current experiments. For the current experiments, the main slide was operated in a fast approach mode that can achieve a closing speed of approximately 170 mm/s at 60 Ton maximum force. The adopted closing speed for the faster experiments was limited to 63 mm/s to ensure a nearly constant velocity.

A clamping force of 40 tons (~392 kN) is applied via a hydraulic cushion available on the large Macrodyne press system to fully clamp the specimen between the die and binder tooling and avoid draw-in during the forming process. A selection of punch speeds, ranging between approximately 1 mm/s and 63 mm/s, were used to evaluate the rate sensitivity of the specific tempers and test conditions, for comparison with the data obtained from the Gleeble apparatus (Stage 2 experiments). In all tests, a low friction condition was achieved using four layers of Teflon sheets between the punch tip and the blank. No Vaseline was utilized between the Teflon sheets in these experiments to avoid any smeared residues on the tooling, especially given the insignificant improvements it offered, as determined by experimental results.

All tooling components (binder, punch, and upper die) were heated to the target test temperatures, simulating an isothermal forming condition, with temperature feedback using embedded thermocouples placed close to the contact surface with the blank. The punch tip thermocouple location is indicated in Figure 39. Additionally, a pyrometer, integrated into the warm forming system, was utilized to validate the starting blank temperature immediately before triggering the forming step. All temperature settings and thermal validation studies are presented in Appendix A.3.1.

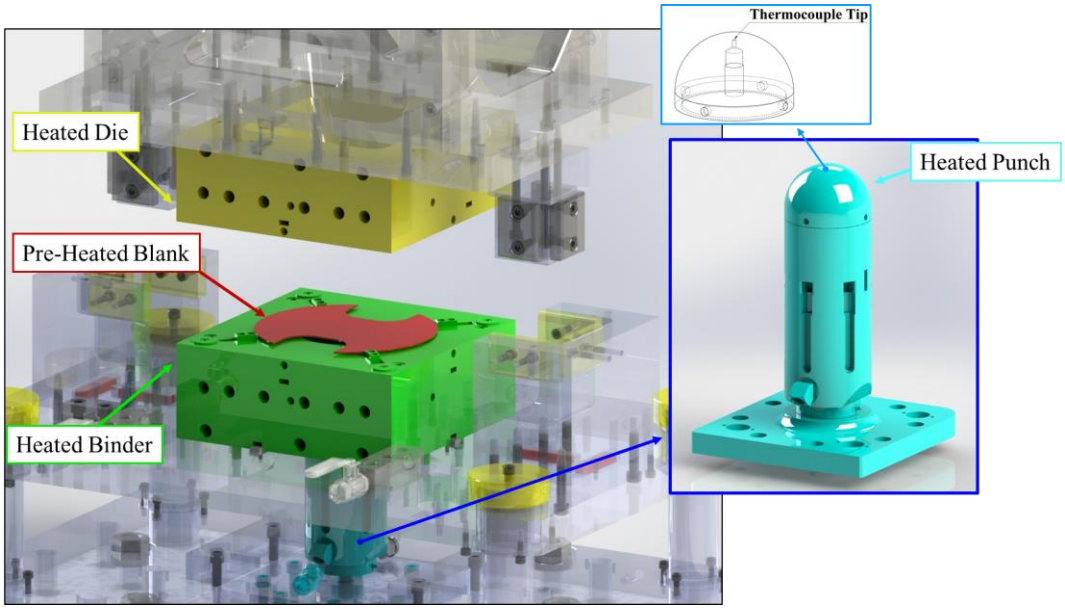

Figure 39. Heated tooling and the specimen positioning on the FFS, George [108].

The punch was mounted on a stationary post while the die is mounted on the press main slide. The binder is mounted on the hydraulic cushion which operates under load control to clamp the sheet metal specimen to the die (while translating) during the press stroke. Further, spring loaded lifters (or positioners) serve to position the blank and hold it above the tooling surface prior to die closure. The specimen is first clamped against the binder and then formed over the stationary punch due to the motion of the press slide and die (see Figure 41). One advantage of this tooling arrangement is that the punch position is constant such that the focal distance between the tip of the punch (and specimen) and camera lenses (also stationary) is constant, maintaining image quality over the entire forming stroke.

CAD images displaying the tooling in isolation and the motion during the forming cycle are shown in Figure 40. The key process parameters for the warm forming tests are presented in Table 3 and displayed graphically in Appendix A.3.2. The temperature profiles over the duration of the tests (achieved by the two furnaces and the heated tooling) were planned to roughly reproduce those of the Gleeble tests.

However, some inherent variations existed between the two setups. The specimen removal time from the furnaces (roughly 6 s, corresponding to both furnaces), specimen transfer times from the furnaces to the die-set positioners (roughly 6 s), and die closure periods (2 to 13 seconds corresponding to the different test speeds), introduced the largest source of difference. The time

required for the robot to retract and clear the forming die-set was roughly 2 seconds, and is included in the die closure period. In the duration of these steps, the specimens were exposed to convectional heat transfer (to ambient air) for 14 to 25 s (4 to 15 s longer than what the Gleeble specimens experienced). As listed in Table 3 and shown graphically in Figures 93 - 96, the specimen temperatures, immediately before the clamping stage, had dropped below the target forming temperatures (up to roughly 10 °C), especially for the slower stroke rate tests (although the blank temperatures would later increase somewhat after contact with the heated dies during forming). Also, the Gleeble system utilized a constant heating rate of 20 °C/s (which translates to 7.5 – 10 s of heating time for the different forming temperatures), whereas the FFS was programmed to achieve the warm forming temperatures in approximately 8 s across all test temperatures. These differences represent a potential source of error when validating the constitutive models using the numerical models presented in Chapter 5 of this thesis.

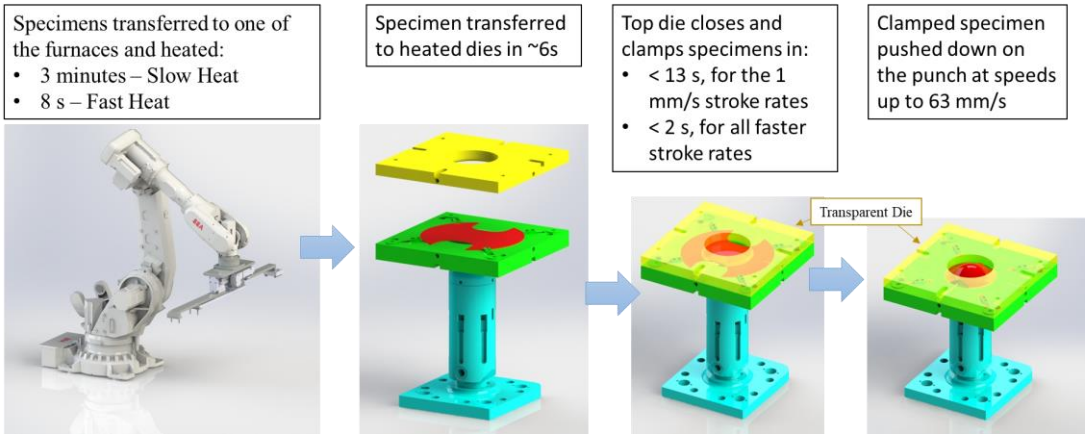

Figure 40. Isolated Fast Forming process, George [108].

Figure 41 demonstrates this forming process in more details, viewed from the section planes.

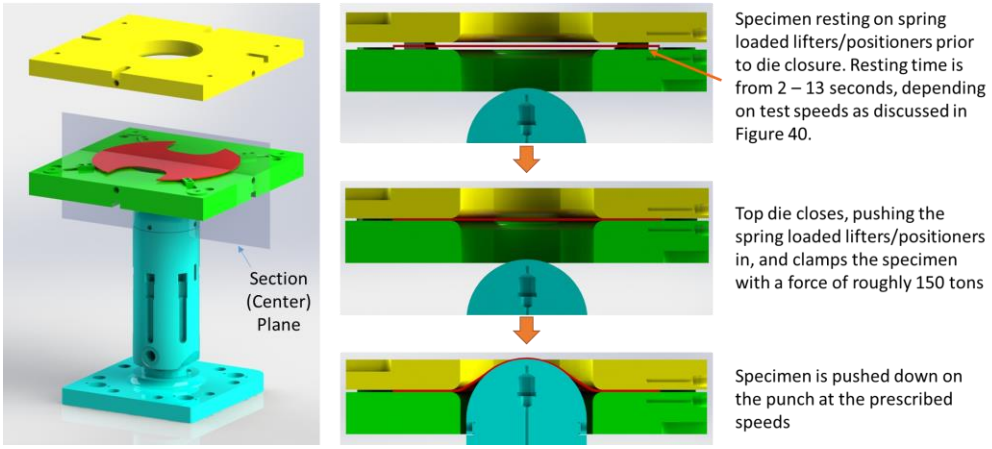

Figure 41. Detailed section view of the forming process.

Table 3. FFS test parameters. The listed values correspond to a representative test for each process route, and are rounded to the nearest integer. All other parameters are common to all warm forming tests, performed on this apparatus and are included in the text (above).

Forming temperatures (°C)	Heating period (s)	Stroke rate (mm/s)	Die and Binder temperatures (°C)	Punch temperature (°C)	Blank temperature when placed on positioners (°C)	Die closure period (s) (starting from the placement of specimen on positioners)	Blank temperature immediately before die closure (°C)
RT	N.A.	1	22	21	20	13	20
		63	21	22	20	2	20
150	8 (Fast Heat)	1	150	152	156	13	145
		63	150	151	150	2	149
	180 (Slow Heat)	1	150	156	156	13	144
		10	150	156	149	3	145
		63	150	153	153	2	149
175	8	1	175	178	181	13	168
		10	175	178	178	3	175
		30	175	179	178	2	175
		63	175	179	175	2	171
	180	1	175	180	180	13	168
200	8	1	200	205	201	13	190
		63	200	204	204	2	200
	180	1	200	207	208	13	195
		63	200	210	191	2	189

The approximate distances between the specimen and the tooling is presented Figure 41.

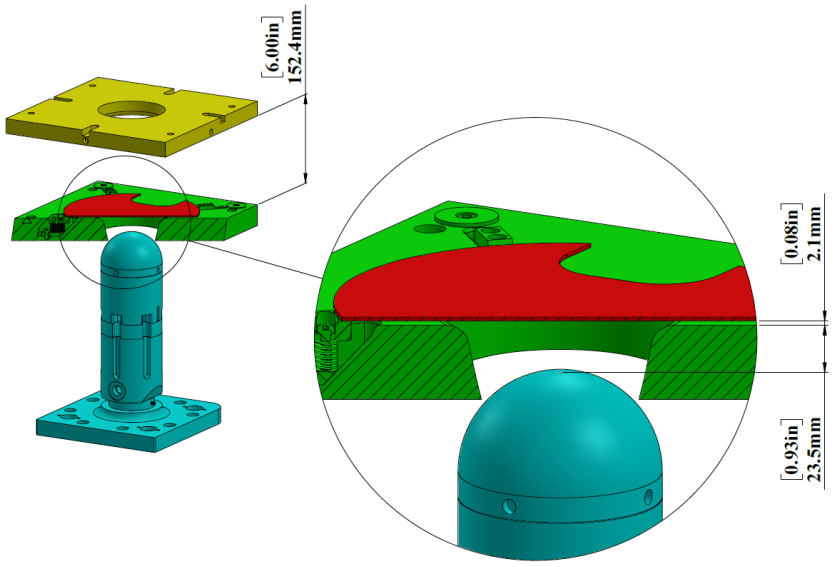

Figure 42. Relative position of the specimen from the tooling surfaces, George [108].

3.5. DIC Analysis

3D digital image correlation (DIC) systems, provided by Correlated Solutions Inc, were utilized throughout this study to obtain full field strain measurement over the duration of the tests. This non-intrusive technique tracks the motion of high-contrast speckle patterns on deforming specimen surface during a test, to determine local deformation, as described by Sutton *et al.* [88].

Random high-contrast speckle patterns, as shown in Figure 42, were obtained by spraying black paint on top of a white background. The specimens tested at room temperature were painted with the Painter's Touch 2X Primer spray paints, while the specimens tested at elevated temperatures were sprayed using the VHT FlameProof Coating. Two layers of white paint were applied, allowing approximately 5 minutes for drying of each layer. The black speckles were then sprayed on from approximately 20 cm away, as illustrated in Figure 43, with the nozzle perpendicular to the specimens laid flat in a paint booth (spray paint standing upwards on paint booth surface).

Figure 43. A tensile sample with black speckles on a white background, used to track the deformation of the gauge region using DIC.

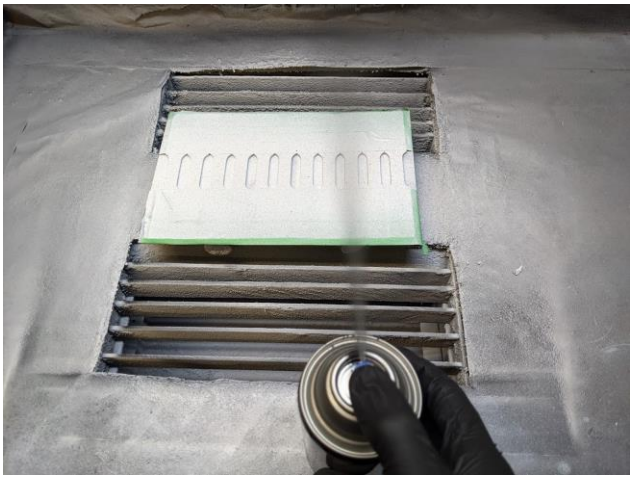

Figure 44. Speckling the tensile specimens with the black spray paint.

3.5.1. Camera and Lighting Setups

The MTS Tensile and Dome Tester apparatuses utilized a pair of mid-speed FLIR Grasshopper series cameras, capturing images at rates of up to 150 fps with a resolution of 5 MP. The FFS employed two high speed Photron AX100 cameras, capturing images at a maximum frame rate of 750 fps with a 1024 × 1024 pixel resolution. Lastly, the Gleeble apparatus used a pair of 2.2 MP cameras recording at a maximum frame rate of 280 fps.

The DIC systems employed on the Gleeble and FFS utilized a blue lighting technique which is commonly used, along with a blue light filter, to maintain a high-contrast monochromatic image in the presence of blackbody radiation, emitted from specimens at higher temperatures. While the current warm forming temperatures will not induce any additional light (glow), the blue light technique served to increase contrast, and was therefore utilized in this study.

3.5.2. Quality of DIC Strain Measurement

In order to develop a standard evaluation metric for the quality of DIC measurements, the Virtual Strain Gauge Length (VSGL), discussed by Rahmaan *et al.* [109], was employed. The VSGL is an indication of the resolution of strain in a given DIC setup and is calculated as:

$$VSGL = Resolution\ of\ the\ region\ of\ interest\ \times Step\ size \times Filter\ size \qquad \text{Eq [12]}$$

The resolution of the region of interest is measured as the average size (in mm) of the region divided by the corresponding number of pixels, in the longitudinal and transverse directions. The Step size and Filter size are variables used in the DIC software to extract the smoothed local strain values. Typical VSGL values for standard tensile and dome formability tests are within the range of 0.5 – 1 mm and 1 - 1.5 mm, respectively [106], [110].

The VSGL values of the DIC systems, employed on the MTS Tensile and Dome Tester frames were set to approximately 0.86 mm and 1.4 mm, respectively. Further, a VSGL value of 1.0 mm was utilized for the strain measurements on the Gleeble and the FFS. Table 4 list all relevant DIC settings for each test apparatus.

Table 4. DIC settings for the different apparatuses.

	Step size	Filter size	VSGL (mm)	Subset
MTS Tensile	3	5	0.86	19
MTS Dome Tester	5	5	1.4	35
Gleeble	4	5	0.96	27
FFS	2	5	≈1	21

3.5.3. Necking Detection and Strain Extraction Methods

The ISO12004-2:2008 [91] necking detection method was utilised to evaluate the forming limits of the plane strain Nakazima tests. It should be noted that although the ISO procedure specifically caters for room temperature tests, this failure detection method was utilized at a variety of warm forming temperatures, as well as for the RT experiments.

Furthermore, given the standard test geometry and procedures of the preliminary RT tensile tests (in accordance with ASTM-E8 [105]), and the resultant uniform strain distributions, the conventional strain extraction method (using virtual extensometers) was employed.

However, considering the non-uniform strain distributions along the gauge region of elevated temperature (Gleeble) tensile tests, although reduced slightly as mentioned in Chapter 3.4.1, the recommended standard strain gauge lengths were deemed unsuitable. Therefore the ARM was employed for the local strain extraction, as further described in Appendix B.2.

3.6. Hardness Measurements

Vickers micro-hardness measurements were performed on the warm formed specimens prior to and after forming, as well as following a subsequent paint bake cycle. The measurements were performed on a Wilson Hardness 402MVD Microhardness Tester. The applied force on this apparatus was set to 1 kgf with 15 seconds of dwell time. Four separate measurements were performed on each test specimen to ensure repeatability. The PBC heat treatments were performed in the fluidized (sand) furnace.

4. Results and Discussion

This chapter presents the results of the experiments based on the methodologies laid out in Chapter 3. The results are presented in order by Stage within the test matrix:

- Stage 1 - Preliminary Room Temperature Studies of Effect of Pre-Age
- Stage 2 - Warm Constitutive Characterization of Selected Tempers
- Stage 3 - Warm Formability Characterization
- Stage 4 - Final Hardness Following PBC

4.1. Stage 1 – Preliminary Room Temperature Studies of the Effect of Pre-Age

4.1.1. Room Temperature Tensile Results

Figure 45 shows the room temperature engineering stress-strain response for the range of pre-aging conditions considered in Stage 1 of the test matrix (Figures 22 and 23). In addition to the pre-aged conditions, results for the as-received (AR) T6 temper, an as-quenched (W) and an as-quenched + 2 day naturally aged (2 day N.A.) temper are also shown for reference. The as-quenched temper is evaluated for the sole purpose of demonstrating the severity of its PLC effect. For clarity, only the "median curves" are plotted for each condition, as being representative of each thermal treatment. In general, the scatter in the data was relatively low, as illustrated in Figure 46 which shows the complete set of curves for two pre-aged conditions.

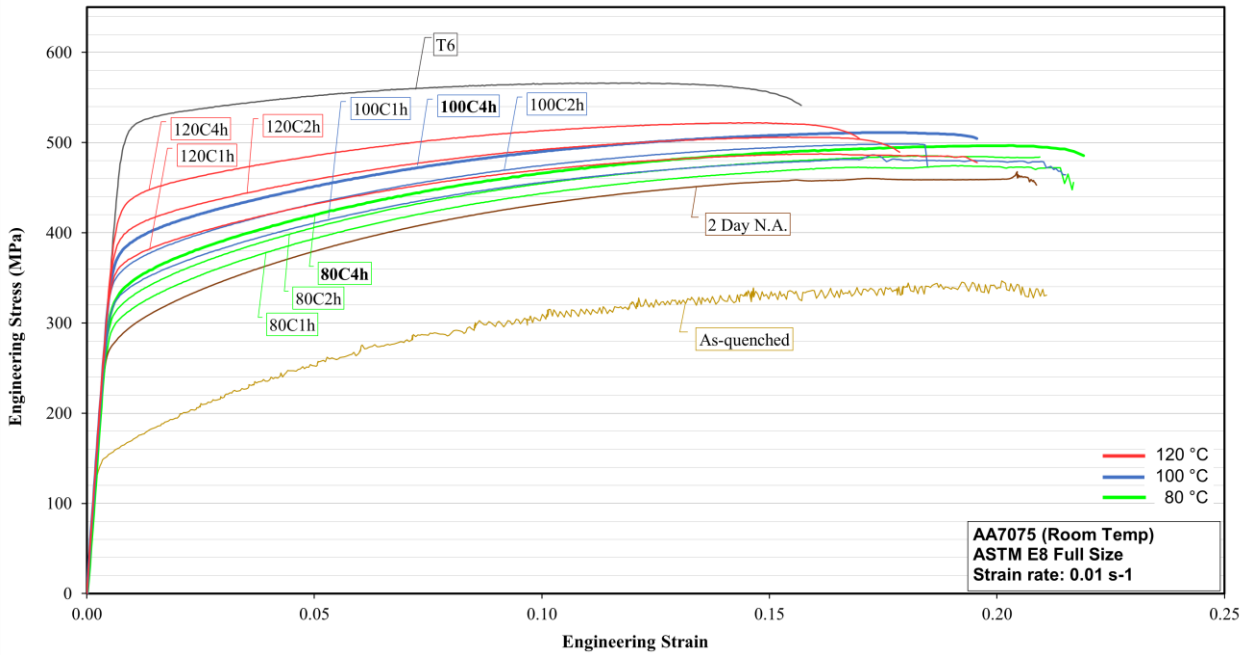

Figure 45. Engineering stress-strain curves corresponding to various pre-aging states.

From observation of Figure 45, for longer aging times at higher temperatures, the yield strengths approach that of the peak T6 temper, but the degree of work hardening is seen to decrease. Also, at low pre-aging states, higher dissolved solute concentrations promote PLC instabilities [48], as indicated by the observed serrated flow. The PLC type appears to be of type A, with the random serrations growing more apparent towards the end of the stress-strain curves. The PLC effects are reduced with higher levels of aging, while the largest PLC serrations are observed for the as-quenched or W-temper condition.

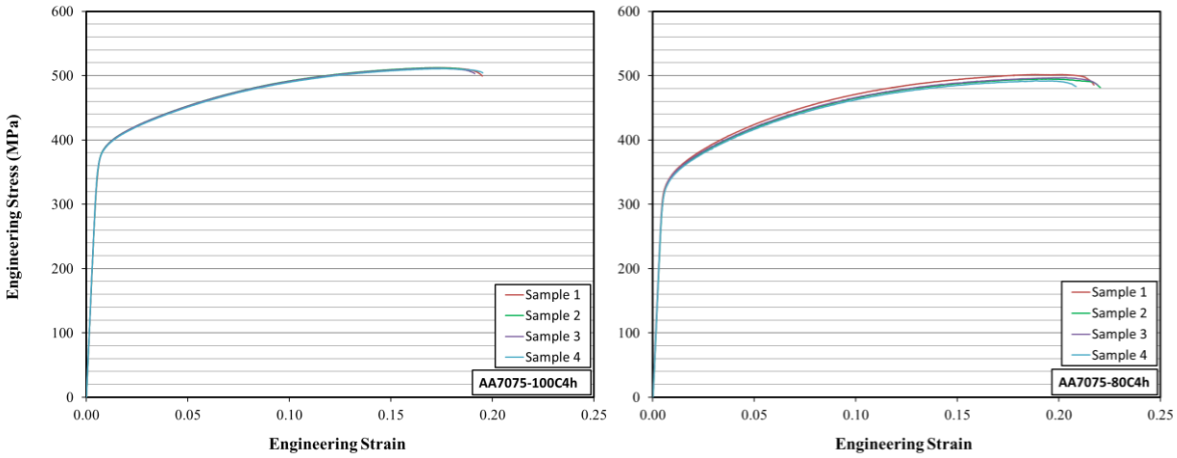

Figure 46. Illustration of the variability in engineering stress-strain data for the 100C4h [Left], and 80C4h [right] pre-aged tempers.

The degree of work hardening, measured here as the difference between the true stress at the uniform elongation (the strain at UTS) and yield strength, and the total elongation are displayed in Figure 47 a) and b) using the median curves in Figure 45 for each material condition. Both quantities are of interest as potential indicators of sheet formability performance. Evident reduction in the amount of hardening and associated reduction in elongation are observed as the degree of aging is increased. Plotting these quantities against each other for every temper, Figure 47 c), also clearly demonstrates this response.

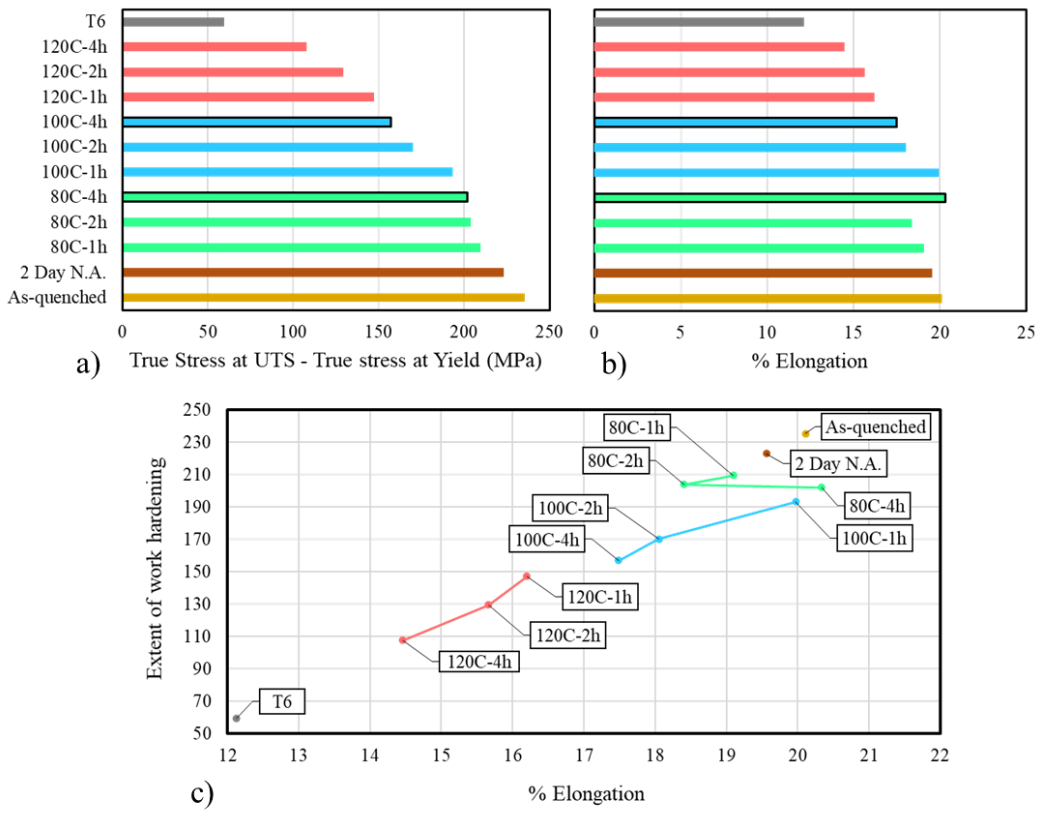

Figure 47. a) Extent of work hardening for each temper. b) Percent elongation of each temper. c) Extent of work hardening vs. percent elongation for each temper, grouped by aging temperatures.

In assessing which of the under aged (PA) tempers may be beneficial in improving the formability of AA7075, it is evident that the 80C pre-age treatments offer the highest degree of work hardening and elongation. In general, the 80C tempers exhibit the highest formability potential, in terms of these metrics, and the work hardening and elongation are highest for the shorter aging durations. In fact, the W temper (as quenched) and 2d-NA conditions exhibit the highest work hardening and elongation. It is important to note, however, that low aging

temperatures and durations result in tensile instabilities in terms of the PLC-induced serrated flow evident in Figure 45. The PLC behaviour also results in a reduced level of repeatability in the stress-strain response that can be seen by comparing the results for the 80C4h condition in Figure 46 [Right] *versus* that of the 100C4h temper [Left]. The 100C4h condition exhibited a muted PLC effect, and intermediate formability potential (work hardening and elongation).

4.1.2. Room Temperature Formability Results

Figure 48 presents the results of the room temperature Nakazima formability experiments in terms of the limiting major strain versus minor strain at onset of necking. It is evident from the plot that the minor strains are slightly positive, indicating that the specimen geometry resulted in strain states that were slightly more biaxial than a true plane strain condition (zero minor strain). The measured variability in the major and minor strains are also shown, from which the repeatability is seen to be approximately ± 0.015 strain for both components which is judged to be acceptable. The conditions closer to the peak aged state (longer aging times at higher temperatures) display reduced scatter, at the cost of somewhat reduced formability. The pre-aged tempers all exhibit a higher formability than the as received T6 condition.

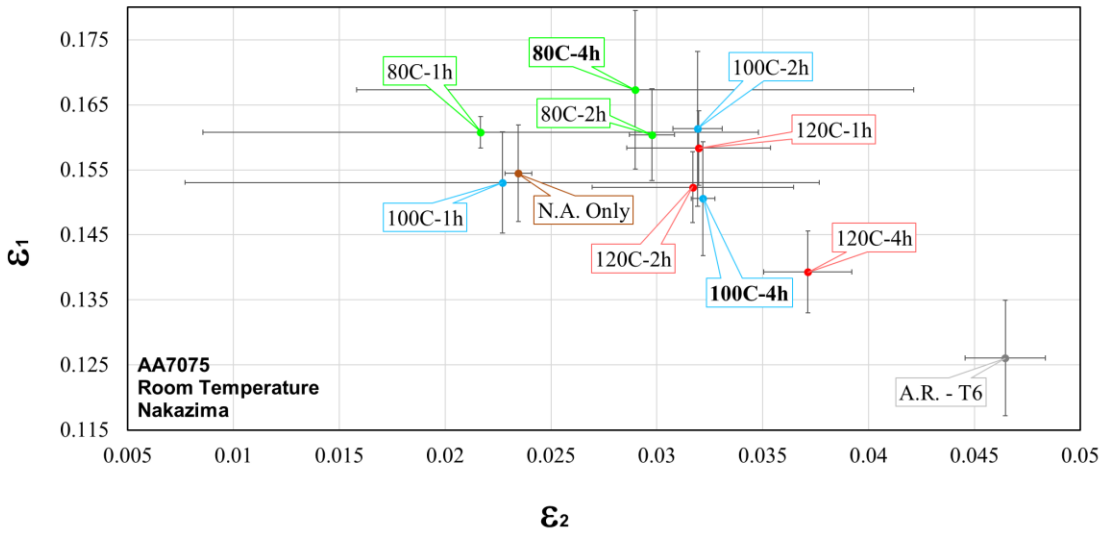

Figure 48. Forming limit graph with approximately plane strain data points of evaluated tempers. The error bars represent the standard deviation. ε_1 and ε_2 are the major and minor strains, respectively.

The effect of aging duration and temperature on the limiting major strain can be seen more clearly in Figure 49. In general, the major strain to onset of necking is not significantly affected

by aging duration for the 80 and 100 °C pre-aged conditions (for the durations considered and observed scatter). The 120 °C pre-age results in a loss of formability as aging duration increases to 4 hours.

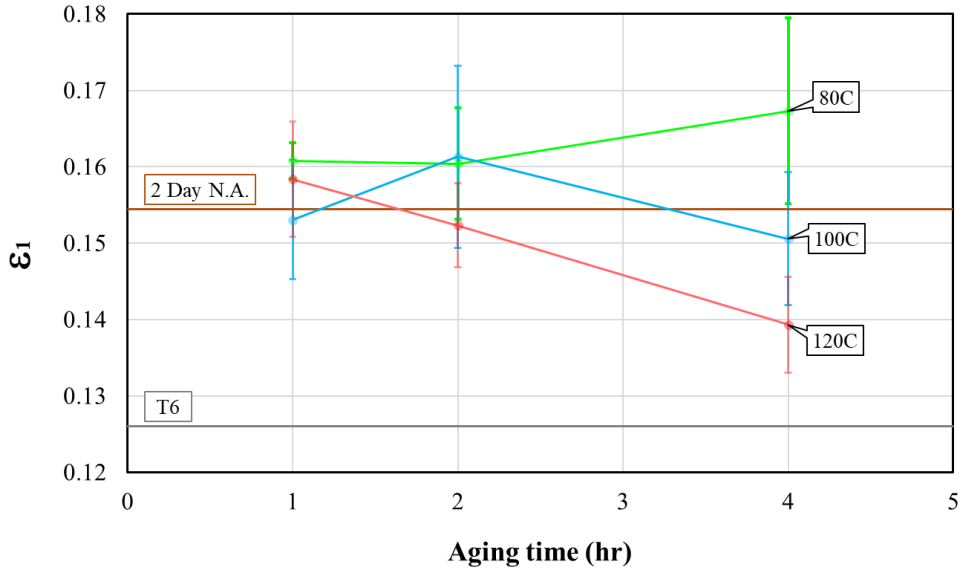

Figure 49. Major true strain (ε_1) vs. Aging time at each temperature. The 2 day N.A and T6 tempers are also included for reference. Note: Although major strains are selected as the indicators of higher formability limits in this study, the minor strains can also reveal important thinning characteristics (considering the plane strain loading condition).

In down-selecting the pre-age tempers for consideration in the subsequent warm constitutive characterization (Stage 2) and warm forming trials (Stage 3), it is evident that the 4h - 80 °C pre-aged temper displayed high formability (Figure 49), work hardening and elongation (Figure 47) with relatively mild PLC serrations (Figure 45), compared to the shorter duration aging periods at this temperature. As a result, this condition was selected for consideration in Stages 2 and 3 of this research. In addition, the 4h - 100 °C temper exhibited good formability, as well as a lower PLC response and was also selected. Figure 50 shows the original test matrix for the room temperature trials in Stage 1, in which the two down-selected pre-age conditions are highlighted. Note that the 120 °C pre-age conditions exhibited lower formability and were dropped from the subsequent stages of this work. The forming limit strains for the two selected conditions are overlaid atop the T6 FLC obtained by DiCecco [106] in Figure 51. The two reference temper conditions of T6 and 2 day N.A. are also shown in this figure for comparison purposes.

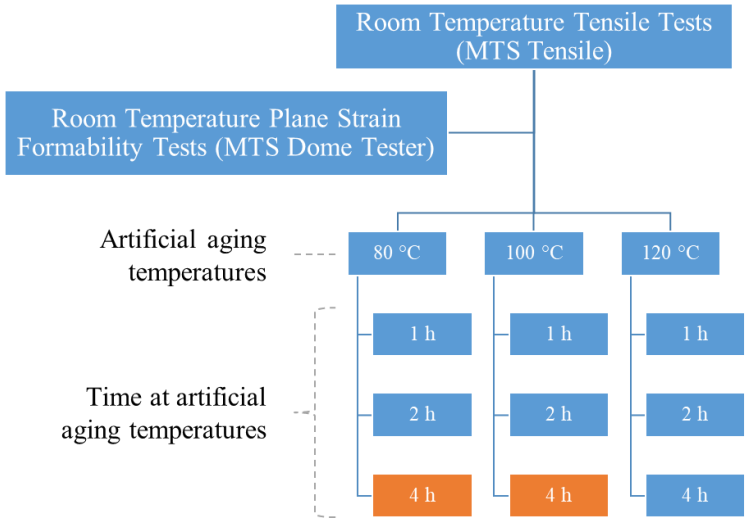

Figure 50. Pre-aged temper conditions selected from Stage 1 room temperature tests.

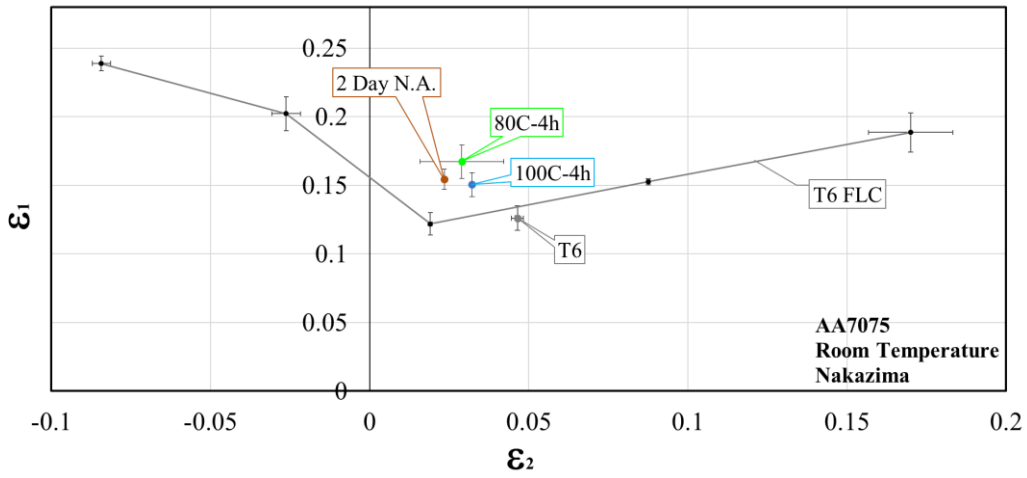

Figure 51. Forming limits of the selected PA conditions plotted against the T6 FLC due to DiCecco [106]. The error bars represent the standard deviations.

4.2. Stage 2 – Warm Constitutive Characterization of Selected Tempers

Elevated temperature tensile tests were performed at different strain rates on the reduced set of pre-aged tempers, namely a 4 h pre-age at either 80 or 100 °C. The as-received T6 temper was also included in this study for comparison purposes. The process parameters and the test matrix for this stage of testing are illustrated in Figures 24 and 25, respectively. The median curves were

utilized for this comparison study, with the same reasoning as that discussed in Stage 1 (Section 4.1).

As described in Chapter 3.2.2, the slower heating rate proposed in this study, corresponds to the heating time required for the test specimens to achieve steady state temperatures in a conventional warm forming apparatus. A limited number of tests were performed to examine the constitutive response under conditions corresponding to the slow heating approach.

Figure 52 shows the effect of elevated temperatures on the constitutive response of the three tempers for the lowest strain rate of 0.01 s^{-1}, and using the slow heating system. Figure 52(a) serves to show the reduction in yield strength of the peak temper (T6) condition with the increase of test temperature. The T6 material also exhibits the early onset of diffuse necking (corresponding to the UTS) at relatively low strain, as well as an increase in the post-UTS elongation relative to the RT response. Figure 52 (b) and (c) show the thermal softening that occurs for the two pre-aged conditions. The reduction in strength with temperature for the two pre-aged conditions is similar to that exhibited by the T6 condition, however, the pre-aged tempers exhibit strong work hardening at room and elevated temperature, indicating that the onset of diffuse necking at elevated temperatures are significantly delayed relative to the T6 response. The differences in the work hardening behaviour is evident in Figure 53 which compares the stress-strain response for each alloy at the three different test temperatures.

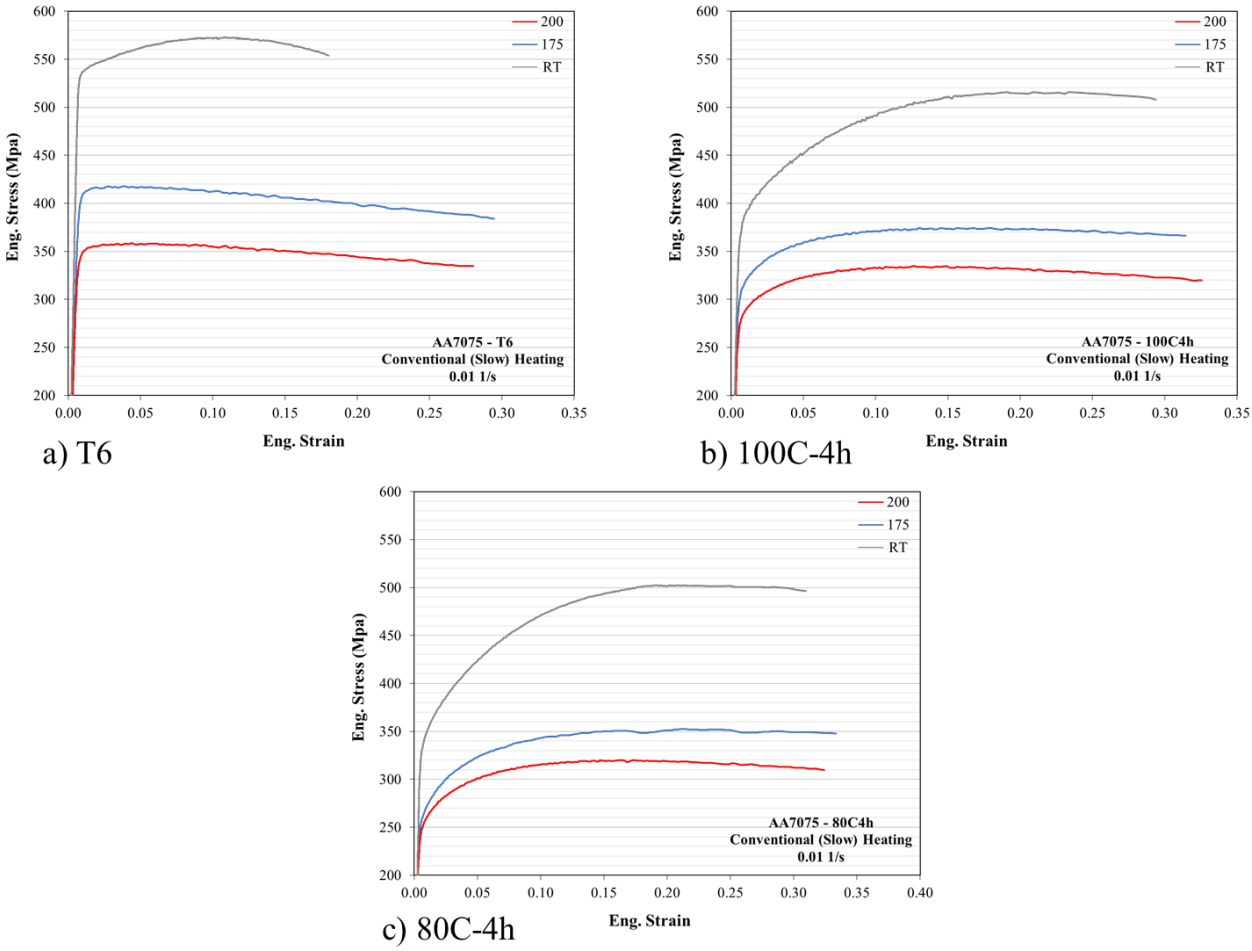

Figure 52. The thermal softening effect observed in the a) T6, b) 100C4h, and c) 80C4h tempers, heated to test temperatures using conventional heating rates.

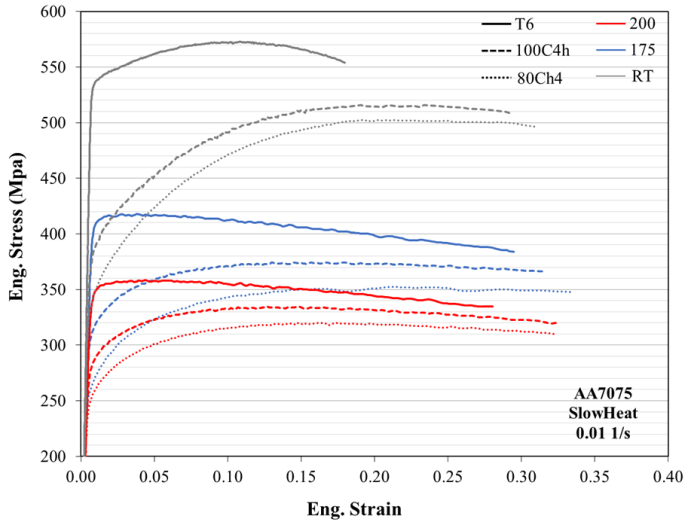

Figure 53. The thermal softening effect of all tempers heated at the conventional (slow) rates.

The strain rate sensitivity (SRS) for two initial tempers of T6 and 80C4h at the various temperatures is examined using Figure 54. Plotted are the true stress versus true strain curves for the T6 and the pre-aged temper, tested at various strain rates and test temperatures. At room temperature, the T6 temper (Figure 54 [Left]) has a slightly positive SRS, which agrees with the findings of Rahmaan *et al.* [111]. With an increase in test temperature, the T6 condition exhibits a strong positive SRS. Furthermore, a reduction in total elongation is observed with an increase in strain rate. Figure 54 [Right] shows the corresponding data for the 80C4h temper. The pre-aged temper also shows a reduction in elongation with an increase in strain rate at elevated temperature, although the increase in flow stress with strain rate is noticeably lower than that seen for the T6 temper.

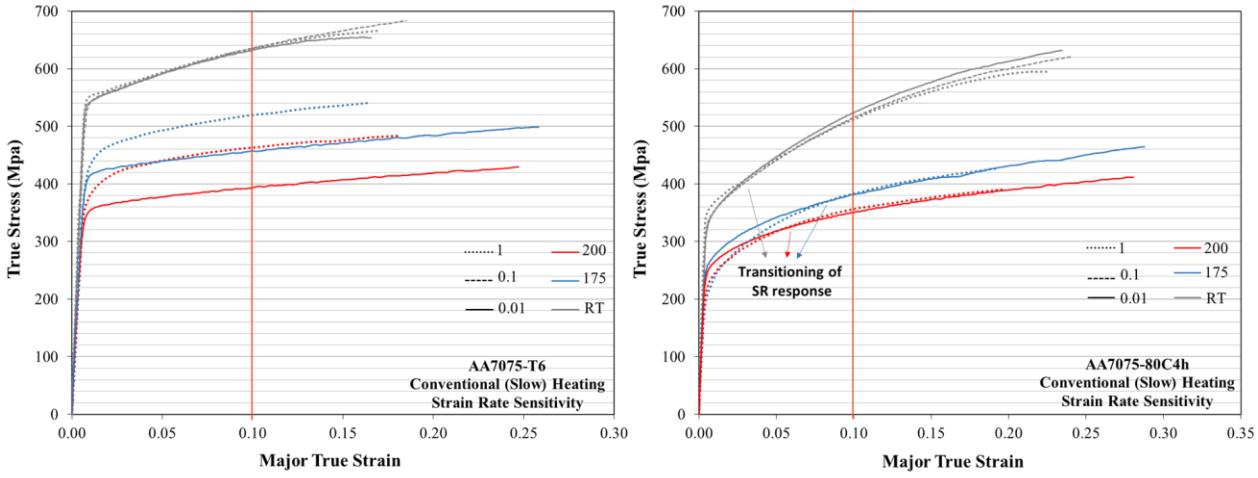

Figure 54. Effect of strain rate on the true stress versus true strain curves for the [Left] T6, and [Right] 80C4h tempers, heated to the test temperatures using conventional heating rates.

In an effort to quantify the strain rate sensitivities of the different tempers under the different test conditions, the true stress at approximately 10% plastic strain is plotted as a function of strain rate for each condition. These flow stress values correspond to the vertical intercepts with the orange line drawn at roughly 10% plastic strain in Figure 54. The resulting data is plotted in Figure 55 which uses a logarithmic scale for the strain rate axis in view of the expected exponential dependency of flow stress on strain rate [112]. As seen in Figure 55 [Left], the T6 temper displays a strong positive SRS at elevated temperatures. In contrast, the pre-aged temper exhibits a rather low SRS at elevated temperatures (nearly zero) and a negative rate sensitivity at room temperature.

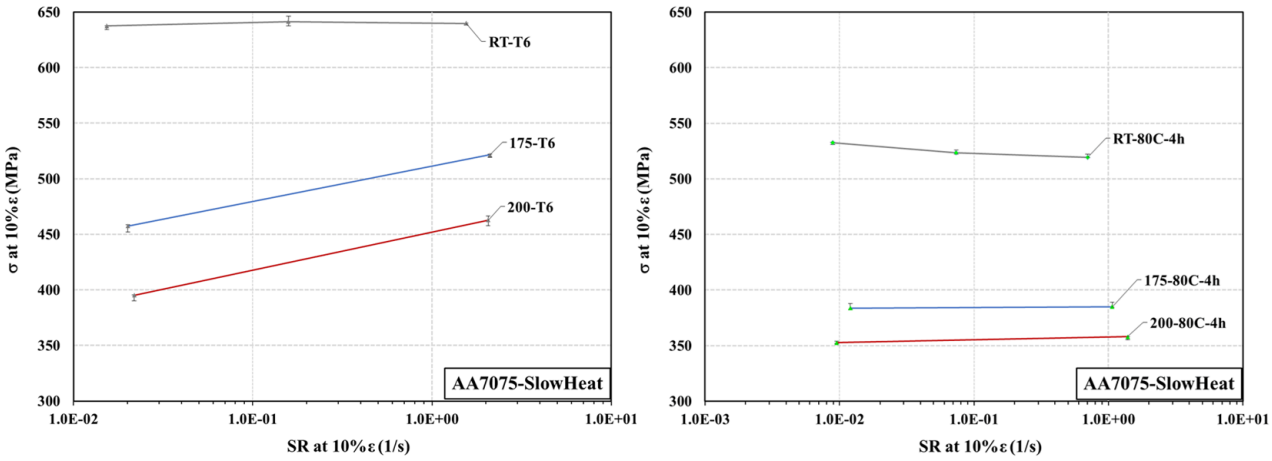

Figure 55. The strain rate sensitivity of the [Left] T6, and [Right] 80C4h tempers at the different temperatures, heated using conventional (slow) rates, measured by the true stress values at roughly 10% plastic strain. The error bars represent the maximum deviations from the median results.

The effect of heating rate on the engineering stress-strain response of the three tempers can be seen by examining Figure 56. In general, the T6 condition displays mild over-aging in response to the reduced heating rates, indicated by the reduction in engineering stresses [31], for the range of conditions tested (Note that not all heating rates, temperatures and strain rates were tested for all initial tempers due to the large amount of testing that would be required). The pre-aged (under-aged) tempers do show differences between the stress-strain response for specimens using slow *versus* fast heating. The effect of fast heating is to reduce the extent of aging while the sample is heated prior to warm tensile testing which in turn reduces the increase in yield strength during heating. As a result, the fast heating stress-strain curves lie below the slow heating curves for the same temperature and strain rate. This effect is most pronounced for higher temperature testing and is more evident for the 80C4h pre-aged temper (Figure 56 c) compared to the 100C4h condition (Figure 56 b). In general, the reduction in yield strength and greater extent of hardening for the fast heating conditions is expected to promote increased formability, as investigated in Section 1.3.

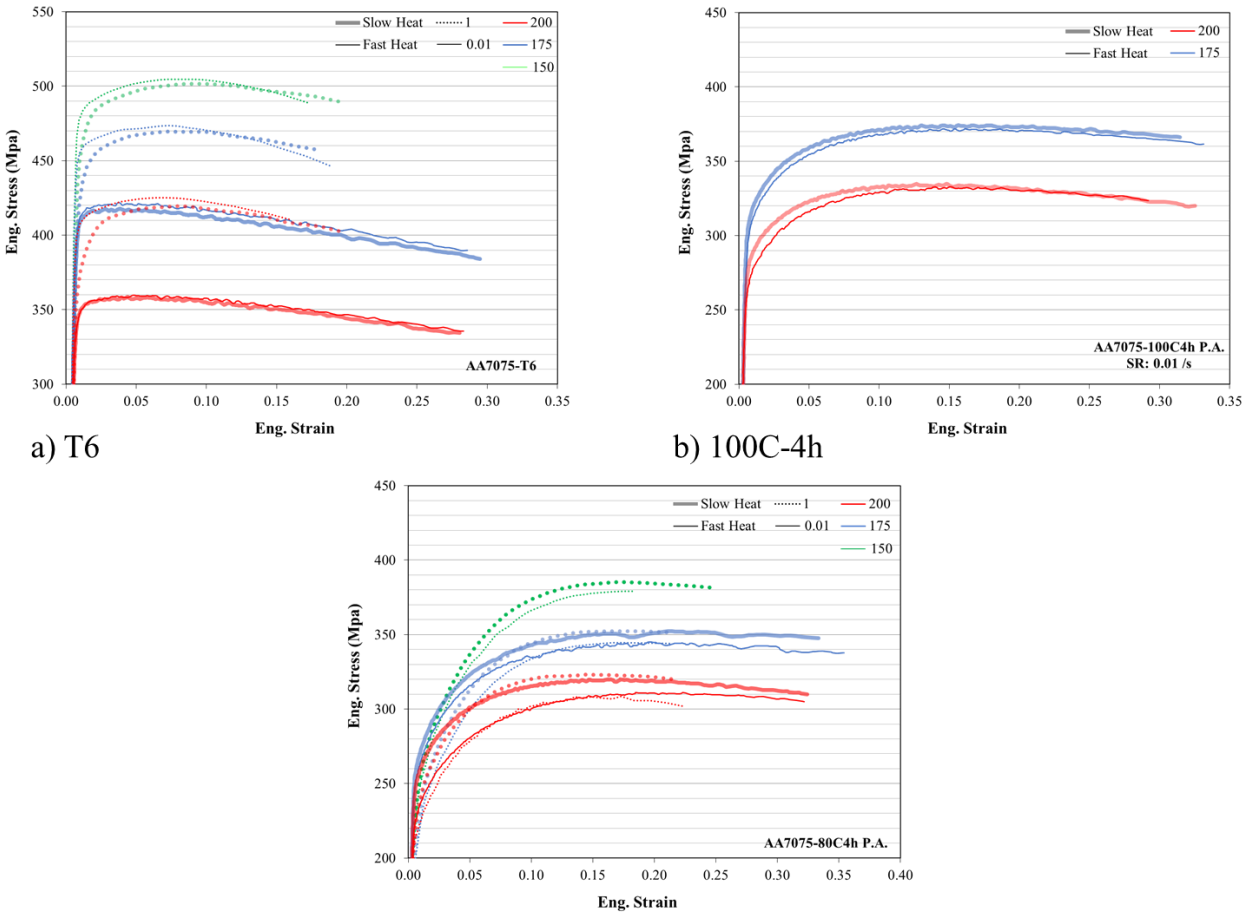

Figure 56. The engineering stress-strain curves of the three different tempers, demonstrating the effect of heating rate on the yield strength and subsequent hardening response.

The thermal softening exhibited by the T6 temper using both heating rates (for comparison) can be seen in Figure 57. The T6 temper exhibits a low strain at UTS and extended post UTS elongation at elevated temperatures, with only mild influence of heating rate, as discussed above.

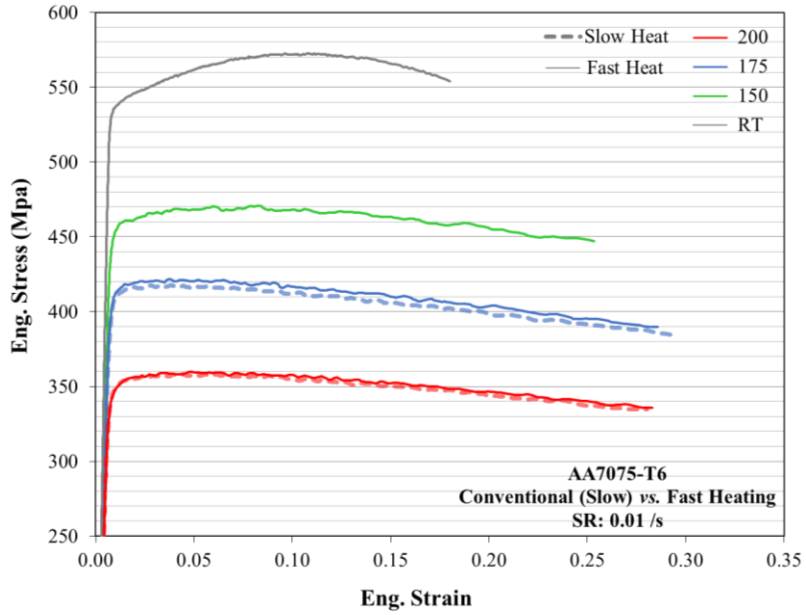

Figure 57. The thermal softening effect observed in the T6 temper, in response to the different heating rates.

Figure 58 serves to compare the thermal softening of all three tempers tested using the fast heating approach. The results are similar to the slow heating tests (Figure 53), with the primary difference being the enhancement of the hardening behaviour of the pre-aged tempers for fast heating to elevated temperatures.

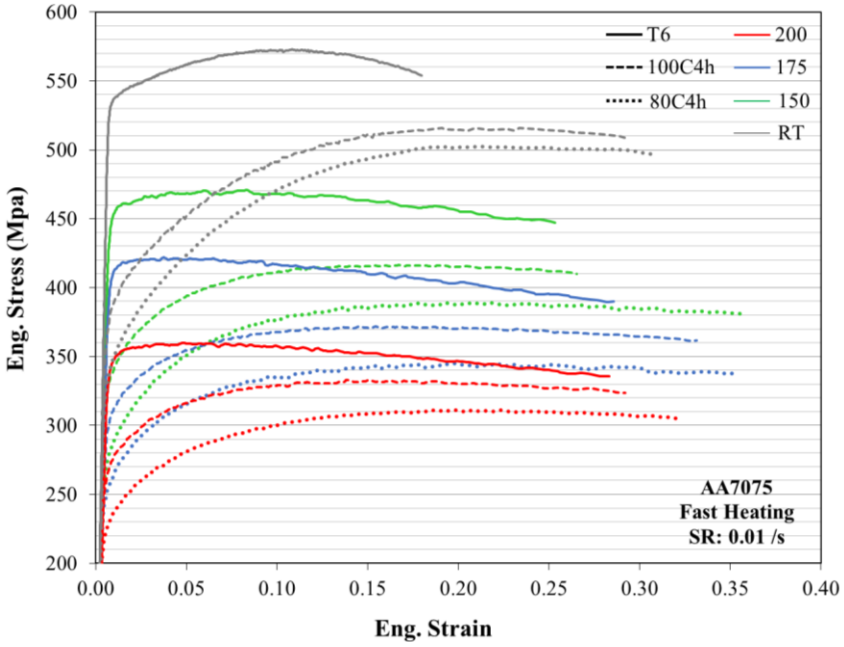

Figure 58. The thermal softening response for all tempers, utilizing the fast heating approach.

Figure 59 serves to examine the effect of strain rate on the true stress versus true strain curves for the three tempers, at different temperatures using fast heating. The T6 temper displays a clear positive strain rate response with an increase in temperature. In contrast, the rate sensitivity is much lower for the under-aged tempers. Of particular note, at room temperature, both the 100C4h and 80C4h conditions exhibit a negative rate sensitivity which is likely due to dynamic strain aging (PLC effect). As temperature increases, the rate sensitivity becomes more positive, but never reaches the rate sensitivity of the T6 condition. As in the slow heating cases, all of the initial temper conditions experience a reduction in total elongation with increased strain rate.

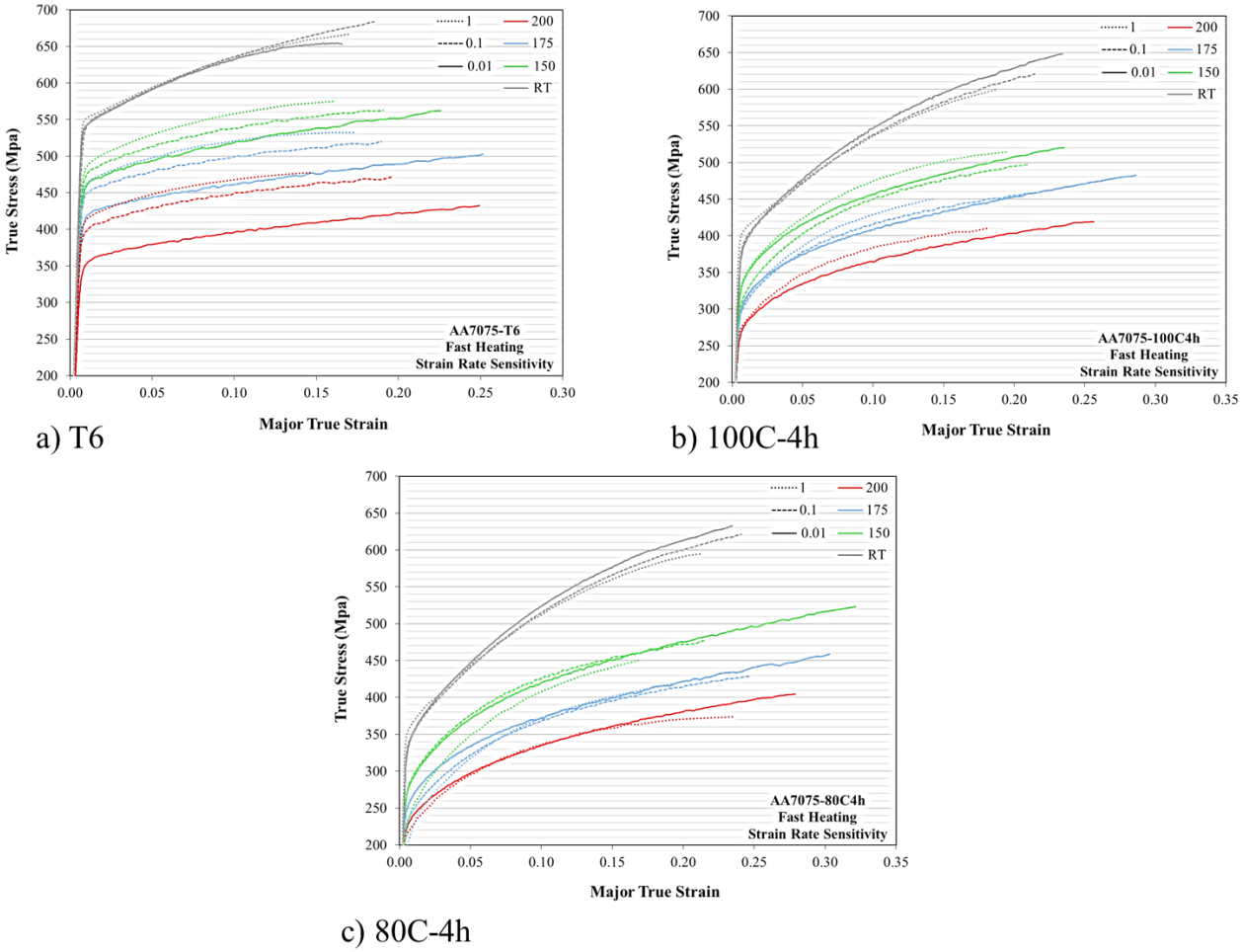

Figure 59. Strain rate sensitivity as observed in the true stress versus true strain curves of the different tempers, using the fast heating rate.

The strain rate sensitivity of the various initial tempers is further examined in Figure 60 which plots true stress values at 10% plastic strain versus strain rate. The T6 temper displays a clear positive SRS, increasing with temperature. The 100C4h and 80C4h tempers show a negative SRS

at room temperature and mildly positive SRS at the elevated temperatures. Despite the more comprehensive test matrix for the fast heating cases, the rate sensitivity trends for fast heating are consistent with those observed for slow heating condition (Figures 54 and 55).

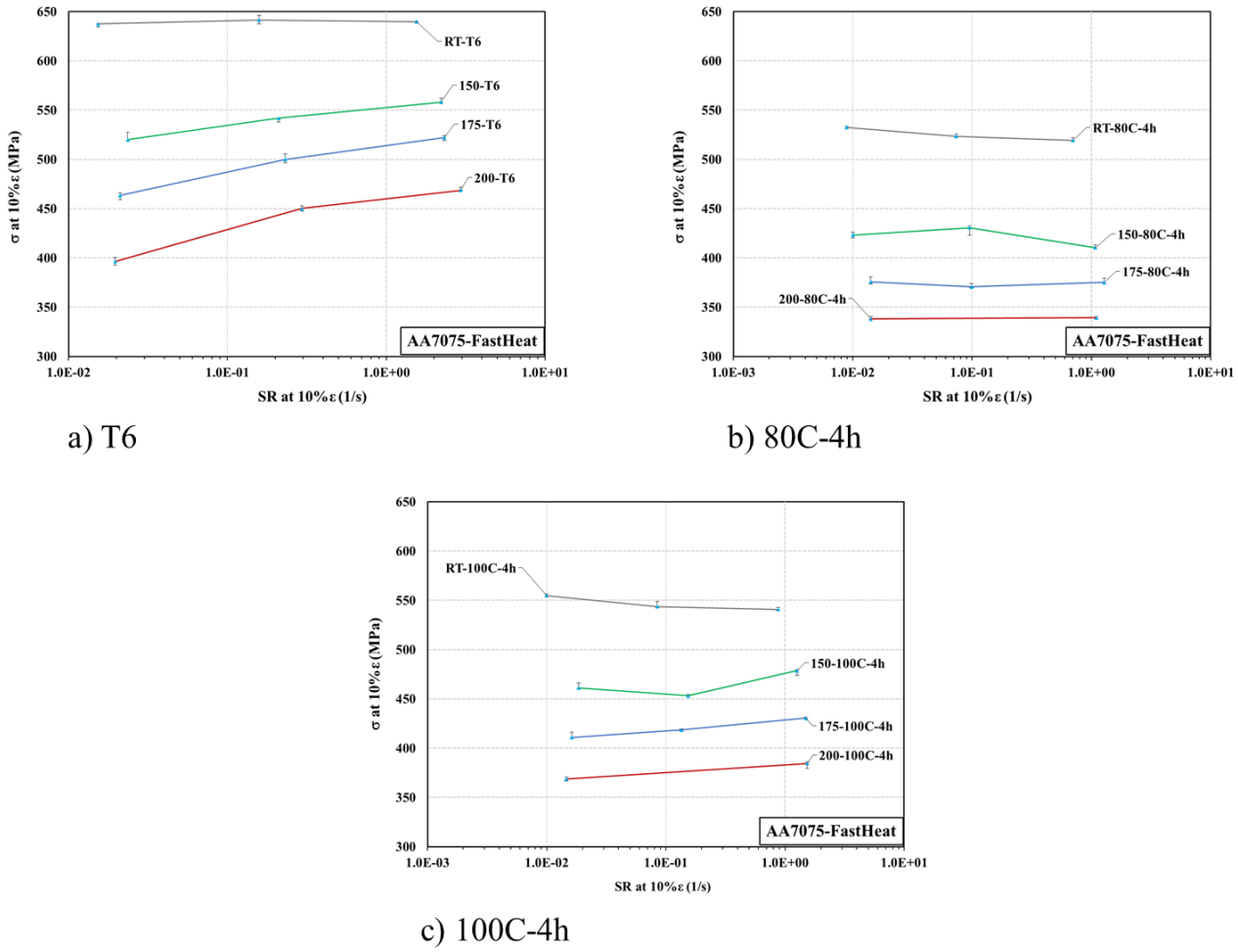

Figure 60. The strain rate sensitivity of the three tempers at the different temperatures, using the fast heating system, characterized in terms of the true stress value at 10% plastic strain versus log strain rate. The error bars represent the maximum deviations from the median results.

In examining the strain rate sensitivity of the under-aged tempers, it is evident that they exhibit a low SRS at elevated temperature and negative SRS at room temperature This behaviour can be attributed to the PLC effects observed for the pre-aged tempers, as examined by Halim *et al.* [52] and Aboulfadl *et al.* [48], which is due to the high solute content at these low levels of precipitation (aging). In contrast, in the peak aged T6 temper, the solute content would be low such that PLC effects are not operative and the SRS is increased. Another interesting aspect of the under aged (80C4h and 100C4h) tempers is that aging is operative during heating of the sample to

the warm testing temperature and during the tensile test itself. The aging during heating was discussed above and accounts for the higher yield strength observed for the slow heated samples (Figure 56). Aging during the test will be higher for the lower strain rate, longer duration tests and could also account to some extent for the lower strain rate sensitivity observed for the under aged tempers (Figure 55 [Right] versus Figure 60 b) and c)). In order to separate the effect of mechanical strain rate sensitivity from the effect of aging during testing, future work should consider strain rate jump tests, similar to that in the work of Kurukuri *et al.* [71].

4.2.1. Constitutive Modeling

As a first step in developing a constitutive fit to the elevated temperature constitutive data, the elevated temperature moduli of elasticity were examined. From the experimental results, there was a drop in the elevated temperature modulus relative to the room temperature value of 71 GPa. However, it was found that the errors associated with calculating the yield strains and stresses using the different moduli of elasticity were less than 4%. Nevertheless, the measured moduli of elasticity were generally utilized for all analysis presented herein (specifically those that deviated noticeably from the room temperature modulus). The details of the modulus calculations are presented in Appendix C.

To evaluate the plastic flow behaviour, a number of models were considered to extrapolate the flow response and to smooth out the inherent noise in the measured data. Figure 61 displays the results of these fits using a number of the common constitutive models for the 100C4h temper, fast heated and tested at 150 °C with a strain rate of 1 s^{-1}. The Hockett-Sherby (H-S) model (as also reported by Rahman *et al.* [57]) was found to be provide the most accurate representation of the flow behaviour up to the UTS point for each temper condition, displaying the highest coefficients of determination (R^2).

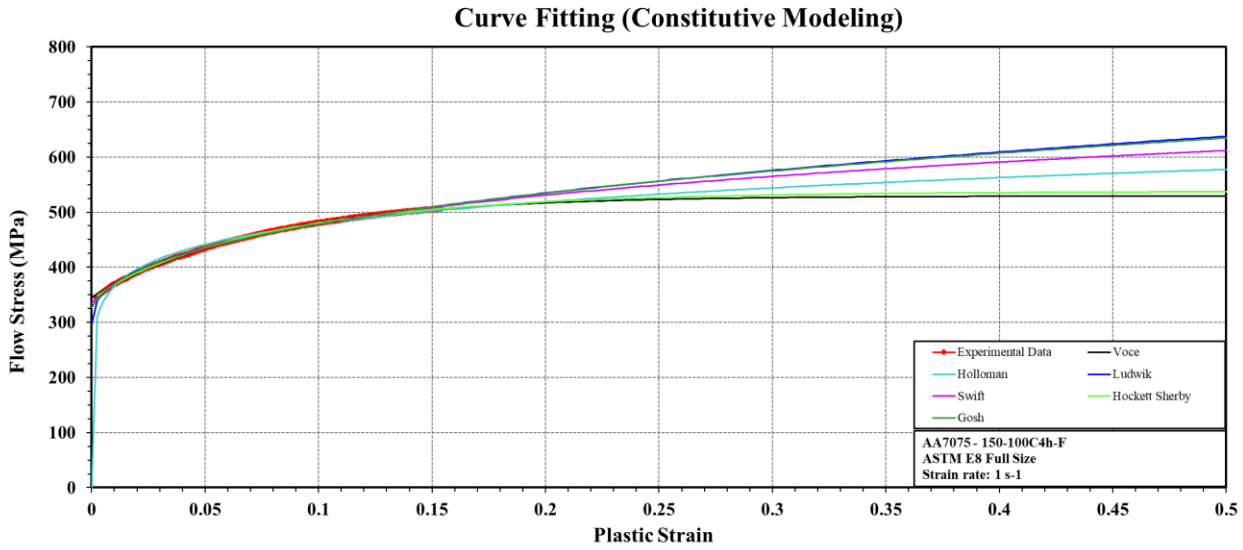

Figure 61. Some common constitutive models fit to the experimental data for the 150C-100C4h-F condition, tested at a strain rate of 1 s^{-1}.

For context, all models displayed a high coefficient of determination, as shown in Table 5, with the minimum R^2 of 89.4% - corresponding to the Holloman fitting model (for the 175-T6-S-0.01 test condition). All other models displayed a minimum R^2 average of 99.7% with a maximum standard deviation of 0.3%. The highest average R^2 coefficient corresponds to the H-S model (99.9%) with a standard deviation of 0.07%.

Table 5. The flow curve fitting model attributes.

R^2\Fitting model	Holloman	Ludwik	Voce	Swift	Hockett Sherby	Gosh	Generalized Voce
Min	0.894	0.993	0.985	0.995	0.997	0.992	0.988
Max	0.995	1.000	1.000	1.000	1.000	1.000	1.000
Average	0.962	0.998	0.997	0.998	0.999	0.998	0.998
STDV.S	0.029	0.002	0.003	0.001	0.001	0.002	0.003

Therefore, given the excellent fit quality of the H-S model, as well as the desirable asymptotic flow response, with saturating stress limits (also observed with the Voce models – see Figure 61), the H-S model (Eq [7]) was selected as the best fitting model for all further studies. Additionally, the H-S model has shown to be of great interest in the industry, given its implementation in a broad range of numerical analysis software including AutoForm.

Figure 62 demonstrates the fitted models pertaining to the flow curves for the 100C-4h temper, warm formed at the elevated temperature of 175 °C, utilizing the Fast Heating approach.

The underlying red curves are the corresponding measured data obtained using the ARM technique (employed for local strain measurements as discussed in Section 3.4.1 and Appendix B.2). In general, the fit quality is judged as reasonable for each case. Table 6 lists the Hockett-Sherby fitting parameters of all test conditions evaluated on the Gleeble apparatus, along with their corresponding coefficients of determination. The fit qualities were high for all fits.

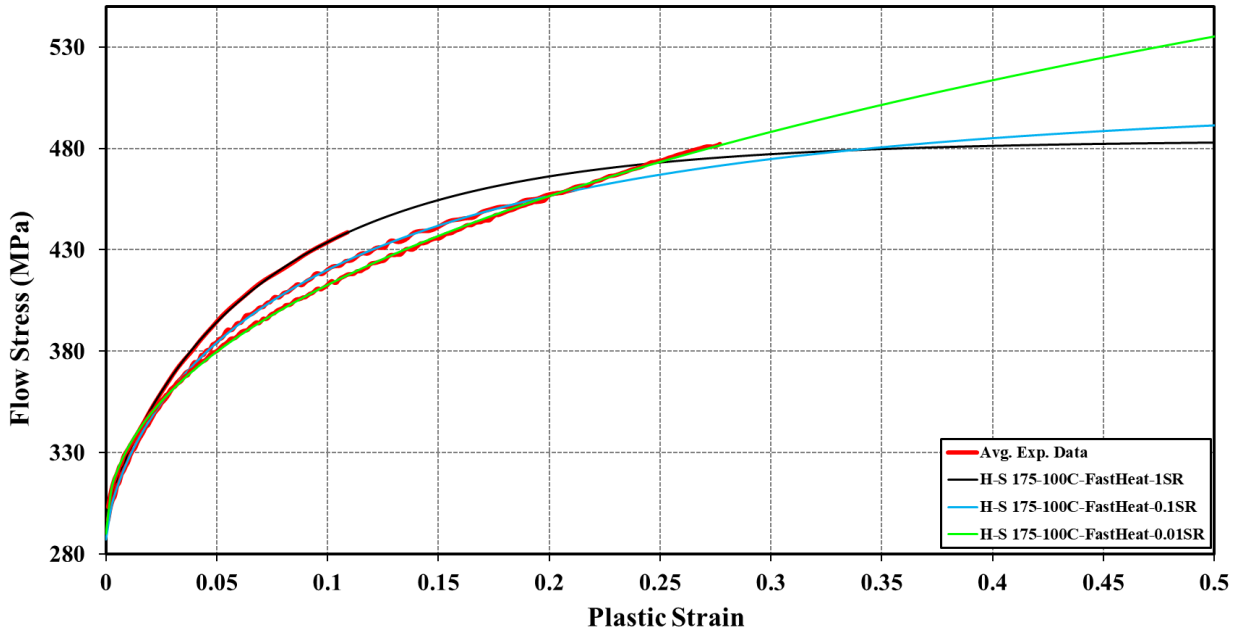

Figure 62. Comparison of the Hockett-Sherby model fits to the measured data (in red) for the 175C-100C4h-F condition tested at the three strain rates of 0.01, 0.1, and 1 s^{-1}.

Table 6. The Hockett-Sherby fitting parameters.

Condition	σ_Y (MPa)	σ_{ss}(MPa)	N	P	R^2
150-80C4h-F-0.01SR	255.53	766.35	1.36	0.53	0.9996
150-80C4h-F-0.1SR	274.19	508.17	6.72	0.78	0.9998
150-80C4h-F-1SR	224.81	520.14	5.84	0.76	0.9999
150-80C4h-S-1SR	242.48	503.26	7.85	0.82	0.9999
150-100C4h-F-0.01SR	316.90	791.48	1.22	0.53	0.9998
150-100C4h-F-0.1SR	303.29	533.95	6.14	0.76	0.9998
150-100C4h-F-1SR	339.70	544.24	8.93	0.89	0.9999
150-T6-F-0.01SR	455.21	1121.57	0.46	0.64	0.9986
150-T6-F-0.1SR	471.72	595.77	5.28	0.80	0.9990
150-T6-F-1SR	487.80	606.00	7.86	0.90	0.9999
150-T6-S-1SR	447.00	1154.94	0.49	0.45	0.9988
175-80C4h-F-0.01SR	232.69	966.03	0.65	0.47	0.9995
175-80C4h-F-0.1SR	223.93	473.12	4.83	0.73	0.9999
175-80C4h-F-1SR	205.92	452.74	7.53	0.80	0.9997
175-80C4h-S-0.01SR	241.81	1161.99	0.50	0.47	0.9993
175-80C4h-S-1SR	210.28	460.67	6.86	0.74	0.9999
175-100C4h-F-0.01SR	290.02	1205.50	0.43	0.48	0.9997
175-100C4h-F-0.1SR	291.22	504.30	4.51	0.68	0.9998
175-100C4h-F-1SR	292.26	484.09	9.05	0.84	0.9999
175-100C4h-S-0.01SR	300.79	1206.37	0.43	0.50	0.9995
175-T6-F-0.01SR	416.31	1165.89	0.32	0.68	0.9982
175-T6-F-0.1SR	445.31	554.45	4.13	0.76	0.9984
175-T6-F-1SR	461.31	552.72	9.12	0.90	0.9995
175-T6-S-0.01SR	413.97	1246.34	0.29	0.71	0.9978
175-T6-S-1SR	412.73	1170.11	0.38	0.38	0.9994
200-80C4h-F-0.01SR	217.13	533.42	2.02	0.62	0.9999
200-80C4h-F-1SR	210.63	394.21	8.16	0.83	0.9996
200-80C4h-S-0.01SR	236.93	588.21	1.36	0.53	0.9999
200-80C4h-S-1SR	215.51	425.46	5.43	0.67	0.9998
200-100C4h-F-0.01SR	253.79	648.63	1.09	0.50	0.9997
200-100C4h-F-1SR	270.13	421.10	11.10	0.88	0.9996
200-100C4h-S-0.01SR	267.34	796.25	0.65	0.47	0.9998
200-T6-F-0.01SR-F	348.45	1080.23	0.28	0.60	0.9974
200-T6-F-0.1SR	389.53	535.69	2.30	0.63	0.9982
200-T6-F-1SR	411.30	491.33	10.33	0.89	0.9999
200-T6-S-0.01SR	350.03	1074.44	0.28	0.63	0.9975
200-T6-S-1SR	342.24	594.43	1.51	0.35	0.9989
RT-80C4h-0.01SR	343.11	709.84	6.15	0.92	0.9999
RT-80C4h-0.1SR	345.68	681.93	7.02	0.96	0.9999
RT-80C4h-1SR	367.38	653.16	8.92	1.05	0.9999
RT-100C4h-0.01SR	385.73	738.09	5.21	0.89	0.9998
RT-100C4h-0.1SR	392.66	687.71	7.05	0.98	0.9998
RT-100C4h-1SR	407.28	665.89	9.00	1.08	1.0000
RT-T6-0.01SR	543.38	671.12	19.94	1.17	0.9995
RT-T6-0.1SR	543.69	747.07	6.34	0.97	0.9999
RT-T6-1SR	552.32	689.95	15.50	1.17	0.9999

Note 1: The flow curves with unrealistically high saturation stresses (σ_{ss} – approaching 1000 MPa) should not be extrapolated, and should only be used for interpolations. Note 2: It is advantageous to include a simulated vs experimental uniform elongation (UE) comparison of the models in this table, for accuracy validations. However, given that the H-S fits were utilized to smoothen the experimental results (utilized to determine the Considère point – Section 4.2.2) this comparison may not be a good indicator of the models' accuracies.

In order to extend the range of useful tensile data beyond the UTS point, Choung *et al.*'s [74] correction factor, Eq [9], was considered. This method corrects for the onset of local necking and the increase of local strain rates at the higher plastic strains, based on the material hardening exponent or *n*-value obtained from a fitted Holloman model. Figure 63 compares the results of Choung's correction method for the three strain rates tests of the 175C-4h100C-F condition, against an ARM correction (constraining) approach proposed by Omer et al. [5] (described in Appendix B.2). The Hockett-Sherby fits for each of the two flow curve correction methods are included in this figure to demonstrate the amplified differences at higher strains.

As illustrated, Choung's approach was most effective when applied to the lower strain rate tests, for which the higher elongations satisfied the minimum thresholds $(\varepsilon_p > 1.4n)$ required in order to apply correction method [74]. At the nominal strain rate of 1 s^{-1}, for this example, the minimum required plastic strain threshold was never met and, therefore, no modifications were made to the flow response.

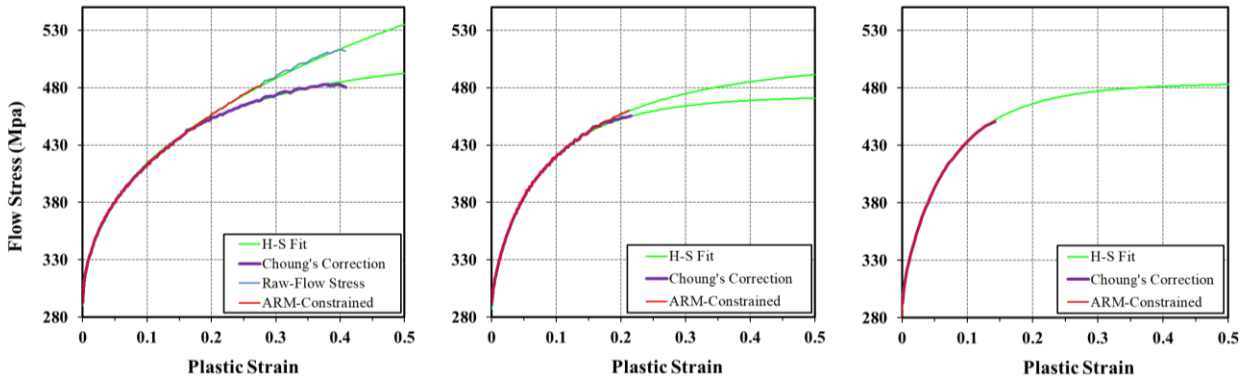

Figure 63. Implementation of Choung et al.'s [74] *ARM correction approach.*

This approach was considered despite our knowledge of the anisotropic behaviour of this alloy (Choung's correction method was developed for isotropic materials), in favour of the flow curve correction advantages. However, as later discussed in Chapter 5.1.1, the implementation of this correction method (in the material models used in numerical simulations) made little difference and was therefore discarded.

4.2.2. Uniform and Total Elongation in the Tensile Tests

The smooth fitted flow curves were used to determine the initiation of diffuse necking as predicted by the Considère criterion. Eq [13] defines the threshold at which uniform elongation is maintained by the work hardening of the material, referred to as the Considère point. Beyond this point, onset of diffuse necking is expected.

$$\frac{d\sigma}{d\varepsilon} > \sigma \qquad OR \rightarrow \qquad \frac{d\sigma}{d\varepsilon} - \sigma > 0 \qquad \text{Eq [13]}$$

Typical curves showing flow stress and work hardening rate (WHR) *versus* plastic strain are plotted in Figure 64 and graphically illustrate the Considère point, which corresponds to their intersection, for a 150C-80C4h-F-0.01 sample condition. This point is indicated by the red diamond symbol, beyond which the flow stress exceeds the WHR and diffuse necking is expected to ensue. Using the fitted H-S models, the right hand equation was utilized to numerically determine the Considère points for all tensile tests performed on the Gleeble apparatus. This equation is also plotted as a function of plastic strain in Figure 65, in which the intersection of the smooth H-S curve with the horizontal axis denotes the Considère point. The raw experimental data is also presented as the faded orange curve, signifying the noise canceling advantages of the fitted models.

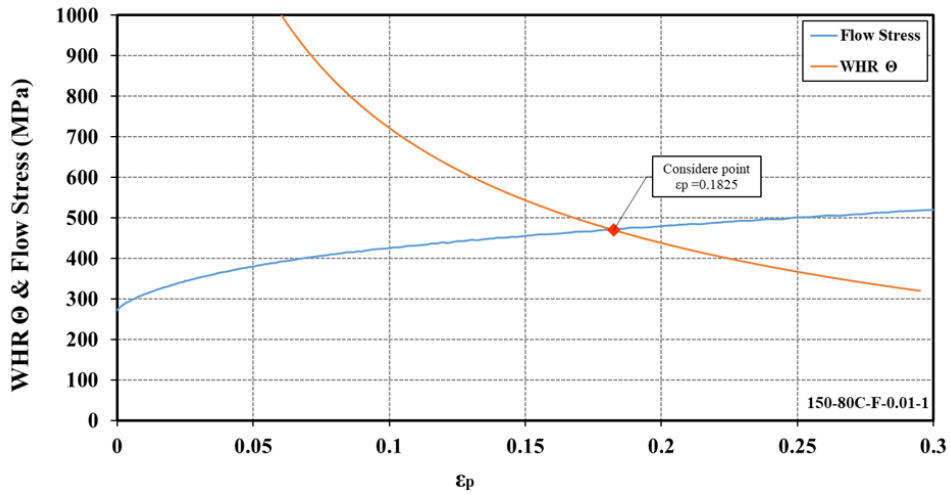

Figure 64. Graphical demonstration of the Considère point, at the location where the flow stress and the instantaneous WRH intersect. The 150-80C4h-F condition tested at a strain rate of 0.01 s^{-1} was used here, for demonstration purposes.

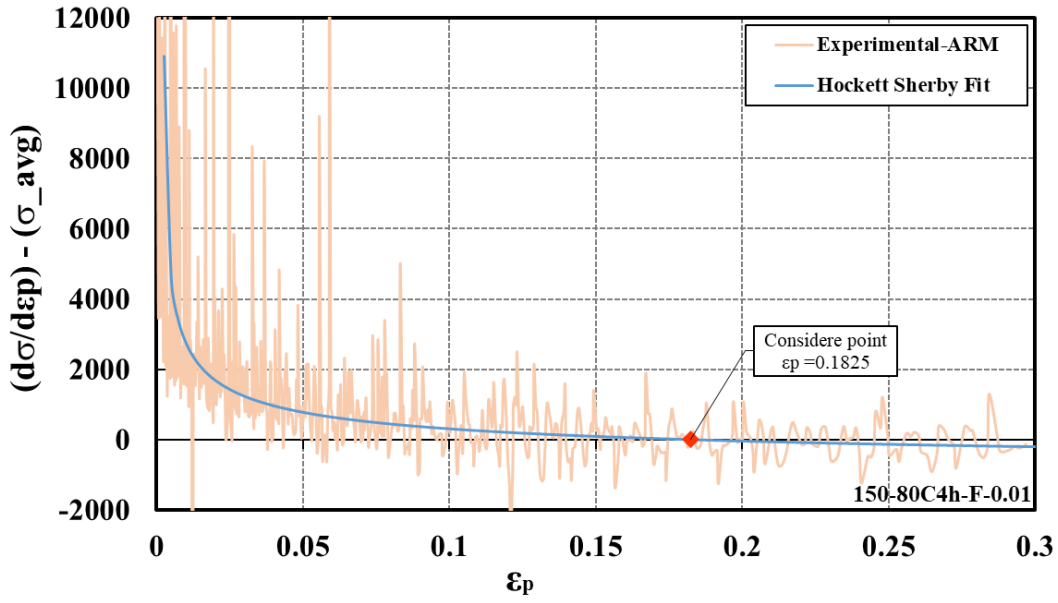

Figure 65. A visual demonstration of the Considère point evaluation with the vertical axis set to the right hand equation (Eq [13]) and the horizontal axis defining the plastic strain. The faded orange curve represents the noisy experimental data and is included for comparison purposes. The 150-80C4h-F condition tested at a strain rate of 0.01 s^{-1} was used here, for demonstration purposes.

The total elongation up to the point of local necking or fracture (obtained using the ARM technique) for each of the evaluated conditions, is compared in the bar chart in Figure 66. Also plotted is the limit of diffuse necking, shown as symbols. The maximum and typical standard deviations for the Considère points for the conditions listed in this chart were ± 1% and ± 0.5%, respectively. The maximum deviations correspond to the 200-100C4h-F-1SR temper. Note that although the obtained data exhibit a significant amount of noise, the fitted data were quite smooth and repeatable, and were utilized when determining the standard deviations. Further, the standard deviations in the measured elongations were generally larger with maximum and typical values of nearly ± 3% and ± 0.75%. The 175-T6-F-0.01SR condition defined the upper threshold in deviation in elongation. The room temperature tests performed on this apparatus displayed quite low deviations in the total elongation results, with a typical standard deviation of ± 0.4%.

In Figure 66, an increase in uniform elongation is generally observed for the lower pre-aging states. Interestingly, while an increase in forming temperature normally improves the total elongation, the uniform elongations are shown to be reduced as temperature increases. This effect

is observed for all three tempers. Further, the elongations are reduced at higher strain rates, as previously discussed.

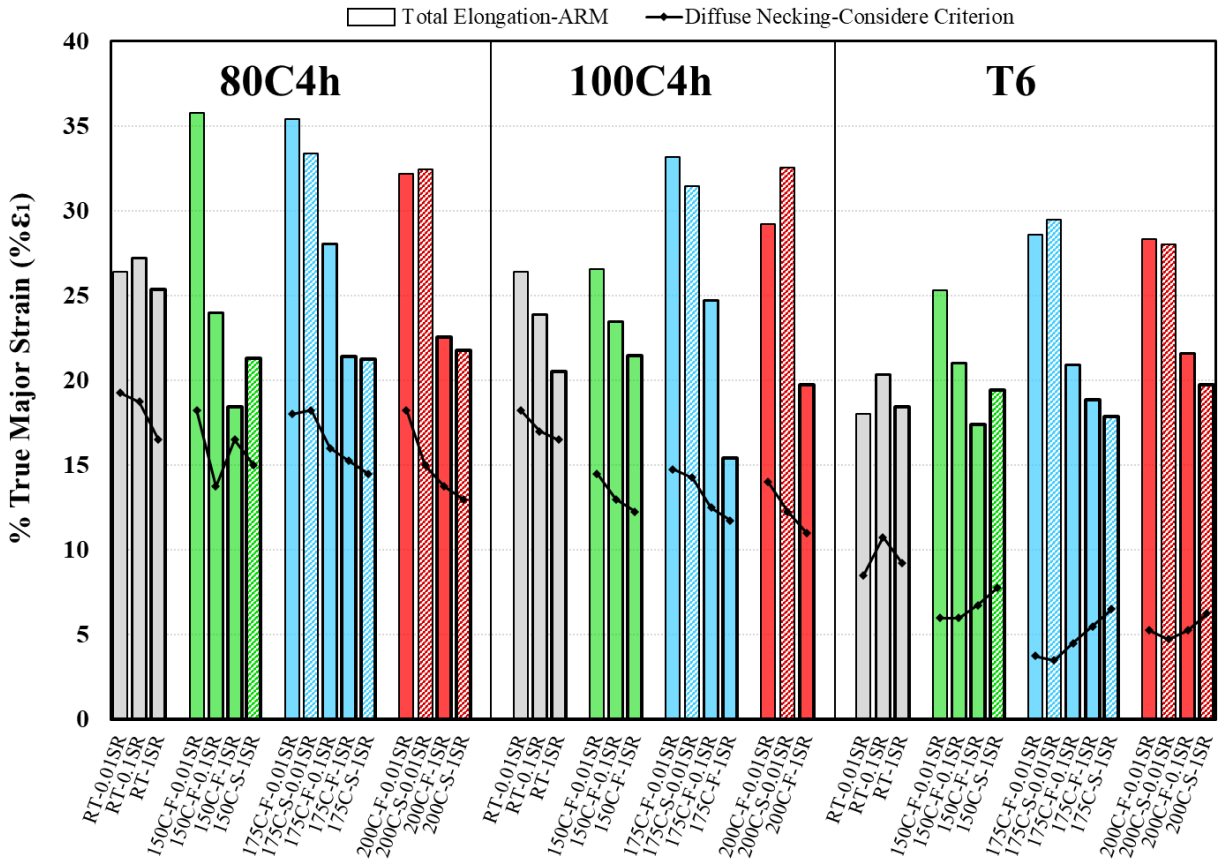

Figure 66. Comparison of the Considère point (uniform elongation, plotted as connected diamond symbols) and the total elongation (plotted as bars) for the various test conditions. Each value corresponds to the median result for the respective test condition. Variability is discussed in the text.

4.2.3. Selection of Initial Tempers for Warm Forming Experiments

The down-selection of the test conditions for the warm formability experiments was undertaken using the obtained constitutive data. Up until this point, given the different process routes that the AA7075 alloy has been exposed to, the following general behaviours have been observed:

- Thermal softening enhances total elongation, but reduces uniform elongation.
- Strain rate sensitivities (SRS) of the three selected tempers:

    - T6 has shown a positive SRS, with a strong positive correlation with temperature.
    - 100C4h has shown a negative SRS at room temperature, and a positive SRS at the elevated temperatures.
    - 80C4h has exhibited a low to negative SRS at all temperatures.
- PLC effects have been observed with the pre-aged tempers, influencing the repeatability of the results.
- A coupled effect between SRS and aging is at play and evident in the pre-aged tempers in which aging during testing (and specimen heating) leads to increased strength for the lower strain rate experiments – this phenomenon is also expected to take place during the warm forming experiments.
- Through the use of the fast heating approach, some unintended aging can be avoided.

Considering these effects, the down-selection of process routes was conducted through the use of some quantitative measures, complimented by graphical comparisons. Further, to determine the desired test conditions, the potential to achieve higher formability limits and superior stability (*i.e.* lower PLC effect) were held as important objectives. In addition, forming at lower temperatures with the lower yield strengths (whether caused by thermal softening or pre-aging) presents a more energy efficient approach to forming, and was therefore taken into consideration in the selection process.

Detailed calculation and ranking of these performance measures is given in Appendix D, for brevity. Based on this ranking (Table 10), a number of processing routes were selected for consideration in Stage 3 of the test matrix which comprises the warm forming characterization experiments. These conditions are highlighted in a re-plot of the Gleeble test matrix, shown in Figure 67. In general, the T6 condition was considered in light of its strong positive strain rate sensitivity and good increase in elongation at elevated temperatures. Both under-aged tempers were considered due to their strong hardening rates and high elongations. Experiments considering both slow and fast heating were included in the warm forming test matrix. Finally, the effect of punch speed (strain rate) was considered in view of the strong effect it exerts on tensile elongation.

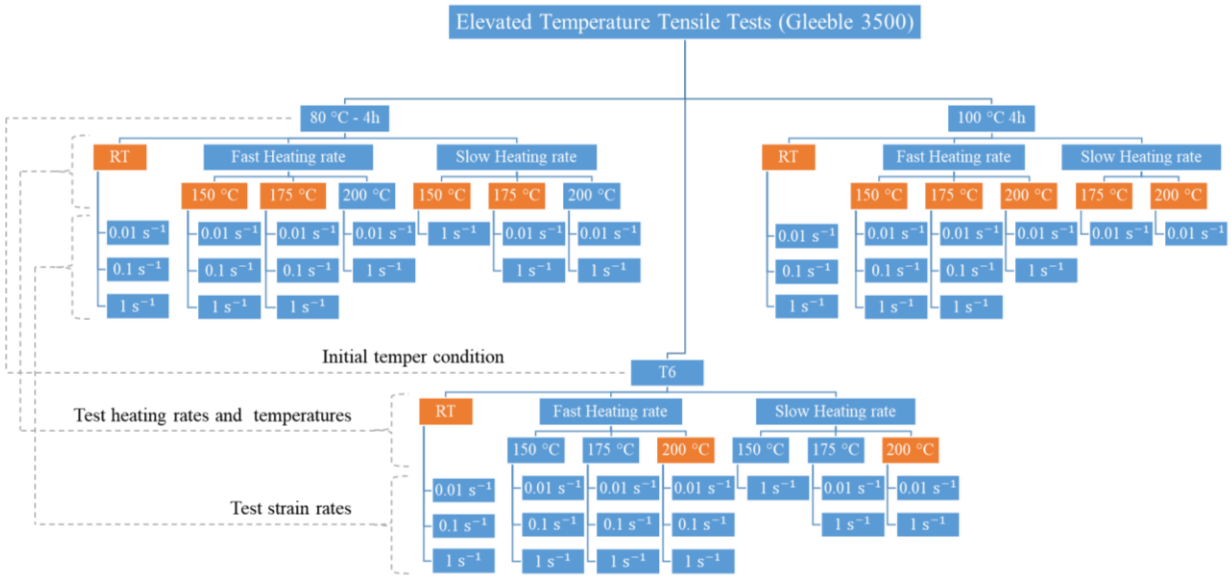

Figure 67. The selected Gleeble tensile testing process routes, down-selected for warm formability characterization.

4.3. Stage 3 – Warm Formability Characterization

The complete set of formability results are plotted on a forming limit diagram in Figure 68, from which the general enhancement in limit strains due to elevated temperature forming can be observed. Similar to the results of the preliminary room temperature tests (Chapter 4.1.2), the minor strain limits are slightly positive. The repeatability for both the major and minor strain is within ± 0.037, which is slightly higher than that observed for the room temperature formability tests, but is once again considered acceptable. A notable condition with a low scatter in forming limits tested at different stroke rates is the 100C4h temper, heated using the platen furnace (fast heat) and warm formed at the temperature of 175 °C (bolded blue borders).

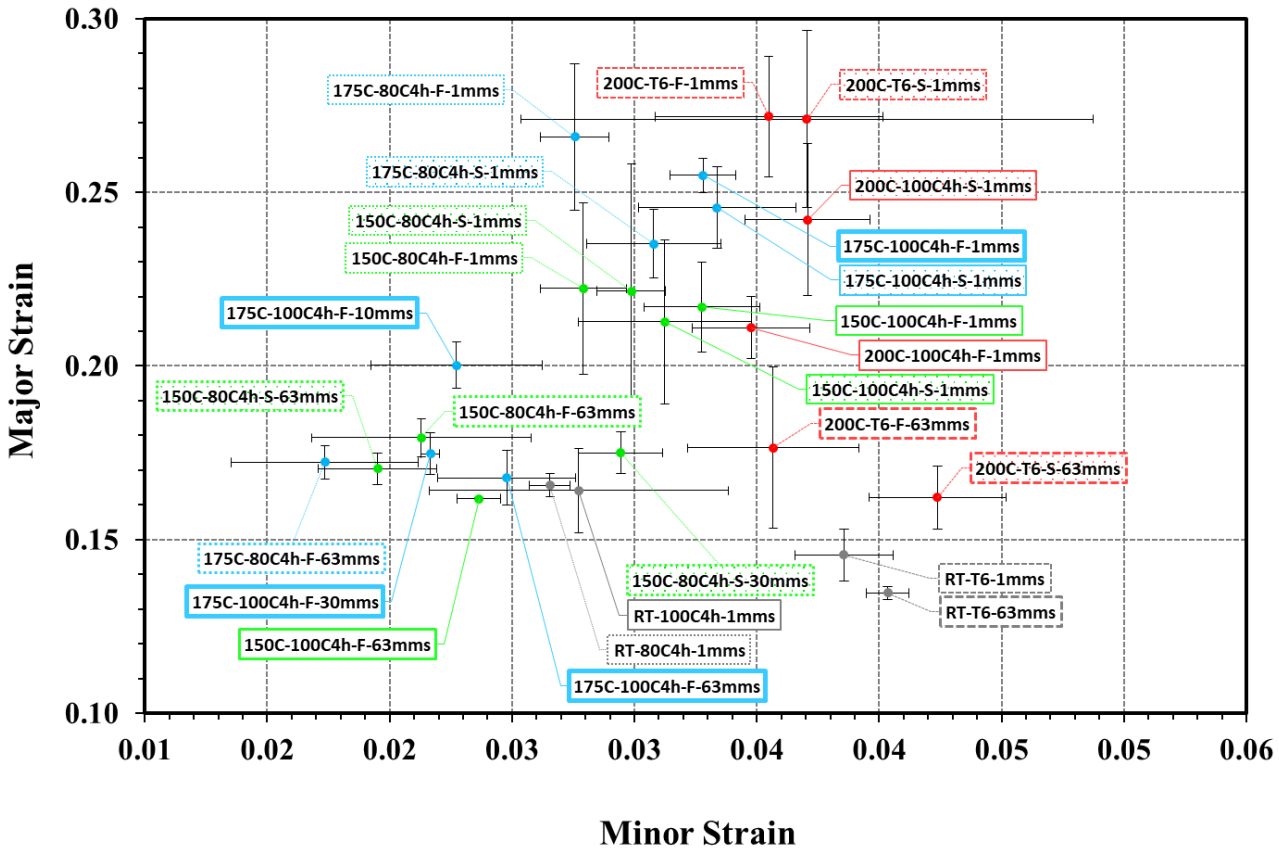

Figure *68. The measured limit major and minor strains from the warm forming experiments shown on a forming limit diagram plot. The error bars represent the standard deviations.*

The forming limits of the slower forming speed tests (1 mm/s), as defined by major limit strains (determined using the ISO12004-2:2008 standards) and the corresponding dome heights, are plotted as a function of forming temperature for the three tempers in Figure 69. A clear increase in the limit strains with temperature is observed in the left hand graph for all tempers. The T6 temper (grey symbols) shows significant improvements, achieving the highest major strains at the warm forming temperature of 200 °C. Furthermore, the fast heating process routes tend to display better forming response as compared to their corresponding slow heating routes.

It was previously shown (Appendix D) that the conditions exhibiting a high extent of work hardening, and an increasing instantaneous strain hardening exponent displayed high total elongation. This response is also confirmed here, as the conditions meeting both criteria have in fact resulted in high forming limit strains.

The limiting dome height data Figure 69 [Right], identified by the visible load-drops in the load-displacement plots, provides an alternative measure of formability. Interestingly, the T6 temper (which had shown the largest increase in formability limits in response to increased temperature) displays only a mild increase in dome height with forming temperature. Here, it can be deduced that the high strain levels of the T6 tempers were not uniformly distributed across the Nakazima plane strain dome geometry. This effect is consistent with the early onset of diffuse necking observed in the engineering stress-strain curves of the T6 temper (described in Chapter 4.2) and the elongation comparison chart in Figure 66.

In contrast to the T6 behaviour, the pre-aged tempers display an increase in dome height with forming temperature, with the fast heating routes, again, displaying superior limits. At forming temperatures of 150 and 175 °C, the pre-aged tempers exhibit a peak in forming limits as observed in both the limit strain data and the limit dome height results. Further, the 80C-4h temper shows the highest limit strains of the two pre-aged tempers, and the largest limiting dome heights across all tempers.

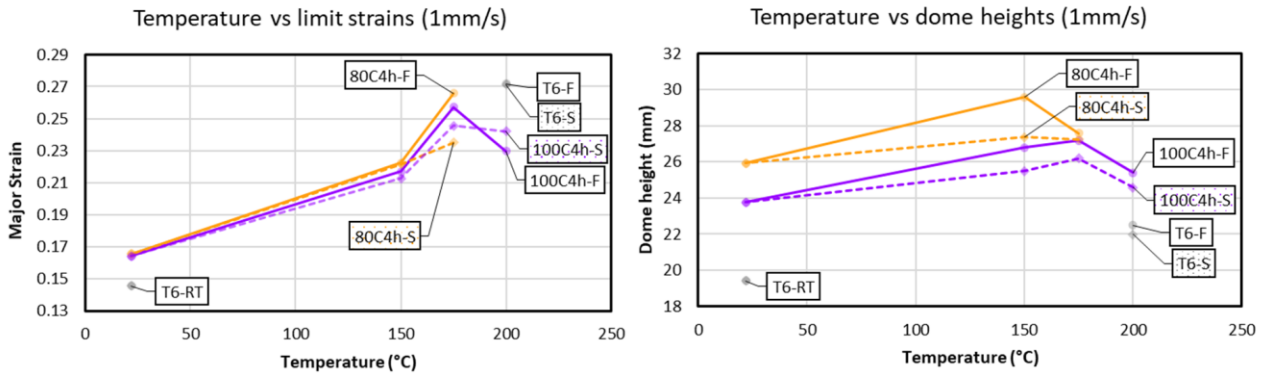

Figure 69. [Left] The major limit strains from the slow (1 mm/s) punch stroke tests. [Right] The maximum dome heights of the slow (1 mm/s) punch stroke tests. Initial tempers and heating rates (F-fast, S-slow) are indicated.

Figure 70 displays the limit strains and maximum dome heights for the three tempers as a function of forming speed. The faster stroke rate tests resulted in lower forming limits which is consistent with the effect of strain rate on elongation observed in the engineering stress-strain data.

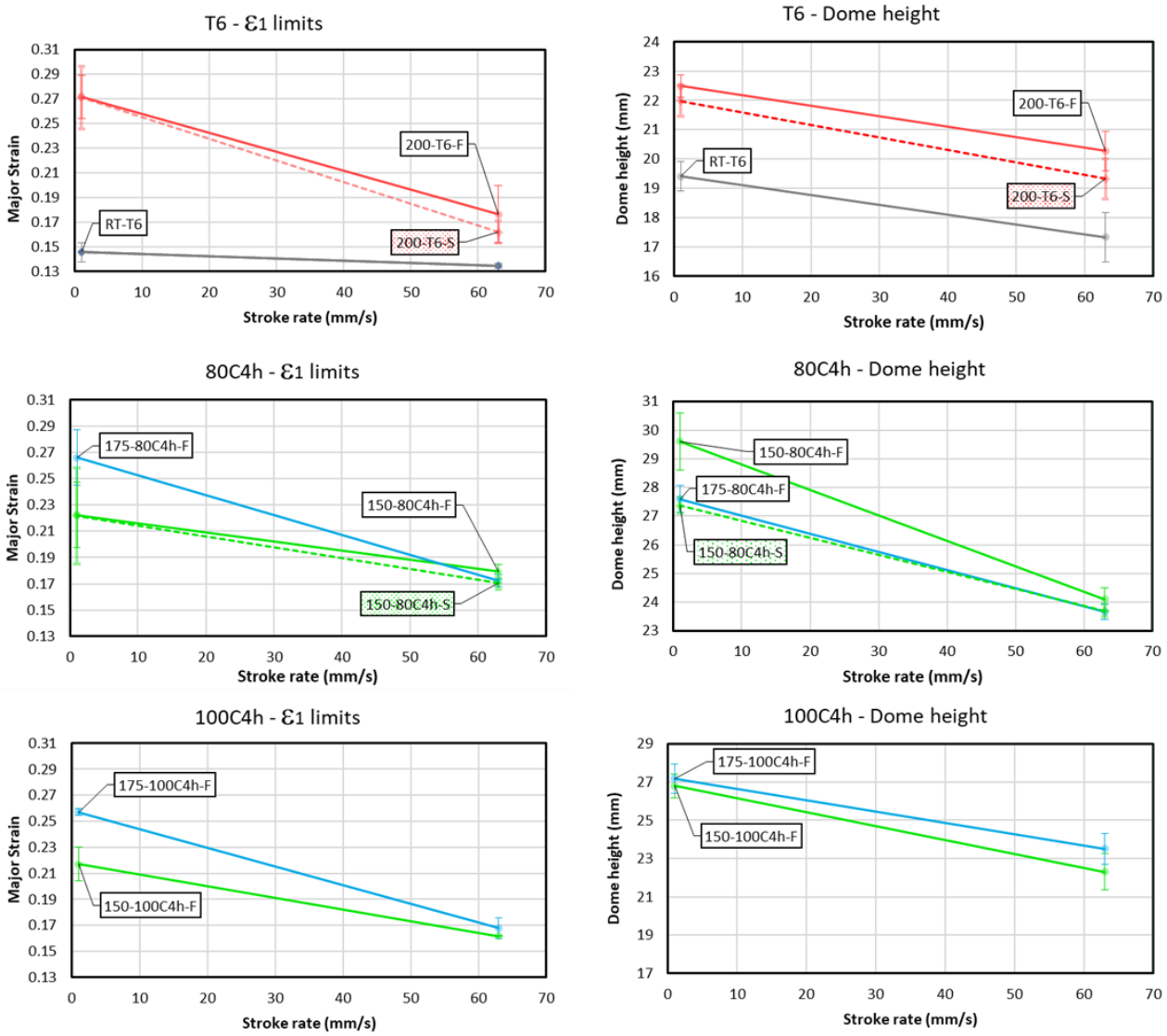

Figure 70. The major limit strains [Left hand graphs] and maximum dome heights [Right hand graphs] of the three tempers tested at different forming temperatures and heating rates vs. forming speed.

Figure 71 provides a summary of the measured limit strains and dome heights for all of the warm forming trials. It is evident that the pre-aged conditions benefit from the higher extent of work hardening imparted by the lower extent of aging (yield strength) prior to forming, as compared to the T6 temper. With higher test temperatures, the limit strains have generally shown a positive increase. This response is also reflected in the dome heights.

The quantitative formability limit improvements observed with the slower (1 mm/s) test results of the175-80C4h-F and 175-100C4h-F conditions with respect to the reference T6-RT condition is approximately 83 and 77 % in terms of major limit strains and 42 and 40 % in terms

of dome heights, respectively. The faster rate tests (63 mm/s) displayed improvements of 28 and 25 % with respect to strains and 37 and 36 % with respect to dome heights. Furthermore, the 150C-80C4h-F condition has shown the highest increase in dome heights, compared to the RT-T6 condition, corresponding to 53 % for the 1 mm/s tests and 39 % for the 63 mm/s tests (which correspond to major strain increases of 53 and 33 %, respectively.

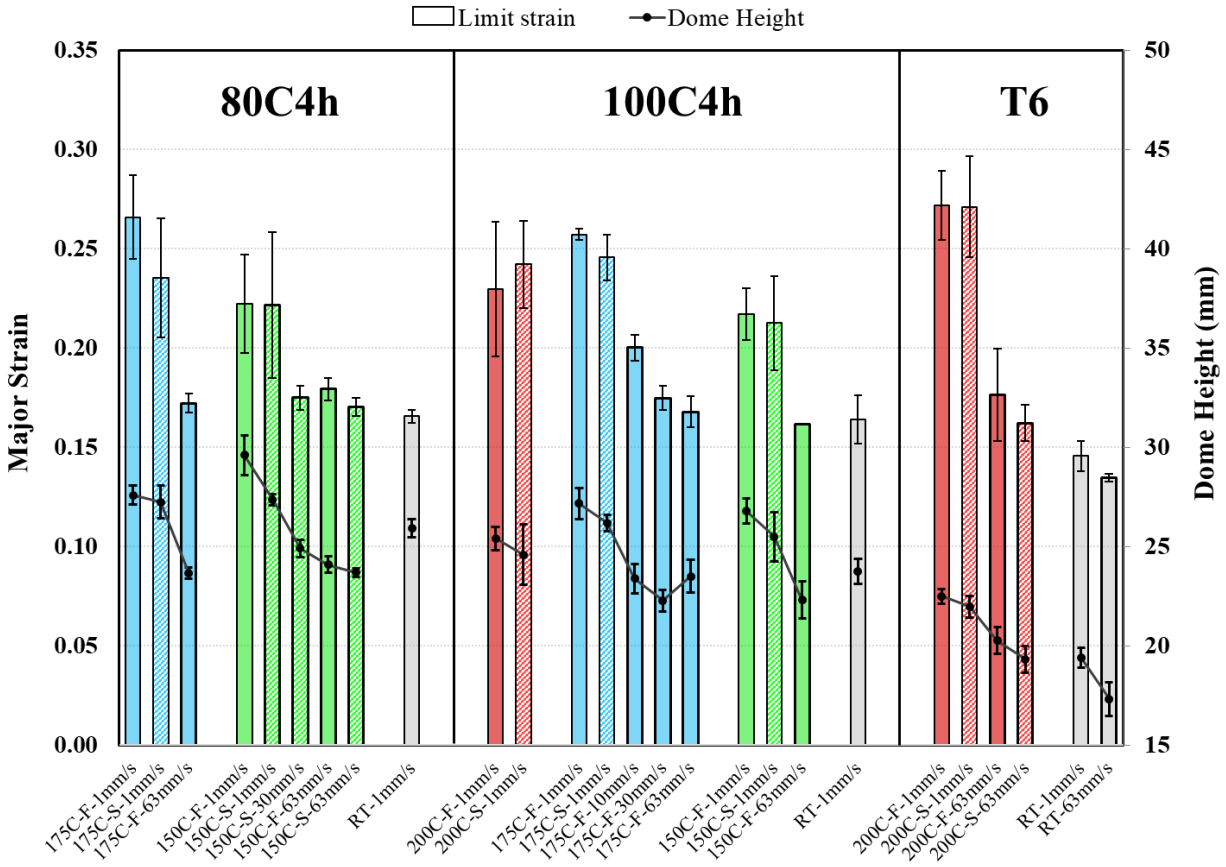

Figure 71. Limiting major strains and dome heights for all of the warm forming test conditions. The error bars represent the standard deviations.

A selection of the most favourable under-aged (PA) conditions from the warm forming trials, along with the T6 tempers (included as a reference) were selected to examine the final hardness of the formed parts following a paint bake cycle (PBC). The specimens tested at the higher stroke rate of 63 mm/s were considered for this study, since this forming speed is closer to that used in industrial forming operations. The conditions selected for paint bake thermal processing are highlighted in the re-plot of the warm forming test matrix in Figure 72.

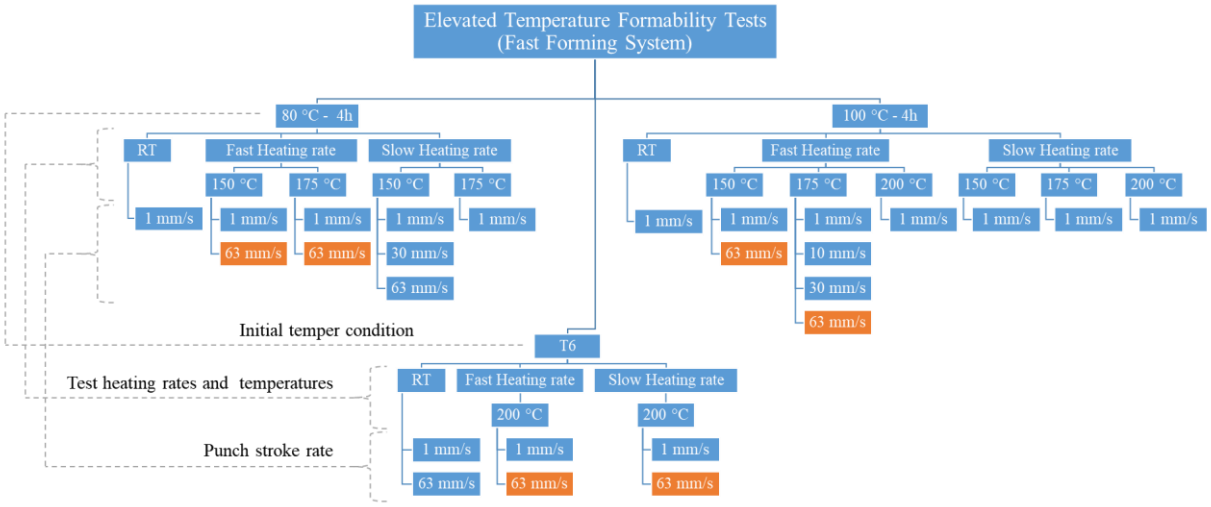

Figure 72. The selected warm forming conditions considered to evaluate hardness following PBC.

4.4. Stage 4 – Final Hardness Following PBC

The selected warm formed specimens were utilised to examine the final hardness following paint bake cycling. Hardness measurements were taken from formed parts, both within regions deformed to approximately 10% strain, as well as from flange regions that experienced the same thermal treatments, but with no deformation. Hardness values were also measured for the same regions following paint bake cycling, thus representing the final properties of the material that are to be expected within a warm formed and paint baked automotive part. The test matrix in Figure 73 displays the conditions that were selected from the warm forming experiments, to be evaluated in this study. All micro-hardness measurements were evaluated on the through-thickness (cross-sectional) plane of the specimens.

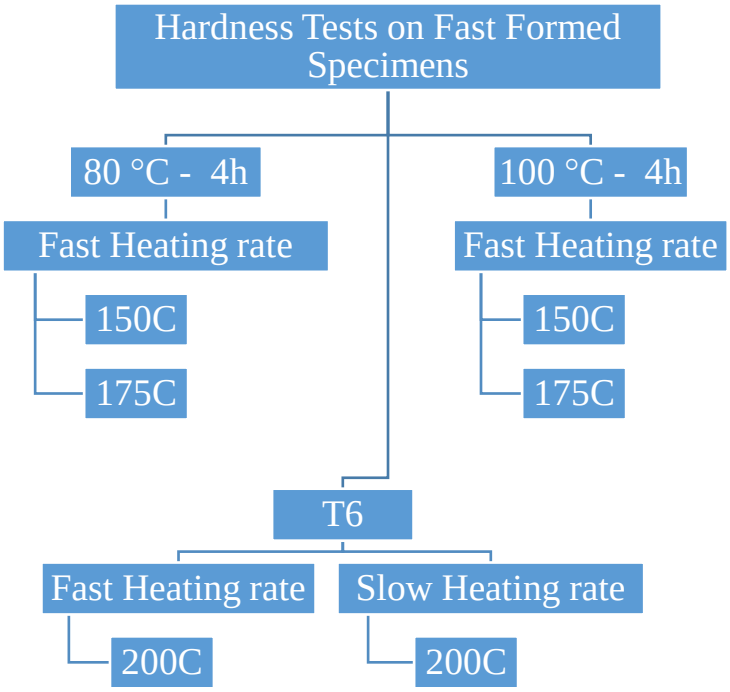

Figure 73. The final hardness test matrix, highlighting the selected forming process routes.

The hardness results are presented in Figure 74. An interesting effect is observed for the T6 tempers, in which some characteristics of retrogression and re-aging, as evaluated by Karaaslan *et al.* [113], are observed. The hardness values following the warm forming process are reduced, below that of the initial T6 temper. However, the heat treatment involved in the PBC appears to return the hardness values to those of the T6 peak aged temper. This effect is observed for both heating rate process routes, for the formed and flange regions.

Also interesting are the hardness results from the 175C-100C4h-F process route, which exhibited a considerable hardness increase in response to the PBC. The corresponding average hardness value achieved from this forming route is approximately 97% of that of the peak T6 temper.

Moreover, Deschamps *et al.* [44] have reported a dislocation annihilation effect observed during deformation of age-hardenable Al-Zn-Mg alloys. This effect seems to be present in the 150-80C4h-F-63 hardness results, apparent from the reduced hardness values of the warm formed state compared to the initial temper's hardness readings. However, given the heat treatment involved in

the PBC, these conditions subsequently gained a large increase in hardness values, likely, due to a similar retrogression and re-aging effect, observed for the T6 temper.

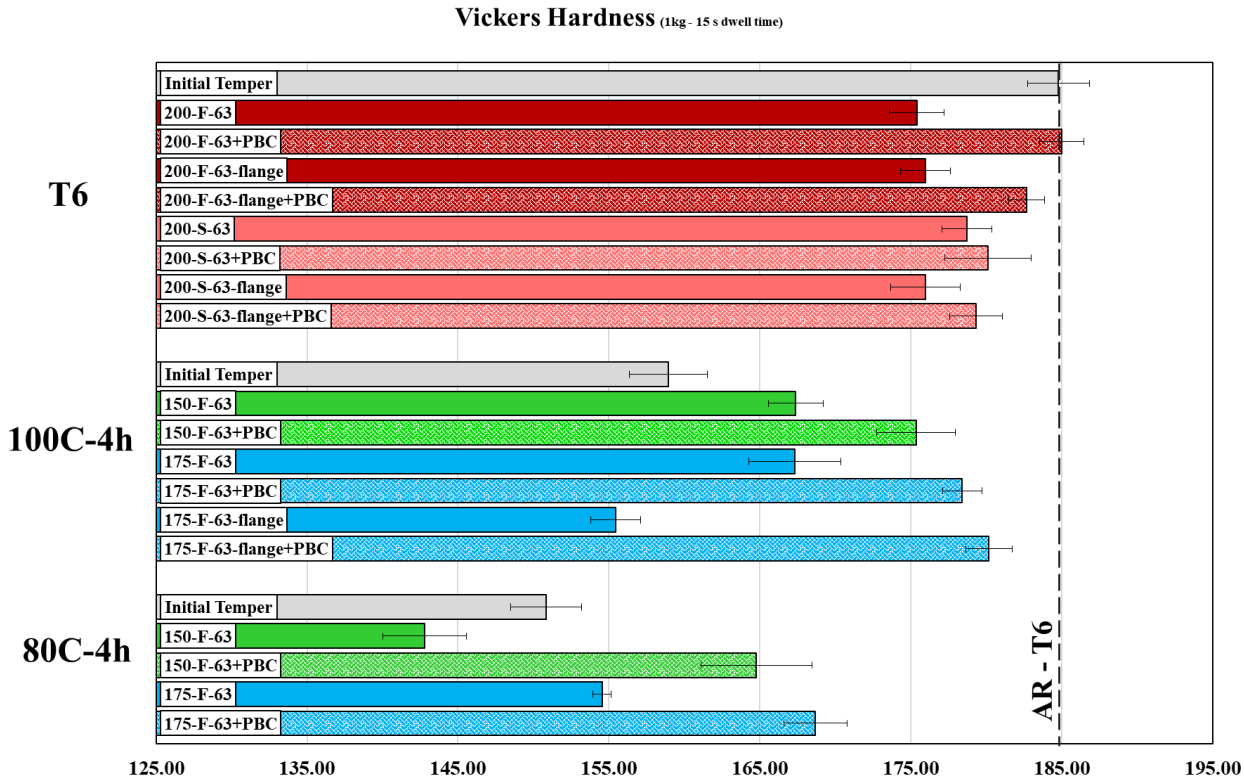

Figure 74. Hardness measurements of the as formed (10% strain) and flange regions of the top performing test conditions. The error bars represent the standard deviations.

Considering the excellent response of the 175-100C4h-F process route to the PBC, this condition has been shown to satisfy all of the selection criteria set in this thesis (discussed in Section 4.2.3). The high levels of formability (and good repeatability), the high precipitation hardening potential, and the relatively low initial yield strength favour the use of this condition in warm forming processes. Moreover, the warm forming temperature for this route is also relatively low compared to the optimal temperatures for the T6 condition [29], and other high-strength aluminum alloys of the 6000-series designation [82], [83].

5. Numerical Modelling – Constitutive Model Assessment

A series of thermo-mechanical numerical simulations of the tensile and the plane strain Nakazima tests were undertaken in order to validate the constitutive fits developed in Section 4.2.1. The simulations were performed using the LS-DYNA (R12.0.0) finite element software. The static implicit and dynamic explicit formulations were adopted for the plane strain formability and tensile tests, respectively. The tensile test validations are presented first, followed by the Nakazima model results.

5.1. Tensile numerical analysis

A numerical study of the Gleeble experiments (Figure 36) was conducted to evaluate the accuracy of the constitutive models. This numerical study utilized a single component tensile geometry, as shown in Figure 75, comprised of quadrilateral elements. An element size of 0.3 mm was used in the gauge region of this geometry. Five integration points through the 2 mm thick specimen were evaluated with a fully integrated in-plane shell element formulation (ELFORM = 16). A fixed boundary condition was assigned to the left hand nodes of the simplified geometry shown in Figure 75. The nodes at the right hand of the specimen were pulled at constant speeds of 0.29, 2.9, and 29 mm/s, corresponding to the cross-head speeds of the Gleeble apparatus for nominal strain rates of 0.01, 0.1, and 1 s^{-1}, respectively. Lastly, the specimens were treated as isothermal (constant temperature) and the test temperature associated with each test (150, 175 or 200 °C) was assigned to all elements in the model.

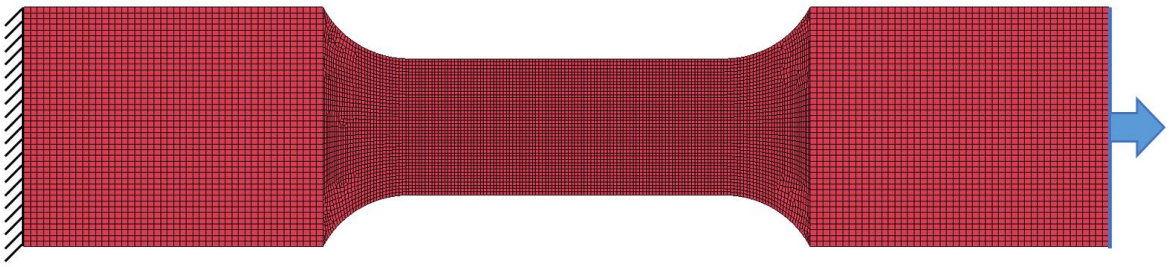

Figure 75. The meshed Gleeble geometry, utilized for the tensile numerical analysis.

5.1.1. Material Model

The material work hardening response was modelled using the fitted Hockett-Sherby flow curves (Section 4.2.1) which provided a smoothed and extrapolated hardening behaviour for each test condition. The fitted parameters are given in Table 6. Further, the Barlat YLD2000 yield surface, calibrated by Rahmaan *et al.* [58], was used to characterize the anisotropic yield surface. No fracture/failure criteria were employed to simulate the tensile tests.

A 3D table containing the point-wise discretized Hockett-Sherby curves for the different strain rates at the different forming temperatures were input into the MAT_133 (MAT_BARLAT_YLD2000) material card. Each temper and heating rate was treated as a different material and was, therefore, assigned a dedicated material card. Figures 76, 77 and 78 display the input constitutive dataset for each of the three tempers (T6, 100C4h, and 80C4h, respectively) at the two heating rates. The flow curves in this figure defined the elastic moduli and plastic behaviour for each strain rate and temperature condition. Moreover, interpolation between strain rate data was performed when possible (curves marked by the asterisks).

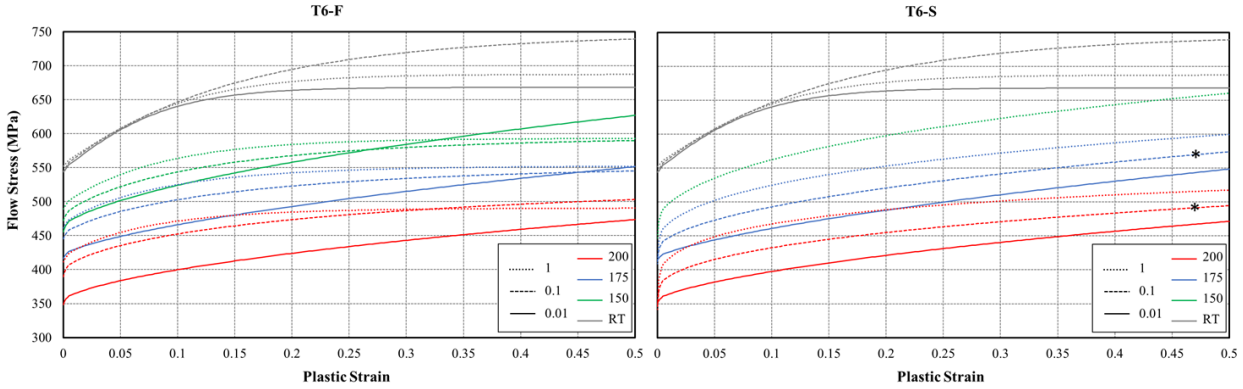

Figure 76. Flow curve data-set input to the material card, corresponding to the T6 temper, [Left] fast heating condition, [Right] slow heating condition. The flow curves denoted by the asterisk are interpolations between the strain rate dataset.

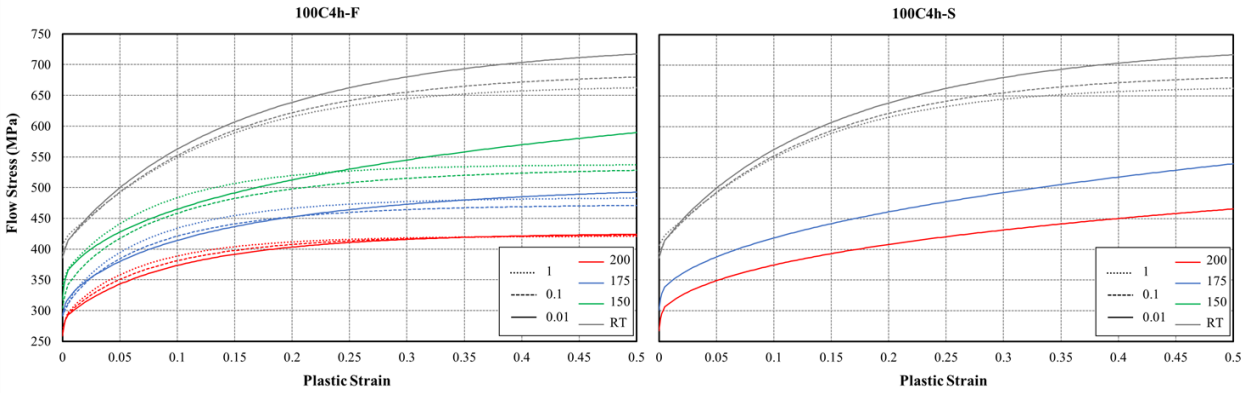

Figure 77. Flow curve data-set input to the material card, corresponding to the 100C4h temper, [Left] fast heating condition, [Right] slow heating condition.

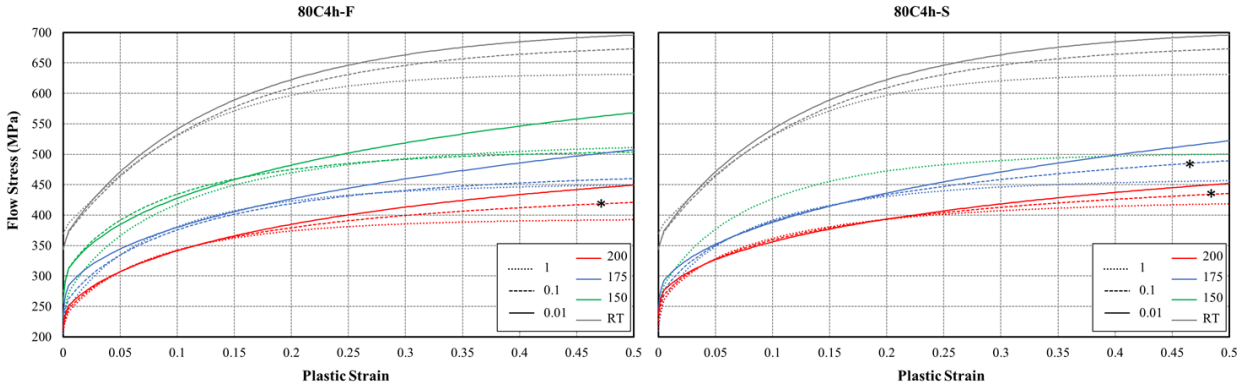

Figure 78. Flow curve data-set input to the material card, corresponding to the 100C4h temper, [Left] fast heating condition, [Right] slow heating condition. The flow curves denoted by the asterisk are interpolations between the strain rate dataset.

As examined by Leacock *et al.* [104], the precipitation process during aging is not expected to exert significant influence on the anisotropy of this alloy (also described in Chapter 3.1). In this study, R-values (acquired in the rolling direction) were obtained using the local strains from the ARM strain data, over a typical range of through-thickness strain of approximately 2 - 6 %. This range corresponds to the region with linear correlation between the width and thickness strains (prior to the onset of diffuse necking). A graphical summary of the R-values is presented in Figure 79. As can be seen, the R-values range from approximately 0.5 to 0.58, which are lower than the r-values of 0.78 reported by Rahmaan *et al.* [57] for this alloy. This difference may be due to the different r-value evaluation range of 0 – 6 % plastic strain. Nevertheless, given the more comprehensive study on the r-values (in multiple directions) conducted by Rahmaan *et al.* [57], their findings were utilized in this numerical study.

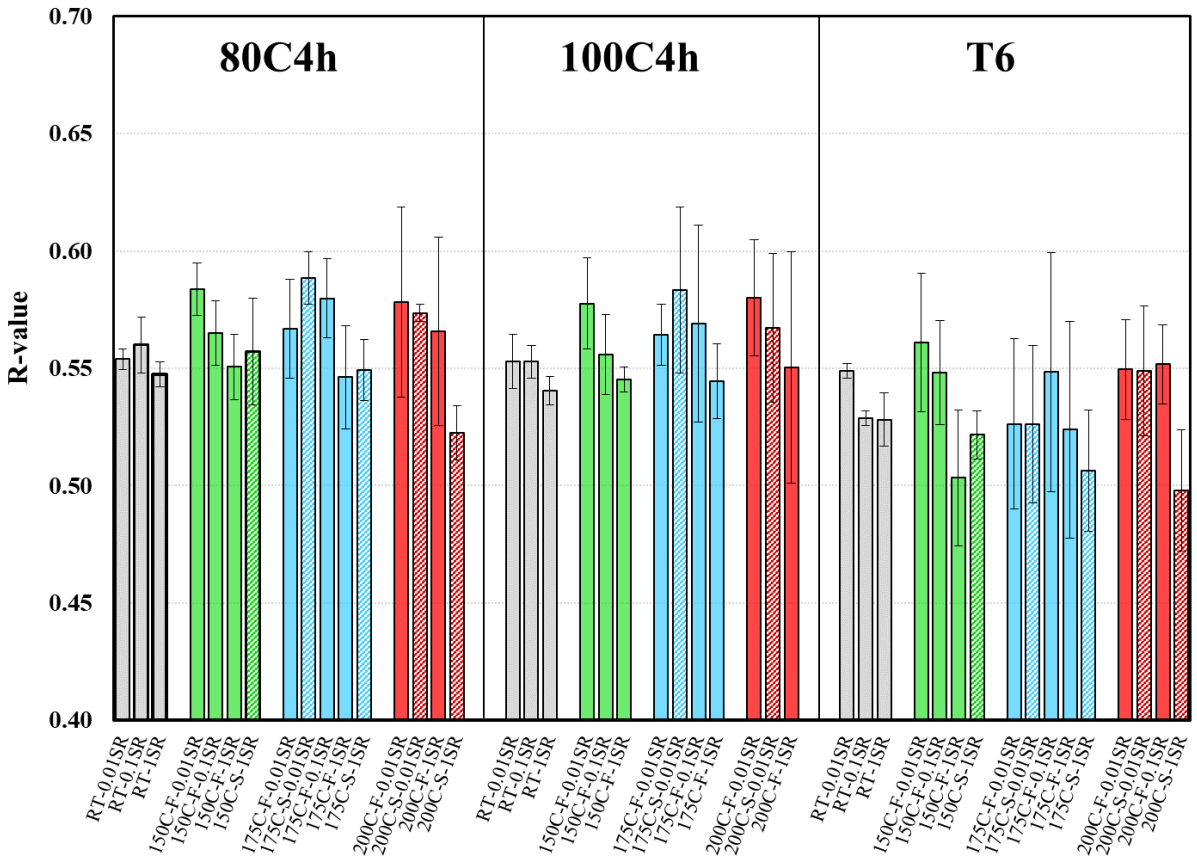

Figure 79. R-values of all conditions tested on the Stage 2 (Gleeble) of the process route selection.

Moreover, a preliminary study was conducted to evaluate the strain rate and strain path correction methods proposed by Choung *et al.* [74] and Omer *et al.* [73] (described in Appendix B.2). This numerical study evaluated the effects of the two correction methods on the tensile and Nakazima test models for the selected condition of 175C-100C4h-F. The slower 0.01 s^{-1} strain rate and 1 mm/s stroke rates tests were used for this study given the more noticeable effects when implementing the Choung *et al.*'s correction method, as shown in Figure 63 of Section 4.2.1.

As displayed in Figure 80 [Left], the difference in the results obtained using the Choung *et al.* [74] correction method was negligible, compared to those of the constrained ARM approach proposed by Omer *et al.* [73]. Similar behaviour has been observed in the Nakazima simulation results, Figure 80 [Right] (the Nakazima models are documented below).

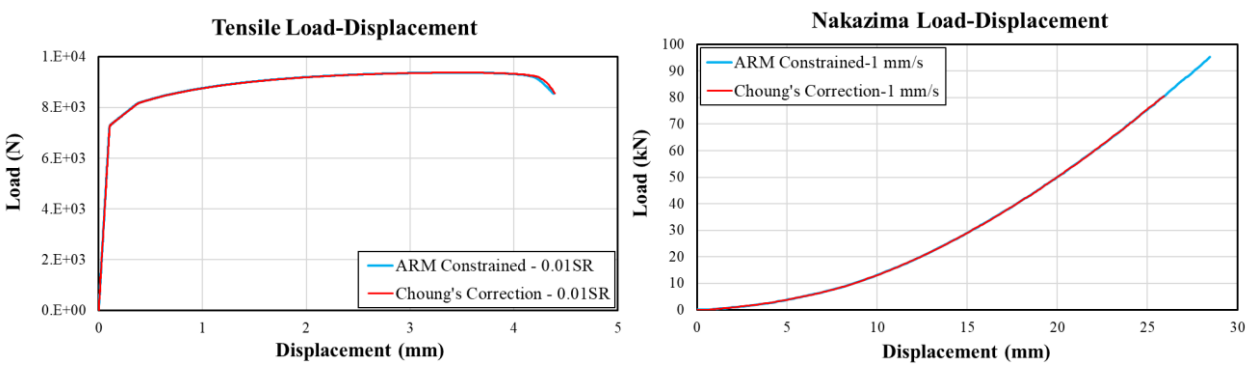

Figure 80. Evaluation of the Choung et al.'s correction method as assessed by [Left] Gleeble tests and [Right] Nakazima formability simulations, on the 175C-100C4h-F condition.

Therefore, due to the use of unnecessary assumptions (discussed in Chapter 2.2.3) and the insignificant effects that the Choung *et al*, *'s* correction method has shown on the simulated results, this approach was no longer considered.

5.1.2. Tensile Predictions

The numerical simulations accurately predicted the load-displacement response of the majority of Gleeble test conditions. As shown in Figures 81 and 82, the room temperature simulations are in good agreement with the experimental results.

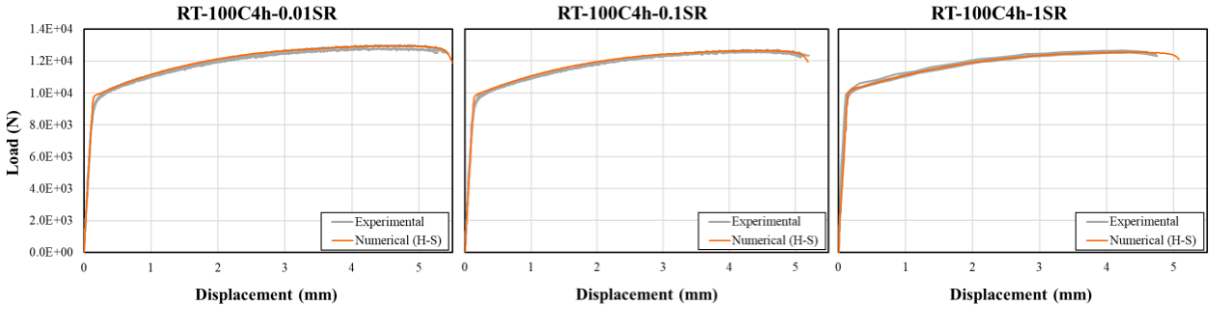

Figure 81. The room temperature predictions for the 100C4h temper at different strain rates.
Note: The simulated curves were cut-off at the onset of load-drops.

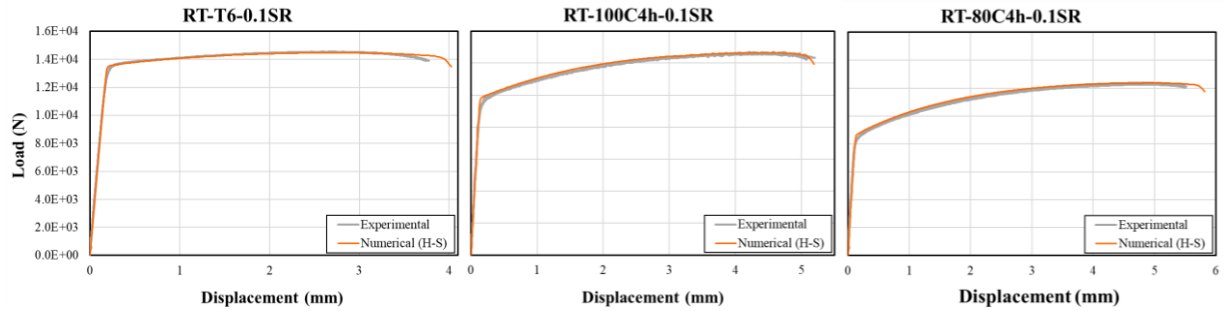

Figure 82. The room temperature predictions for the T6, 100C4h, and 80C4h tempers at the strain rate of 0.1 s^{-1}.
Note: The simulated curves were cut-off at the onset of load-drops.

However, at the elevated temperatures, some of the models failed to capture the full elongation, particularly at the lower (0.01 and 0.1 /s) strain rates, as seen in Figures 83 and 84.

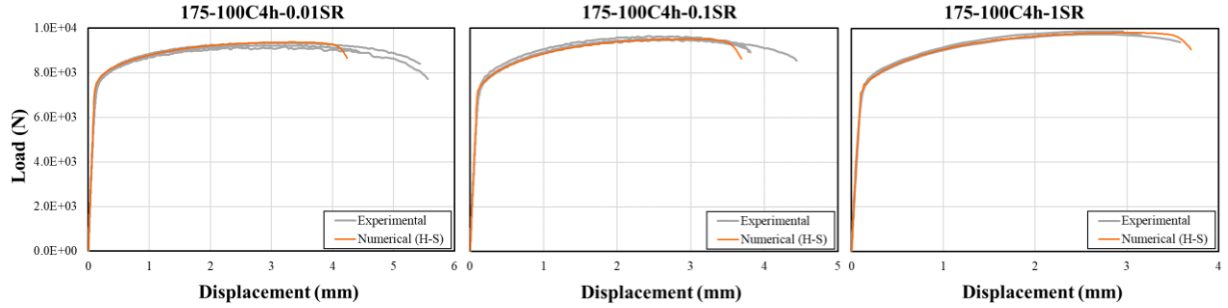

Figure 83. The elevated temperature predictions for the 100C4h temper at different strain rates.
Note: The simulated curves were cut-off at the onset of load-drops.

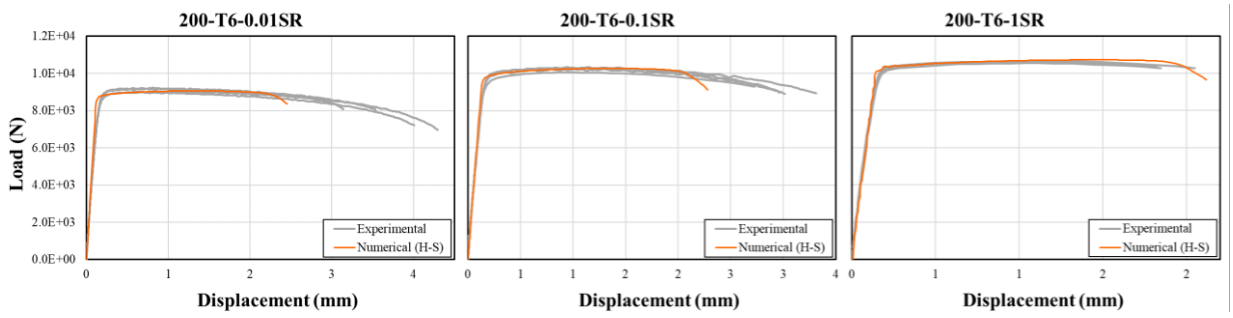

Figure 84. The elevated temperature predictions for the T6 temper at different strain rates.
Note: The simulated curves were cut-off at the onset of load-drops.

The predicted load-displacements are in good agreement up to the point of local necking, which occurs sooner than observed in the experiments. The premature onset of necking is likely due to the measured material rate sensitivity which is obscured in the Gleeble testing by the coupled effects of strain rate sensitivity and the dynamic aging during deformation, as discussed

in Chapter 4. It is anticipated that the actual elevated temperature strain rate sensitivity is higher than that measured using constant strain rate tensile tests; future work should consider strain rate jump tests to better separate strain rate sensitivity and aging effects during testing. In addition, the onset of local necking is known to be influenced significantly by the accuracy of the yield surface in the plane strain condition, which is not explicitly calibrated in the work by Rahmaan *et al.* [58]. Further work is required to improve the predictions to higher strain levels.

5.2. Warm Forming Numerical Analysis

This section provides details of the numerical warm forming model. The simulation results are assessed in terms of the predicted the load-displacement responses versus the measured data.

5.2.1. Finite Element Mesh

A quarter symmetry representation of the specimen and tooling, as shown in Figure 85 and 86. A fully integrated shell element formulation (ELFORM = 16) and five integration points were used to describe the deformable 2 mm blank. The tooling was treated as rigid. The dimensions of the plane strain blank were derived from the geometry in Figure 33. Further, the critical dimensions (*i.e.* die radius, die entry radius and the punch radius, along with relative positions) were identical to those described in Section 3.4.2.

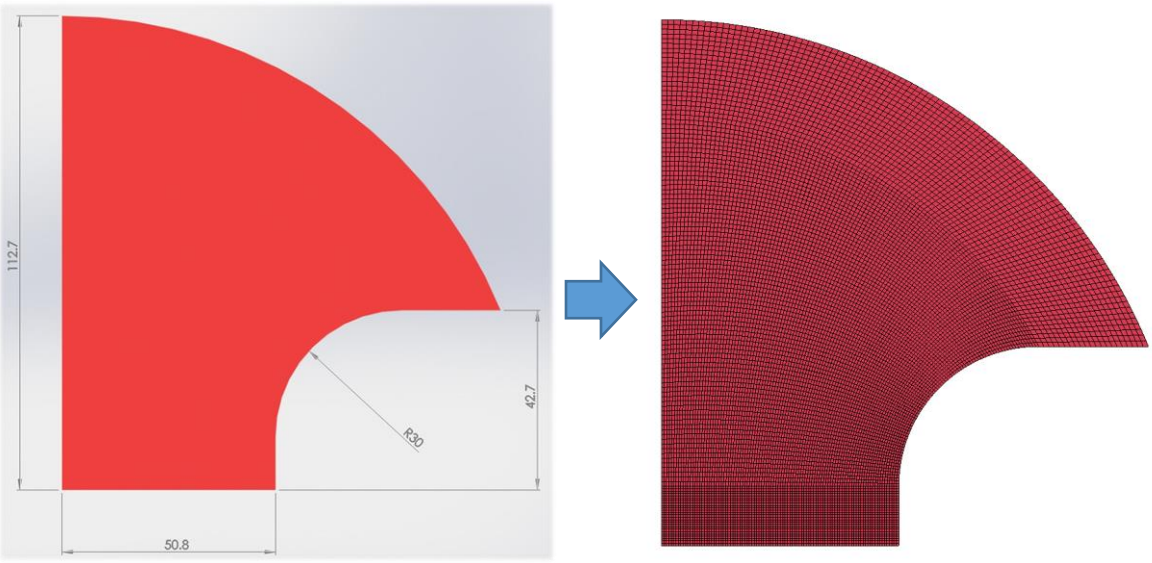

Figure 85. The quarter symmetry mesh used for the Nakazima dome specimen model (units in mm).

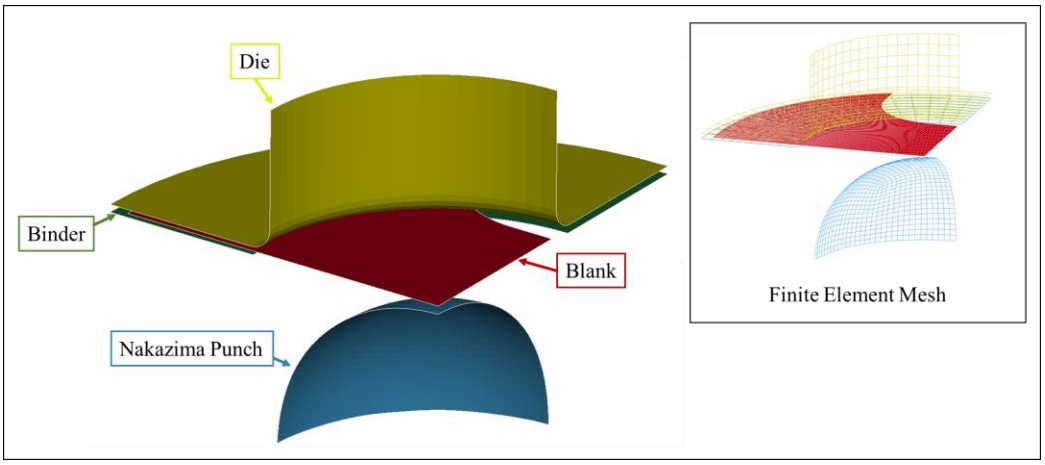

Figure 86. Plane Strain Nakazima simulation assembly.

The Gauss-Lobatto through-thickness integration approach was employed to predict the strains on the surface of the specimen. The shell elements used in this study are all comprised of quadrilateral elements with a minimum size of 0.5 mm at the center of the blank.

5.2.2. Boundary Conditions

5.2.2.1. Tooling Motion and Loads

A variable velocity, aiming to simulate the tooling motion during the warm forming process, was assigned to the moving toolset. Once the specimen was fully clamped in the die-set, the punch was assigned to advance into the blank. Following the force controlled clamping process, 5% of the punch displacement was allocated to the acceleration and deceleration on each end of the stroke motion. The remaining 90% was assigned as constant velocity, corresponding to the different experimental stroke rates. A quarter symmetry binder load of 10 tons (≈ 98 kN), was applied to prevent draw-in during deformation.

5.2.2.2. Temperature History

Furthermore, although relatively small deviations from the forming temperatures were measured on the heated tooling and the blanks, the full thermal histories were utilized in the

simulations to improve the accuracy of the model. Appendix A.3.2 presents the temperature curves corresponding to the warm forming components (tooling and blank) utilized in this numerical simulation. The timings for each step of the simulation, starting from blank insertion, were derived from these temperature histories. Table 3 in Chapter 3.4.2 also lists the key process parameters for all tests performed using the warm forming system. Moreover, the heat transfer coefficients, utilized in the thermal contact definitions, were adopted from the work of Omer *et al.* [114] (Table 7).

Table 7. The heat transfer coefficients of AA7075-T6 versus contact pressure obtained by Omer et al. [114]

Contact Pressure (MPa)	*HTC (W/m^2-K)*
2	*355*
5	*501*
10	*620*
20	*750*
40	*1010*
60	*1800*
80	*2803*

5.2.2.3. Friction

The coefficient of friction (COF) values utilized in this study were adopted from the work of Noder *et al.* [115]. The COF values of 0.007 and 0.037 – corresponding to the elevated and room temperature conditions, respectively – were utilized for the lubricated (Teflon) contact between the punch and the blank. For the unlubricated contact (clamping) regions (between the blank and the die-set) a COF of 0.35 was employed.

5.2.3. Warm Forming Predictions

The numerical models of the warm forming experiments provided fair predictions of the experimental data, with the faster stroke rate results being slightly more accurate than those of the slower tests. A similar systematic error has been observed across all tested conditions.

The predicted *versus* measured load-displacement curves for the 80C-4h temper are displayed in Figures 87 and 88 for forming temperatures of 150 and 175 °C, respectively. In these figures, the sudden drops in the experimental load-displacement curves correspond to the onset of failure.

Although the predictions are generally in good agreement with the experimental results, the simulations tend to initially underestimate, and later over-estimate the measured loads. Near the midpoint of the test, the slopes of the predicted load-displacements are shown to increase more rapidly compared to the experimental response, resulting in an overshoot in response.

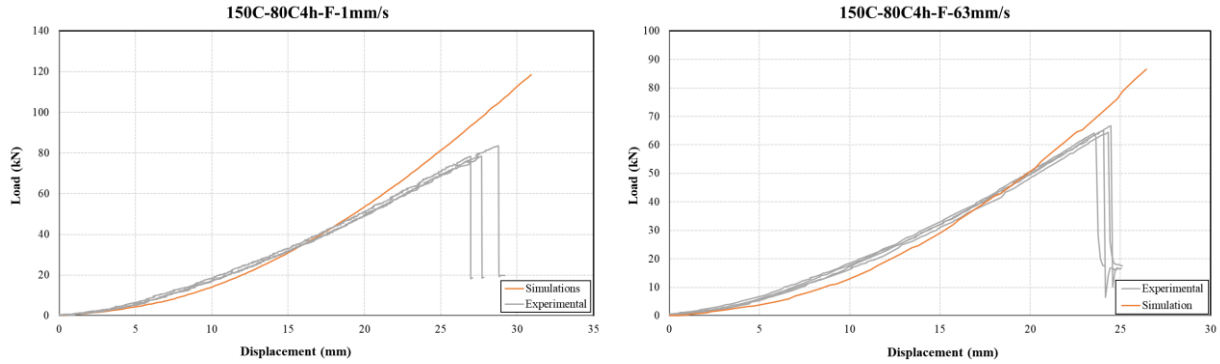

Figure 87. The load-displacement responses from the Nakazima formability experiments, for the 80C-4h temper, warm formed at 150 °C with the fast heating rates, at the stroke rates of [Left] 1 mm/s and [Right] 63 mm/s; compared to the corresponding simulated results.

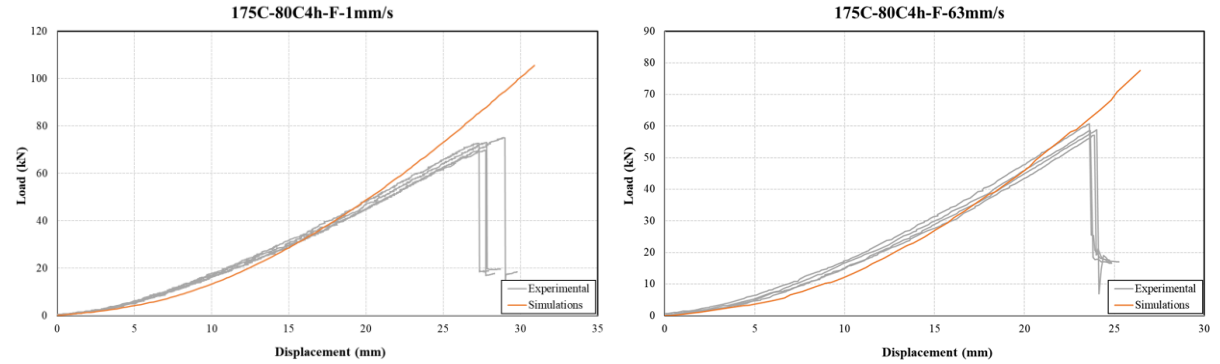

Figure 88. The load-displacement responses from the Nakazima formability experiments, for the 80C-4h temper, warm formed at 175 °C with the fast heating rates, at the stroke rates of [Left] 1 mm/s and [Right] 63 mm/s; compared to the corresponding simulated results.

Similar behaviours are observed for the 100C-4h tempers at the different forming temperatures, stroke rates, and heating rates as shown in Figures 89, 90 and 91.

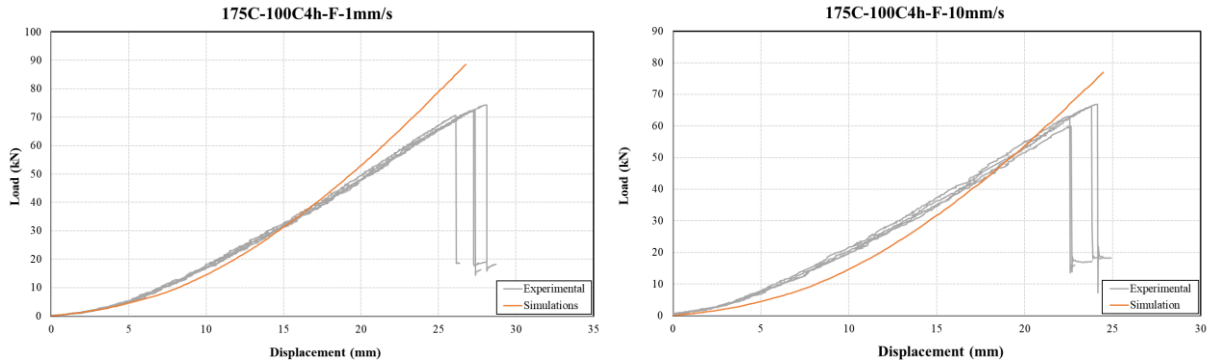

Figure 89. The load-displacement responses from the Nakazima formability experiments, for the 100C-4h temper, warm formed at 175 °C with the fast heating rates, at the stroke rates of [Left] 1 mm/s and [Right] 10 mm/s; compared to the corresponding simulated results.

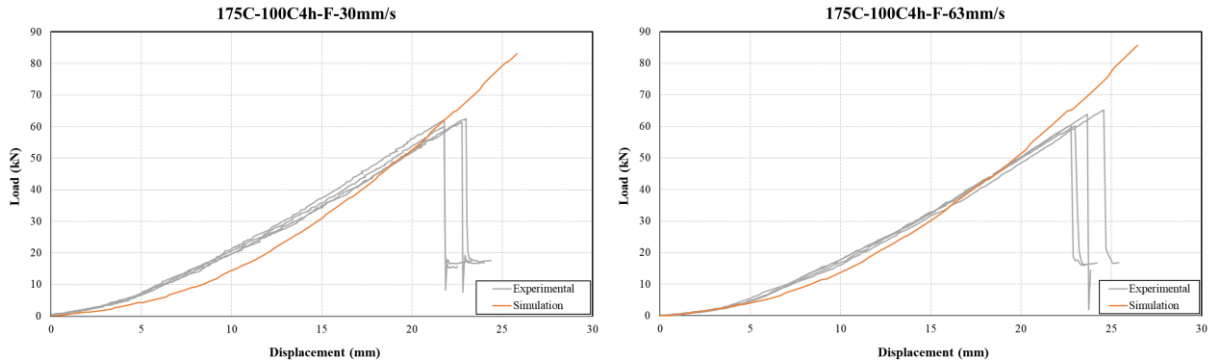

Figure 90. The load-displacement responses from the Nakazima formability experiments, for the 100C-4h temper, warm formed at 175 °C with the fast heating rates, at the stroke rates of [Left] 30 mm/s and [Right] 63 mm/s; compared to the corresponding simulated results.

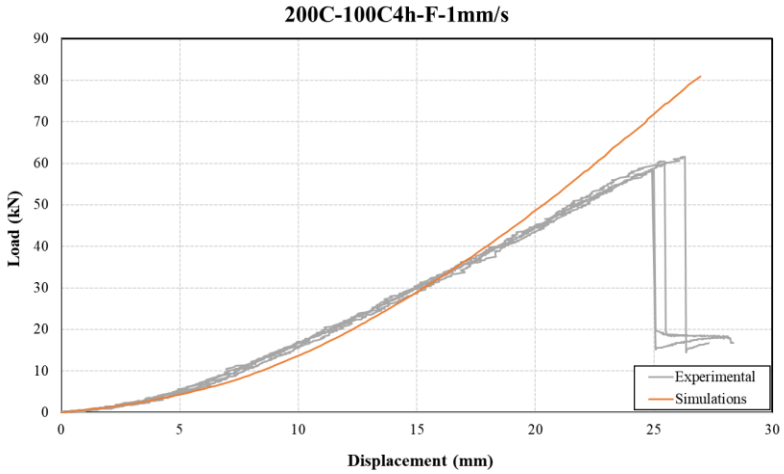

Figure 91. The load-displacement responses from the Nakazima formability experiments, for the 100C-4h temper, warm formed at 200 °C with the fast heating rates, at the stroke rate of 1 mm/s; compared to the corresponding simulated results.

Similarly, the T6 temper exhibited comparable trends as shown in Figures 92 and 93. The reduced elongations for the 1mm/s tests are likely caused by the rapid increase in the strain rates, and due to the lower ductility of this alloy, impaired by the same discrepancy in capturing an accurate strain rate sensitivity response as described in Section 5.1.2.

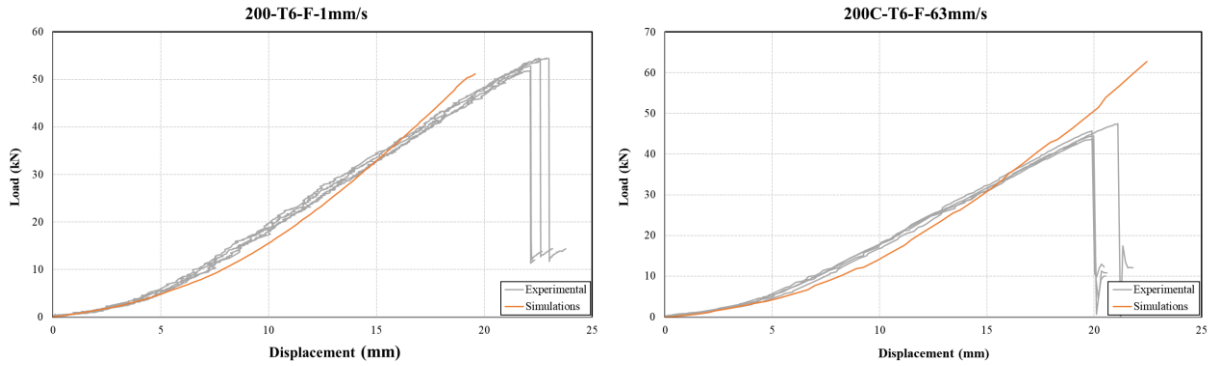

Figure 92. The load-displacement responses from the Nakazima formability experiments, for the T6 temper, warm formed at 200 °C with the fast heating rates, at the stroke rates of [Left] 1 mm/s and [Right] 63 mm/s; compared to the corresponding simulated results. Note: The simulated curve of the 1 mm/s test was cut-off at the onset of load-drop.

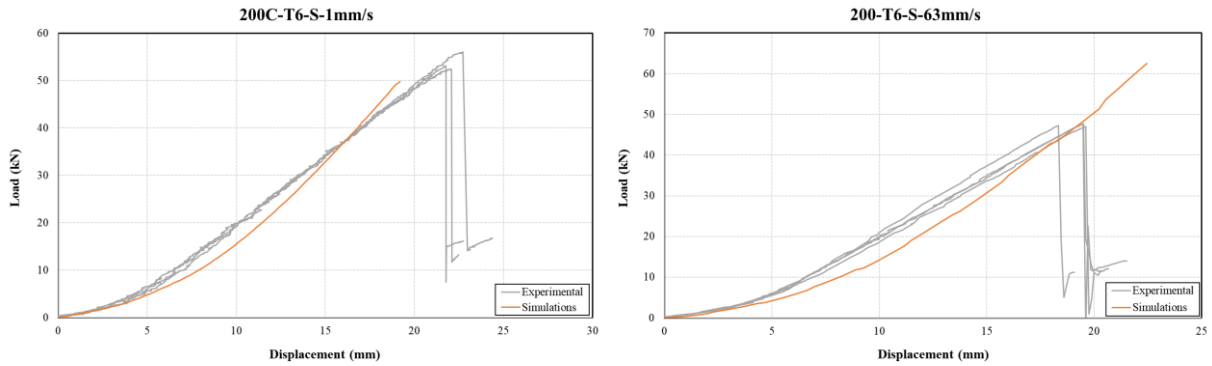

Figure 93. The load-displacement responses from the Nakazima formability experiments, for the T6 temper, warm formed at 200 °C with the slow heating rates, at the stroke rates of [Left] 1 mm/s and [Right] 63 mm/s; compared to the corresponding simulated results. Note: The simulated curve of the 1 mm/s test was cut-off at the onset of load-drop.

From this numerical study it can be deduced that the load displacement simulations of the Nakazima formability tests generally provide a moderately good prediction when compared to the experimental results; and follow the observed trends with systematic errors. The slow heating routes have yielded similar results, since the slightly over-aged specimens have also been exposed to similar thermo-mechanical processes during warm forming. The slightly more accurate response

of the faster stroke rate tests is likely due to the reduced effects of aging during deformation since the time at elevated temperature is reduced.

In this study, a different material card was produced for each of the three tempers, essentially treating them as different materials. However, integrating a dedicated precipitation hardening model, similar to the work of Omer *et al.* [67] and Kurukuri *et al.*[71], may be possible which would make use of all of the data obtained in this thesis within a unified material model. This integration may also help to decouple the aging and strain rate sensitivity effects within the constitutive response, as discussed in Chapter 5.2. To this end, strain rate jump tests, in which the strain rate is rapidly varied during a tensile test would be helpful to identify strain rate sensitivity for a given "aging state". Using this approach, the strain rate sensitivity can be better separated from the aging effects. Such methods can be expected to improve the prediction accuracies and provide a more complete material model for a larger range of process routes.

6. Conclusions and Recommendations

The peak (T6) temper of AA7075 aluminum alloy sheet has excellent specific strength, but exhibits inferior formability at room temperature. The current thesis has served to put forth a process route to enhance the manufacturability of AA7075, utilizing warm forming of under-aged (pre-aged) tempers, as well as warm forming of the T6 temper, to improve formability. The constitutive characteristics obtained at the different testing conditions were also characterized and utilized to devise the optimal process parameters to form this alloy.

6.1. Conclusions

The following conclusions are drawn:

- The pre-aged tempers displayed an enhanced work hardening response, compared to that of the T6 condition, and therefore better elongation and formability. PLC effects were prevalent for lower aging durations and temperatures, and impaired the repeatability of the results, however, PLC effects were much lower for the 4-hour pre-age conditions.

- Warm forming promoted increased formability, in terms of measured limit strain, for all selected temper conditions (T6, 100C4h, 80C4h). However, the measured increase in limit strain for the T6 temper was local; as a result, only marginal increases in dome height were observed for this temper. The lack of improvement in dome height for the T6 temper is attributed to the early onset of diffuse necking at elevated temperatures.

- In contrast to the T6 results, the under aged tempers exhibited strong work hardening at room and elevated temperature that delays the onset of diffuse necking. As a result, the under aged tempers exhibited significant improvement in both limit strain and dome heights to failure at elevated temperatures.

- Rapid heating reduced the extent of pre-aging and generally led to an increase in forming limit for the under aged tempers (up to 8% and 13% in terms of dome heights and major limit strains relative to the slow heated sample, respectively).

- From the numerical simulations, the Hockett-Sherby constitutive fits were shown to provide accurate predictions of the measured load-displacement response in the tensile experiments and moderately accurate predictions for the warm forming experiments.

- Based on the evaluation of the hardness of the different tempers before and after a PBC, following the forming process, the following conclusions were drawn:

    - Over-aging of the T6 temper is observed in response to the warm forming processes. However, this effect might be desirable if an over-aged T76 temper is sought for its superior stress corrosion cracking resistance.

    - The PBC process has shown to increase the hardness values of the warm formed T6 specimens, as a manifestation of the retrogression and re-aging effect. Evidence of this phenomena lies in the reduction in hardness values of the post warm formed T6 specimens, and the regain of the hardness values after a subsequent PBC.

    - The hardness of the 100C-4h temper, after paint bake and warm forming at 175 °C using the fast heating method, approached 97% of the hardness of the peak aged (T6) condition.

6.2. Recommendations

The constitutive dataset acquired in this work, along with the preliminary modelling work (Hockett-Sherby fits), represent a solid foundation for the further development of a more complete constitutive model. This model should include separate terms for *in situ* aging and recovery during warm forming with decoupling of strain rate sensitivity, along with work hardening and thermal softening effects. To decouple aging (during warm forming) and strain rate effects, strain rate jump tests should be performed for a range of initial aging conditions. Moreover, a parallel study on the boundary conditions and the size of the shell elements should also be devised to ensure optimal numerical model accuracy.

A full FLC characterization is recommended for the high performing conditions of 175C-100C4h, 175C-80C4h and 200C-T6, at a range of stroke rates (recommended 10-63 mm/s) using the fast heating approach. Further, large-scale component forming experiments should follow this characterization study for industrial validation of the warm forming process and models.

A detailed friction study is recommended with precise load cells to capture the low coefficients of friction observed with the current lubrication method. Also, considering the relatively low forming temperatures, industrial lubrications, such as FUCHS Forge Ease AL278 and RENOFORM 2502, should be examined to evaluate the friction levels achievable in warm forming (since Teflon is not a realistic option for large scale manufacturing).

Furthermore, tensile tests performed on parts subjected to warm forming (pre-straining), before and after the PBC, are needed to complement the hardness evaluation study presented in this thesis, and provide a more complete characterization of the post-formed states. Additionally, it is also recommended to evaluate the stress corrosion cracking response of the high performing conditions in future work.

Lastly, a longer pre-aging duration (more than 4 hours) at the lowest pre-aging temperature of 80 °C should be considered to examine the potential reduction in the PLC effect and improvement in formability with further aging.

References:

[1] G8, “Declaration of the Leaders: The Major Economies Forum on Energy and Climate,” 2009. [Online]. Available: http://www.g8.utoronto.ca/summit/2009laquila/2009-mef.html.

[2] Government of Canada, “Greenhouse gas emission regulations,” 2018. [Online]. Available: https://www.canada.ca/en/environment-climate-change/services/climate-change/greenhouse-gas-emissions/regulations.html#X-201105241638261.

[3] Government of Canada, “Canada’s actions to reduce emissions,” 2020. [Online]. Available: https://www.canada.ca/en/services/environment/weather/climatechange/climate-plan/reduce-emissions.html.

[4] International Energy Agency, “Explore energy data by category, indicator, country or region,” 2018. [Online]. Available: https://www.iea.org/data-and-statistics?country=CANADA&fuel=CO2 emissions&indicator=CO2BySource.

[5] Canada Energy Regulator, “Market Snapshot: How does Canada rank in terms of vehicle fuel economy?,” 2019. [Online]. Available: https://www.cer-rec.gc.ca/en/data-analysis/energy-markets/market-snapshots/2019/market-snapshot-how-does-canada-rank-in-terms-vehicle-fuel-economy.html.

[6] International Energy Agency, “International Energy Agency,” 2017. [Online]. Available: https://www.iea.org/.

[7] Canada Energy Regulator, “Market Snapshot Share of truck sales are at a record high in Canada,” 2018. [Online]. Available: https://www150.statcan.gc.ca/n1/en/type/data?text=790003.

[8] Statistics Canada, “Statistics Canada.” [Online]. Available: https://www.statcan.gc.ca/eng/start.

[9] U.S. Department of Transportation, “Corporate Average Fuel Economy (CAFE) Standards,” 2014. [Online]. Available: https://www.transportation.gov/mission/sustainability/corporate-average-fuel-economy-cafe-standards.

[10] INTERNATIONAL COUNCIL ON CLEAN TRANSPORTATION, “Summary of the Trump

Administration's fatally flawed U.S. light-duty vehicle efficiency standards," 2020. .

[11] THE WHITE HOUSE, "FACT SHEET : President Biden Sets 2030 Greenhouse Gas Pollution Reduction Target Aimed at Creating Good-Paying Union Jobs and Securing U . S . Leadership on Clean Energy Technologies," 2021. [Online]. Available: https://www.whitehouse.gov/briefing-room/statements-releases/2021/04/22/fact-sheet-president-biden-sets-2030-greenhouse-gas-pollution-reduction-target-aimed-at-creating-good-paying-union-jobs-and-securing-u-s-leadership-on-clean-energy-technologies/.

[12] Canada Energy Regulator, "Market Snapshot Vehicle emissions standards will reduce gasoline use," 2018. [Online]. Available: https://www.cer-rec.gc.ca/en/data-analysis/energy-markets/market-snapshots/2018/market-snapshot-vehicle-emissions-standards-will-reduce-gasoline-use.html.

[13] U.S. National Highway Transportation Safety Authority, "NHTSA 2017-2025." .

[14] NEB calculations, "Canada's Energy Future 2017.pdf." .

[15] J. German and N. Lutsey, "Size or Mass? The Technical Rationale for Selecting Size as an Attribute for Vehicle Efficiency Standards," no. 9, 2010.

[16] L. V. F. Economy, E. Systems, and P. Sciences, *Assessment of fuel economy technologies for light-duty vehicles*. 2011.

[17] A. Renski, "Investigation of the Influence of the Centre of Gravity Position on the Course of Vehicle Rollover," *Esv*, vol. 1, no. 15, pp. 1–12, 2015.

[18] M. Redelbach, E. D. Özdemir, and H. E. Friedrich, "Optimizing battery sizes of plug-in hybrid and extended range electric vehicles for different user types," *Energy Policy*, vol. 73, pp. 158–168, 2014.

[19] IEA, "Fuel Consumption of Cars and Vans," 2020. [Online]. Available: https://www.iea.org/reports/fuel-consumption-of-cars-and-vans.

[20] H.-H. Braess and U. Seiffert, *Vieweg handbook automotive technology*. Springer Vieweg, 2011.

[21] J. M. Runge, *The metallurgy of anodizing aluminum: Connecting science to practice*. 2018.

[22] E. L. Osborn, "From bauxite to cooking pots: Aluminum, chemistry, and West African artisanal

production," *Hist. Sci.*, vol. 54, no. 4, pp. 425–442, 2016.

[23] H. Deville, *de L'Aluminium*. Taschenbuch, 1859.

[24] RUSAL, "The history of the aluminium industry." [Online]. Available: Aluminiumleader.com.

[25] C. M. HALL, "PROCESS OF REDUCING ALUMINUM BY ELECTROLYSIS," 400,766, 1889.

[26] A. Wilm, "A. Metallurgie," 8, 223, 650, 1911.

[27] C. A. Ungureanu, S. Das, and I. S. Jawahir, "Life-cycle Cost Analysis: Aluminum versus Steel in Passenger Cars," *Miner. Met. Mater. Soc.*, vol. 273, no. 7310, p. 136, 2007.

[28] H. Wang, Y. B. Luo, P. Friedman, M. H. Chen, and L. Gao, "Warm forming behavior of high strength aluminum alloy AA7075," *Trans. Nonferrous Met. Soc. China (English Ed.*, vol. 22, no. 1, pp. 1–7, 2012.

[29] N. Sotirov, P. Simon, C. Chimani, D. Uffelmann, and C. Melzer, "Warm Deep Drawability of Peak-Aged 7075 Aluminium Sheet Alloy," *Key Eng. Mater.*, vol. 504–506, no. 0, pp. 955–960, 2012.

[30] S. Polak *et al.*, "Warm forming of 7075 aluminum alloys," *Procedia Eng.*, vol. 207, pp. 2399–2404, 2017.

[31] J. A. Österreicher *et al.*, "Warm-forming of pre-aged Al-Zn-Mg-Cu alloy sheet," *Mater. Des.*, vol. 193, p. 108837, 2020.

[32] Y. S. Lee, D. H. Koh, H. W. Kim, and Y. S. Ahn, "Improved bake-hardening response of Al-Zn-Mg-Cu alloy through pre-aging treatment," *Scr. Mater.*, vol. 147, pp. 45–49, 2018.

[33] E. E. Batukhtina, V. A. Romanova, R. R. Balokhonov, and V. S. Shakhijanov, "A crystal plasticity model for the deformation behavior of aluminum single crystals," *AIP Conf. Proc.*, vol. 1785, no. November, 2016.

[34] D. A. PORTER, K. E. EASTERLING, and M. Y. SHERIF, *Phase Transformations in Metals and Alloys*, Third. Florida: CRC Press Taylor & Francis Group, 2009.

[35] D. J. Lloyd and M. C. Chaturvedi, "A calorimetric study of aluminium alloy AA-7075," *J. Mater. Sci.*, vol. 17, no. 6, pp. 1819–1824, 1982.

[36] A. Deschamps and Y. Brechet, "Influence of predeformation and ageing of an Al-Zn-Mg Alloy-II.

Modeling of precipitation kinetics and yield stress," *Acta Mater.*, vol. 47, no. 1, pp. 293–305, 1998.

[37] S. Esmaeili, D. J. Lloyd, and W. J. Poole, "Modeling of precipitation hardening for the naturally aged Al-Mg-Si-Cu alloy AA6111," *Acta Mater.*, vol. 51, no. 12, pp. 3467–3481, 2003.

[38] P. Ratchev, B. Verlinden, P. De Smet, and P. Van Houtte, "Precipitation hardening of an Al-4.2 wt% Mg-0.6 wt% Cu alloy," *Acta Mater.*, vol. 46, no. 10, pp. 3523–3533, 1998.

[39] MatWeb, "Aluminum 7075-T6; 7075-T651." [Online]. Available: http://www.matweb.com/search/DataSheet.aspx?MatGUID=4f19a42be94546b686bbf43f79c51b7d&ckck=1.

[40] MatWeb, "Aluminum 7075-T76; 7075-T7651." [Online]. Available: http://www.matweb.com/search/datasheet.aspx?MatGUID=e1adabad6c1b4fed99133c4b135303a8.

[41] D. S. Mackenzie and H. International, "Heat Treatment Practice of Wrought Age-Hardenable Aluminum Alloys," *Alum. Sci. Technol.*, vol. 2, pp. 462–477, 2018.

[42] R. C. Jr, B. Coughran, I. Traina, A. Hernandez, T. Scheck, and C. Etuk, "On the correlation of mechanical and physical properties of 7075-T6 Al alloy," vol. 12, pp. 520–526, 2005.

[43] D. Wang, D. R. Ni, and Z. Y. Ma, "Effect of pre-strain and two-step aging on microstructure and stress corrosion cracking of 7050 alloy," vol. 494, pp. 360–366, 2008.

[44] A. Deschamps, F. Livet, and Y. Bréchet, "Influence of predeformation on ageing in an Al-Zn-Mg alloy-I. Microstructure evolution and mechanical properties," *Acta Mater.*, vol. 47, no. 1, pp. 281–292, 1998.

[45] S. V. Emani, J. Benedyk, P. Nash, and D. Chen, "Double aging and thermomechanical heat treatment of AA7075 aluminum alloy extrusions," *J. Mater. Sci.*, vol. 44, no. 23, pp. 6384–6391, 2009.

[46] B.-A. Behrens, S. Hübner, H. Vogt, O. Golovko, S. Behrens, and F. Nürnberger, "Mechanical properties and formability of EN AW-7075 in cold forming processes Mechanical properties and formability of EN AW-7075 in cold forming processes," *Int. Deep. Res. Gr. (IDDRG 2020)*, vol. 967, 2020.

[47] A. Deschamps *et al.*, “Low-temperature dynamic precipitation in a supersaturated Al-Zn-Mg alloy and related strain hardening,” *Philos. Mag. A Phys. Condens. Matter, Struct. Defects Mech. Prop.*, vol. 79, no. 10, pp. 2485–2504, 1999.

[48] H. Aboulfadl, J. Deges, P. Choi, and D. Raabe, “Dynamic strain aging studied at the atomic scale,” *Acta Mater.*, vol. 86, pp. 34–42, 2015.

[49] A. H. COTTRELL, “LXXXVI. A Note on the Portevin-Le Chatelier Effect,” *Philos. Mag.*, 1953.

[50] G. Ananthakrishna, “Current theoretical approaches to collective behavior of dislocations,” vol. 440, pp. 113–259, 2007.

[51] A. Portevin and F. Le Chatelier, “Sur un phénomène observé lors de l’essai de traction d’alliages en cours de transformation,” *Comptes Rendus l’Académie des Sci.*, vol. 176, pp. 507–510, 1923.

[52] H. Halim, D. S. Wilkinson, and M. Niewczas, “The Portevin-Le Chatelier (PLC) effect and shear band formation in an AA5754 alloy,” *Acta Mater.*, vol. 55, no. 12, pp. 4151–4160, 2007.

[53] A. Mogucheva, M. Saenko, and R. Kaibyshev, “The Portevin-Le Chatelier effect in an Al-Mg alloy,” *AIP Conf. Proc.*, vol. 1783, 2016.

[54] P. G. McCormigk, “A model for the Portevin-Le Chatelier effect in substitutional alloys,” *Acta Metall.*, vol. 20, no. 3, pp. 351–354, 1972.

[55] B. J. Brindley, P. J. Worthington, B. J. Brindley, and P. J. Worthington, “Yield-point phenomena in substitutional alloys Yield-point phenomena in substitutional alloys,” vol. 6690, no. 1970, 2013.

[56] J. A. Österreicher, G. Kirov, S. S. A. Gerstl, E. Mukeli, F. Grabner, and M. Kumar, “Stabilization of 7xxx aluminium alloys,” *J. Alloys Compd.*, vol. 740, pp. 167–173, 2018.

[57] T. Rahmaan, C. Butcher, and M. J. Worswick, “Constitutive response of AA7075-T6 aluminum alloy sheet in tensile and shear loading,” *Conf. Proc. Soc. Exp. Mech. Ser.*, vol. 4, pp. 115–122, 2017.

[58] T. Rahmaan, J. Noder, A. Abedini, P. Zhou, C. Butcher, and M. J. Worswick, “Anisotropic plasticity characterization of 6000- and 7000-series aluminum sheet alloys at various strain rates,” *Int. J. Impact Eng.*, vol. 135, no. December 2018, p. 103390, 2020.

[59] G. C. Soares, M. C. M. Rodrigues, and L. De Arruda Santos, “Influence of temperature on

mechanical properties, fracture morphology and strain hardening behavior of a 304 stainless steel," *Mater. Res.*, vol. 20, no. June, pp. 141–151, 2017.

[60] M. H. Cai, H. Ding, Z. Y. Tang, H. Y. Lee, and Y. K. Lee, "Strain hardening behavior of high performance FBDP, TRIP and TWIP steels," *Steel Res. Int.*, vol. 82, no. 3, pp. 242–248, 2011.

[61] R. L. and W. P.I., "Z. Metallkd," vol. 4, p. 226, 1983.

[62] S. Esmaeili, D. J. Lloyd, and W. J. Poole, "A yield strength model for the Al-Mg-Si-Cu alloy AA6111," *Acta Mater.*, vol. 51, no. 8, pp. 2243–2257, 2003.

[63] L. Brown and R. Ham, "Strengthening Methods in Crystals," 1971, p. 12.

[64] A. Ardell, "Prediction of yield strength in a polycrystalline nickel base superalloy during interrupt cooling," *Met. Trans A*, vol. 16A, p. 2131, 1985.

[65] D. J. Lloyd, "Proc. 7th Int Conf on the Strength of Metals and Alloys," *7th Int Conf Strength Met. Alloy.*, vol. 3, p. 1745, 1985.

[66] L. M. Cheng, W. J. Poole, J. D. Embury, and D. J. Lloyd, "The influence of precipitation on the work-hardening behavior of the aluminum alloys AA6111 and AA7030," *Metall. Mater. Trans. A Phys. Metall. Mater. Sci.*, vol. 34 A, no. 11, pp. 2473–2481, 2003.

[67] K. Omer, "On the Response of 7000-Series Aluminum Alloys to Hot Stamping," 2019.

[68] F. Fazeli, W. J. Poole, and C. W. Sinclair, "Modeling the effect of Al3Sc precipitates on the yield stress and work hardening of an Al-Mg-Sc alloy," *Acta Mater.*, vol. 56, no. 9, pp. 1909–1918, 2008.

[69] F. Barlat *et al.*, "Plane stress yield function for aluminum alloy sheets - Part 1: Theory," *Int. J. Plast.*, vol. 19, no. 9, pp. 1297–1319, 2003.

[70] J. E. Hockett and O. D. Sherby, "Large strain deformation of polycrystalline metals at low homologous temperatures," *J. Mech. Phys. Solids*, vol. 23, no. 2, pp. 87–98, 1975.

[71] S. Kurukuri, M. J. Worswick, and S. Winkler, "Constitutive modelling of aluminium alloy sheet at warm forming temperatures," *J. Phys. Conf. Ser.*, vol. 734, no. 3, 2016.

[72] K. Omer, C. Butcher, and M. Worswick, "Characterization and application of a constitutive model for two 7000-series aluminum alloys subjected to hot forming," *Int. J. Mech. Sci.*, vol. 165, p.

105218, 2020.

[73] K. Omer, C. Butcher, and M. Worswick, “Characterization and application of a constitutive model for two 7000-series aluminum alloys subjected to hot forming,” *Int. J. Mech. Sci.*, vol. 165, no. November 2018, p. 105218, 2020.

[74] J. M. Choung and S. R. Cho, “Study on true stress correction from tensile tests,” *J. Mech. Sci. Technol.*, vol. 22, no. 6, pp. 1039–1051, 2008.

[75] I. Scheider, W. Brocks, and A. Cornec, “Procedure for the determination of true stress-strain curves from tensile tests with rectangular cross-section specimens,” *J. Eng. Mater. Technol. Trans. ASME*, vol. 126, no. 1, pp. 70–76, 2004.

[76] S. P. Keeler, “PLASTIC INSTABILITY AND FRACTURE IN SHEET STRETCHED OVER RIGID PUNCHES,” 1961.

[77] I. Formability, “Forming Limit Curve (FLC) and Forming Limit Diagram (FLD),” vol. 1.

[78] W. F. Hosford and R. M. Caddell, *Metal forming: Mechanics and metallurgy*. 2011.

[79] Z. Marciniak, J. L. Duncan, and S. J. Hu, *Mechanics of Sheet Metal Forming*. Butterworth-Heinemann, 2002.

[80] R. Bagheriasl and M. J. Worswick, “Formability of AA3003 brazing sheet at elevated temperatures: Limiting dome height experiments and determination of forming limit diagrams,” *Int. J. Mater. Form.*, vol. 8, no. 2, pp. 229–244, 2015.

[81] M. Boba, C. Butcher, N. Panahi, M. J. Worswick, R. K. Mishra, and J. T. Carter, “Warm forming limits of rare earth-magnesium alloy ZEK100 sheet,” *Int. J. Mater. Form.*, vol. 10, no. 2, pp. 181–191, 2017.

[82] D. Li and A. K. Ghosh, “Biaxial warm forming behavior of aluminum sheet alloys,” *J. Mater. Process. Technol.*, vol. 145, no. 3, pp. 281–293, 2004.

[83] S. DiCecco, M. Di Ciano, C. Butcher, and M. Worswick, “Numerical and experimental investigation of the formability of AA6013-T6,” *J. Phys. Conf. Ser.*, vol. 896, no. 1, 2017.

[84] J. R. Davis, “Aluminum and Aluminum Alloys.” ASM International, Russell Township, Geauga County, 1993.

[85] H. Pishyar, S. DiCecco, and M. Worswick, “Warm Forming Characteristics of AA7050-T6,” *IOP Conf. Ser. Mater. Sci. Eng.*, vol. 651, no. 1, 2019.

[86] K. Nakazima, T. Kikuma, and K. Hasuka, “Study on the Formability of Steel Sheets,” *Yamata Tech. Rep.*, vol. 264, pp. 8517–8530, 1968.

[87] Z. Marciniak, K. Kuczyi, and S. K. I. Warsaw, “LIMIT STRAINS IN THE PROCESSES OF STRETCH-FORMING SHEET METAL,” vol. 9, pp. 609–620, 1967.

[88] M. A. Sutton, O. Jean-Jose, and S. H. W., *Image Correlation for Shape, Motion, and Deformation Measurements*. 2009.

[89] W. Volk and P. Hora, “New algorithm for a robust user-independent evaluation of beginning instability for the experimental FLC determination,” *Int. J. Mater. Form.*, vol. 4, no. 3, pp. 339–346, 2011.

[90] S. Dicecco, C. Butcher, M. Worswick, E. Boettcher, E. Chu, and C. Shi, “Determination of forming limit diagrams of AA6013-T6 aluminum alloy sheet using a time and position dependent localized necking criterion,” *IOP Conf. Ser. Mater. Sci. Eng.*, vol. 159, no. 1, 2016.

[91] International Organization for Standardization, *ISO/DIC 12004-2:2008. metallic materials sheet and strip –Determination of forming limit curves –Part 2: determination of forming limit curves in the laboratory*. 2008.

[92] G. Huang, S. Sriram, and B. Yan, “Digital Image Correlation Technique and its Application in Forming Limit Curve Determination,” *International Deep Drawing Research Group*. Olofström, Sweden, pp. 153–162, 2008.

[93] W. Hotz, M. Merklein, A. Kuppert, H. Friebe, and M. Klein, “Time dependent FLC determination - Comparison of different algorithms to detect the onset of unstable necking before fracture,” *Key Eng. Mater.*, vol. 549, pp. 397–404, 2013.

[94] J. Min, T. B. Stoughton, J. E. Carsley, and J. Lin, “Comparison of DIC Methods of Determining Forming Limit Strains,” *Procedia Manuf.*, vol. 7, pp. 668–674, 2017.

[95] J. Min, T. B. Stoughton, J. E. Carsley, and J. Lin, “A Method of Detecting the Onset of Localized Necking Based on Surface Geometry Measurements,” *Exp. Mech.*, vol. 57, no. 4, pp. 521–535, 2017.

[96] J. Min, T. B. Stoughton, J. E. Carsley, and J. Lin, “An improved curvature method of detecting the onset of localized necking in Marciniak tests and its extension to Nakazima tests,” *Int. J. Mech. Sci.*, vol. 123, no. February, pp. 238–252, 2017.

[97] K. Wang, J. E. Carsley, B. He, J. Li, and L. Zhang, “Measuring forming limit strains with digital image correlation analysis,” *J. Mater. Process. Technol.*, vol. 214, no. 5, pp. 1120–1130, 2014.

[98] J. Noder and C. Butcher, “A comparative investigation into the influence of the constitutive model on the prediction of in-plane formability for Nakazima and Marciniak tests,” *Int. J. Mech. Sci.*, vol. 163, no. August, 2019.

[99] T. B. Stoughton, “General forming limit criterion for sheet metal forming,” *Int. J. Mech. Sci.*, vol. 42, no. 1, pp. 1–17, 2000.

[100] T. B. Stoughton and X. Zhu, “Review of theoretical models of the strain-based FLD and their relevance to the stress-based FLD,” *Int. J. Plast.*, vol. 20, no. 8–9, pp. 1463–1486, 2004.

[101] K. Elangovan, C. S. Narayanan, and R. Narayanasamy, “Modelling of forming limit diagram of perforated commercial pure aluminium sheets using artificial neural network,” *Comput. Mater. Sci.*, vol. 47, no. 4, pp. 1072–1078, 2010.

[102] N. Kotkunde, A. D. Deole, and A. Kumar, “Prediction of Forming Limit Diagram for Ti-6Al-4V Alloy Using Artificial Neural Network,” *MSPRO*, vol. 6, no. Icmpc, pp. 341–346, 2014.

[103] United Aluminum, “Chemical Composition and Properties of Aluminum Alloys,” 2020. [Online]. Available: https://unitedaluminum.com/chemical-composition-and-properties-of-aluminum-alloys/.

[104] A. G. Leacock, C. Howe, D. Brown, O. G. Lademo, and A. Deering, “Evolution of mechanical properties in a 7075 Al-alloy subject to natural ageing,” *Mater. Des.*, vol. 49, pp. 160–167, 2013.

[105] ASTM E8, “ASTM E8/E8M standard test methods for tension testing of metallic materials,” *Annu. B. ASTM Stand. 4*, no. C, pp. 1–27, 2010.

[106] S. DiCecco, “Personal Communication.” Waterloo, 2021.

[107] S. Lu, “Personal Communication.” Waterloo, 2021.

[108] R. George, “Personal Communication.” Waterloo, 2021.

[109] X. Tag, D. X. X. Armin, D. X. X. Cliff, D. X. X. Michael, and J. W. D. X. X, “International Journal of Impact Engineering Investigation into the shear stress , localization and fracture behaviour of DP600 and AA5182-O sheet metal alloys under elevated strain rates,” *Int. J. Impact Eng.*, vol. 108, pp. 303–321, 2017.

[110] A. Zhumagulov, “Personal Communication.” Waterloo, 2021.

[111] T. Rahmaan, P. Zhou, C. Butcher, and M. J. Worswick, “Strain rate and thermal softening effects in shear testing of AA7075-T6 sheet,” vol. 02037, pp. 1–6, 2018.

[112] F. J. Zerilli and R. W. Armstrong, “Dislocation-mechanics-based constitutive relations for material dynamics calculations,” *J. Appl. Phys.*, vol. 61, no. 5, pp. 1816–1825, 1987.

[113] A. Karaaslan, I. Kaya, and H. Atapek, “Effect of aging temperature and of retrogression treatment time on the microstructure and mechanical properties of alloy AA 7075,” *Met. Sci. Heat Treat.*, vol. 49, no. 9–10, pp. 443–447, 2007.

[114] K. Omer, S. Kim, C. Butcher, and M. Worswick, “Characterizing the Constitutive Properties of AA7075 for Hot Forming,” *J. Phys. Conf. Ser.*, vol. 896, no. 1, 2017.

[115] J. Noder, R. George, C. Butcher, and M. J. Worswick, “Friction Characterization and Application to Warm Forming of a High Strength 7000-Series Aluminum Sheet,” *J. Mater. Process. Technol.*, p. 117066, 2021.

[116] N. Deng and Y. P. Korkolis, “Elastic anisotropy of dual-phase steels with varying martensite content,” *Int. J. Solids Struct.*, vol. 141–142, pp. 264–278, 2018.

Appendix

A. Process Control - Temperature Validation

This appendix provides supporting data concerning the temperature settings and process histories associated with the various furnaces and heating apparatuses, utilized in the heat treatment and warm forming of the tested specimens. Note that the Gleeble heating apparatus is presented in the Appendix B. Temperature histories in the duration of the heating processes are provided to showcase the temperature uniformity and stability for each apparatus.

A.1. Heat Treatment Furnace

A convection DelTech furnace (DT-20) was utilized to heat treat (solutionize and pre-age) the Nakazima dome test specimens. This section presents results from a study of the steady state and transient conditions within the furnace to verify the heat treatment temperatures and durations.

First, a frame was fabricated to support multiple blanks within the furnace and enable batch processing during the heat-treatment process. This frame was also used to evaluate the temperature distribution within the furnace. To assess the initial thermal state of the furnace, instrumented specimens (utilizing K-type thermocouples, or TCs) were placed on the fixture as shown in Figure 94.

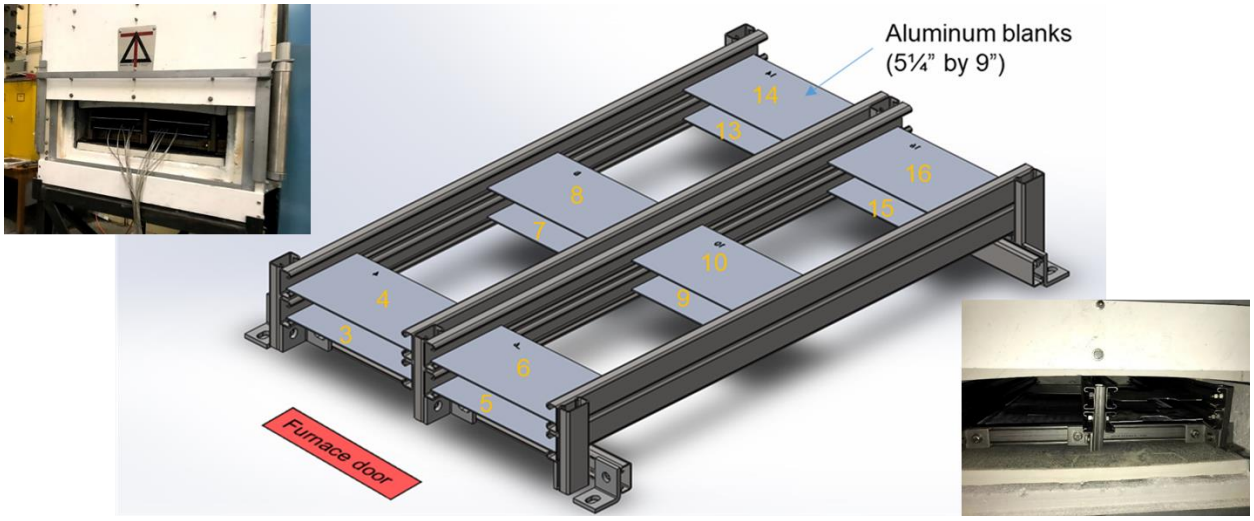

Figure 94. The batch heat-treatment processing fixture. The Thermocouples (TCs) attached to the instrumented blanks were numbered, from 3 to 16 (TC_3 to TC16).

The large variance in the temperature data (Figure 95) close to the furnace door on the lower shelves of the frame (TC_3 and TC_5), denote the severity of the non-uniform temperature distribution within the DT-20 convection furnace. A reverse CFD analysis, Figure 96, highlights the thermal gradients within the furnace.

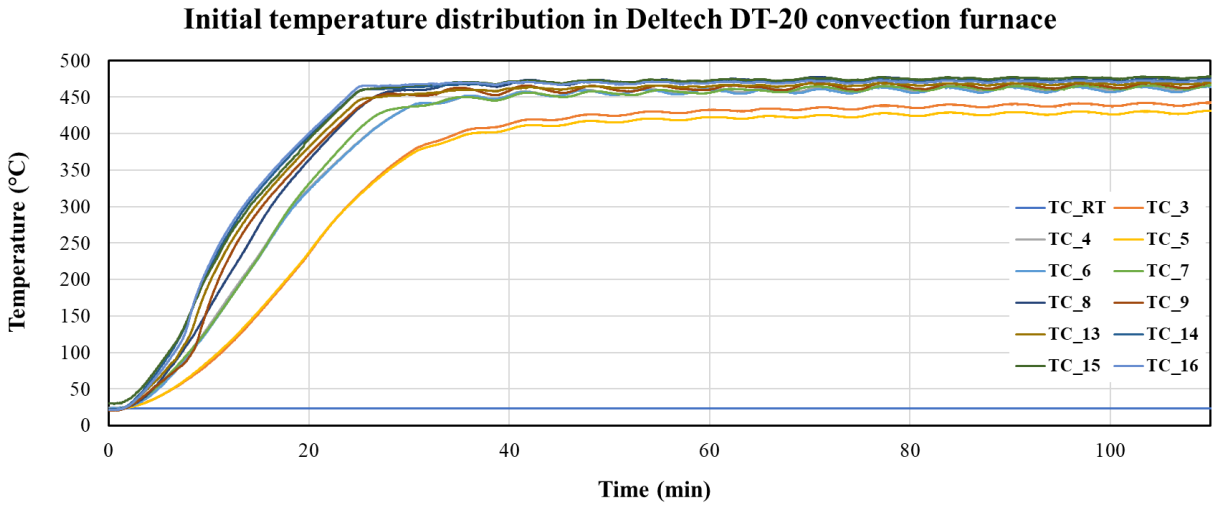

Figure 95. The Temperature history of the 'MiniMac' DT-20 furnace. The first 40 minutes denote the ramp-up period of the furnace from room temperature to the (roughly) steady-state target temperatures.

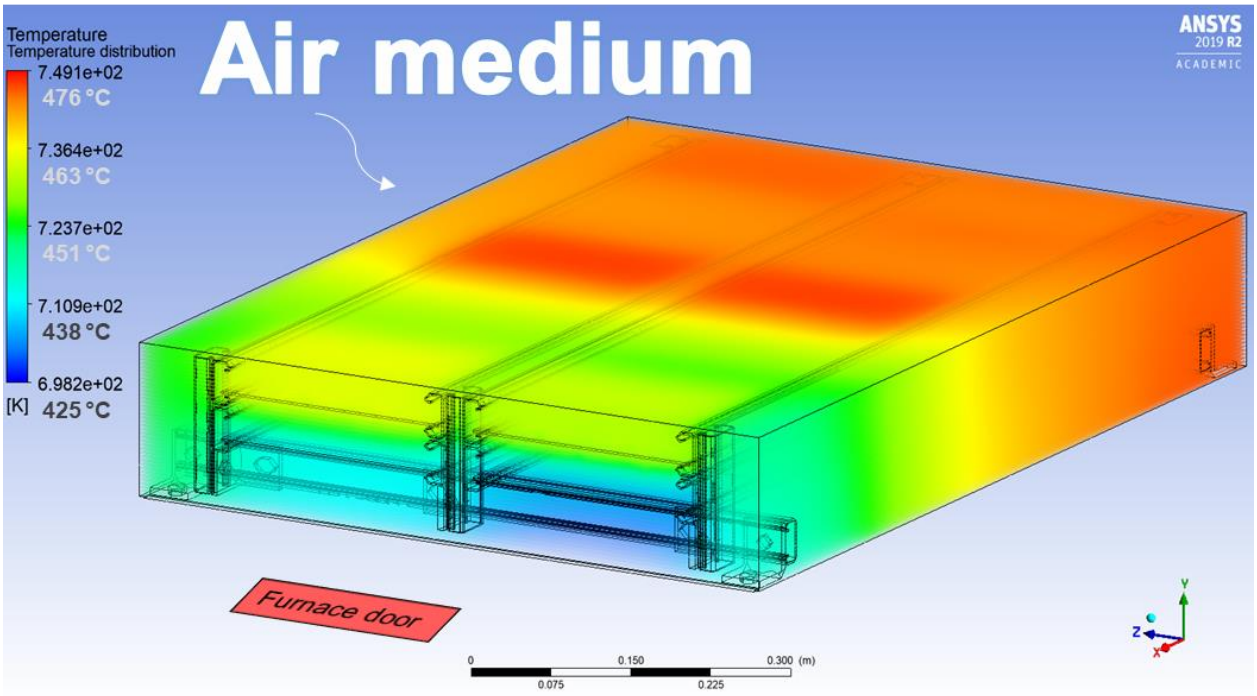

Figure 96. The average temperature distribution within the furnace, as obtained from reverse CFD analysis.

With improved thermal insulation and air circulation turned on a more uniform temperature distribution (from approximately 50 to 7 °C of temperature gradient) was observed near the centre of the furnace, as confirmed by the thermal history in Figure 97. This region was, therefore, utilized for batch heat-treatment processing of the Nakazima dome specimens.

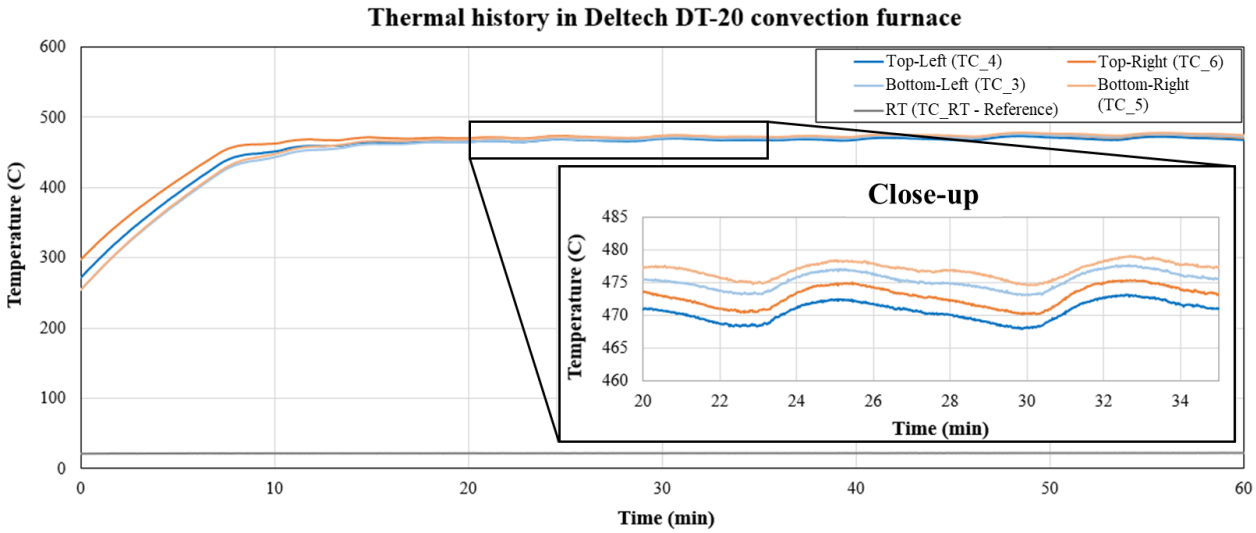

Figure 97. The improved temperature history of instrumented specimen between the front and centre of the furnace. As with all temperature history graphs, a room temperature (RT) thermocouple has been included to ensure proper connectivity of the data acquisition system's (DAQ's) input module. This thermocouple was placed in room temperature, close to the DAQ.

A.2. Temperature Uniformity in the Fluidized Sand Furnace.

The on-site Sand Furnace at the University of Waterloo has shown to provide the most stable and uniform stand-alone heat-treatment solution. To evaluate the stability, a thermocouple was sandwiched between two ASTM E8 tensile specimens, as shown in Figure 98. This instrumented sample was then placed in a typical heat treatment batch (of about 10 to 12 specimens per batch) and inserted into the Sand Furnace set to 475 °C.

Figure 98. Instrumented tensile specimens used in the Sand Furnace.

The resulting thermal response is shown in Figure 99. As can be seen, the steady state temperature is within 1 °C of the set target temperature.

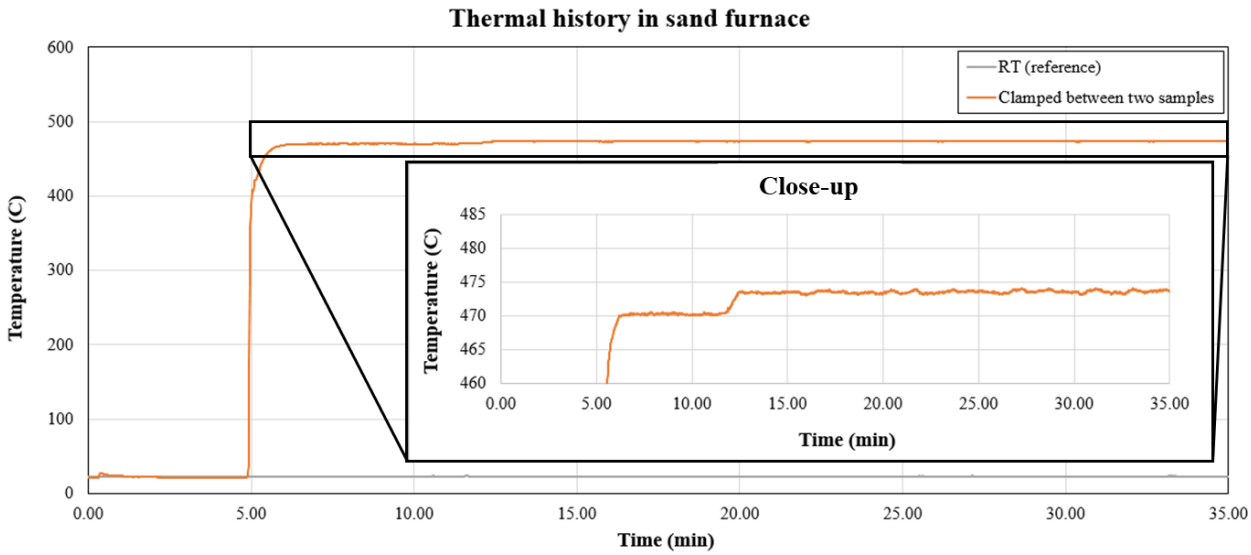

Figure 99. The thermal history of the probed specimens inside the Sand Furnace.

A shortcoming of this furnace was its small opening, which prevented larger (Nakazima dome) specimens from fitting in. Therefore, only the smaller (tensile) specimens were heat-treated using this apparatus.

A.3. Warm Forming System Furnace Validation

A.3.1. Furnace Settings

In order to achieve the prescribed (short) heating periods within the two furnaces, the furnace temperatures were set to exceed the desired specimen temperatures. The resulting specimen temperature histories are shown in Figures 100 and 101 for the convection (Deltech) and contact (Can-Eng) furnaces, respectively. The initial heating trials shown in these figures were utilized to determine the furnace temperature settings for each condition, through interpolation. The calculated furnace temperature settings are listed in Tables 8 and 9.

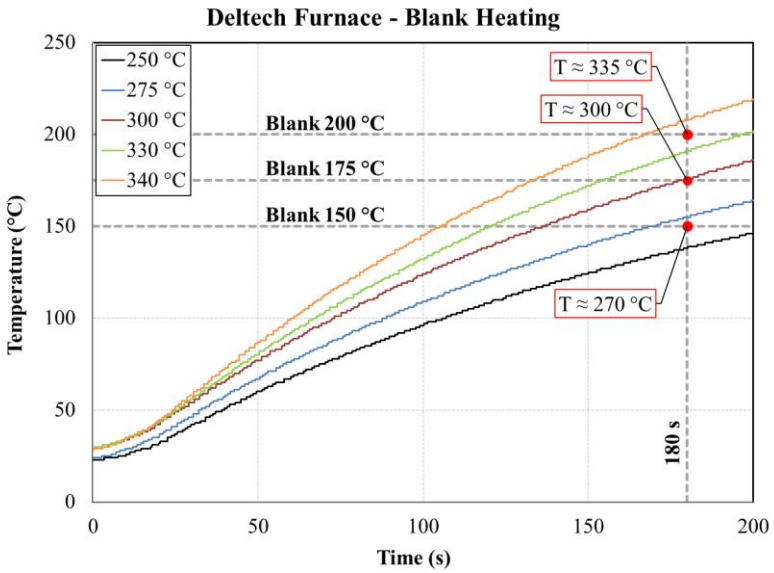

Figure 100. Measured specimen temperature-time histories for a range of furnace set point temperatures (legend) using the Deltech convection furnace. Interpolation between the specimen temperature curves determined the rough furnace set points for achieving the desired blank temperature at the target heating time of 180 s [108].

Table 8. Convection Furnace temperature settings corresponding to a heating time of 3 minutes [108].

Desired blank temperatures after 180 s in furnace	Set temperatures
150 °C	270 °C
175 °C	300 °C
200 °C	335 °C

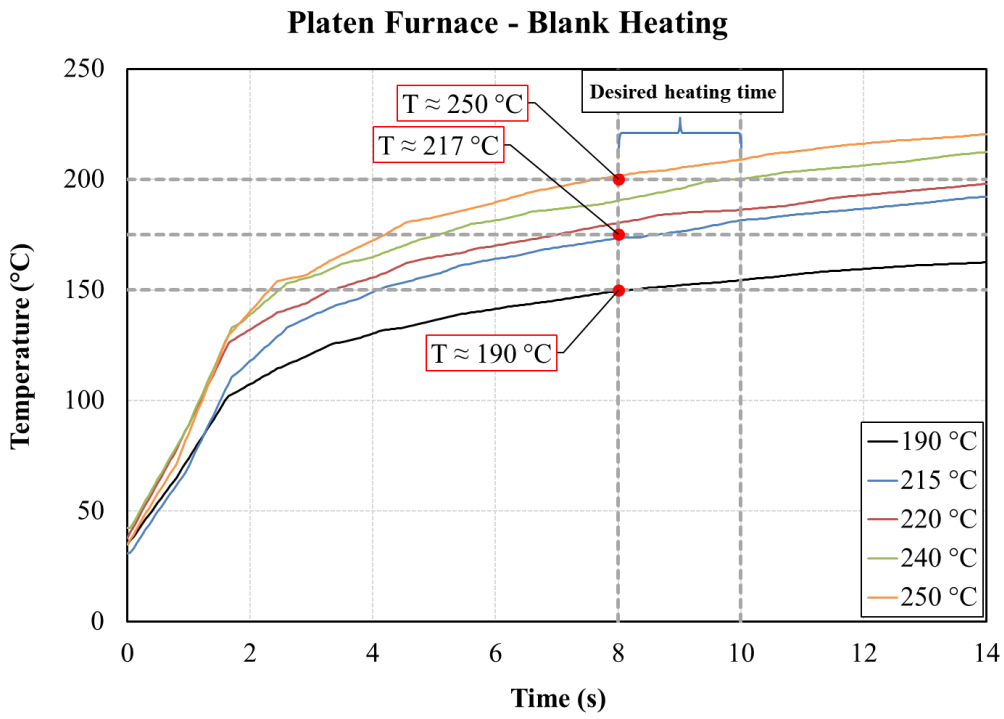

Figure 101. Measured specimen temperature-time histories for a range of furnace set point temperatures (legend) using the Can-Eng contact furnace. Interpolation between the specimen temperature curves determined the rough furnace set points for achieving the desired blank temperature at the target heating time of roughly 8 s [108].

Table 9. Conduction (platen) furnace temperature settings corresponding to a heating time of 8 seconds [108].

Desired temperatures	Set temperatures
150 °C	190 °C
175 °C	217 °C
200 °C	250 °C

A.3.2. Warm Forming *In Situ* Temperature Histories

The thermal histories of the specimens during the indicated forming condition in the Fast Forming System is shown in the following figures. These figures include the infrared (IR) pyrometer's thermal measurements of the specimen surface, as well as the temperatures of the heated die-set and the punch, utilizing their embedded thermocouple sensors. These graphs were used to define the process parameter in the numerical simulations.

The outer and inner thermocouples in the die-set correspond to the pair of sensors placed 6 mm from the contact surface, at different radial distances from the center of the die-set, with the inner being closer to the center of the specimen. The Punch thermocouple location is displayed in

Figure 39. Moreover, the die closure defined the limit of validity for the IR pyrometer, due to reflections. Therefore, all succeeding data were discarded for this specific sensor.

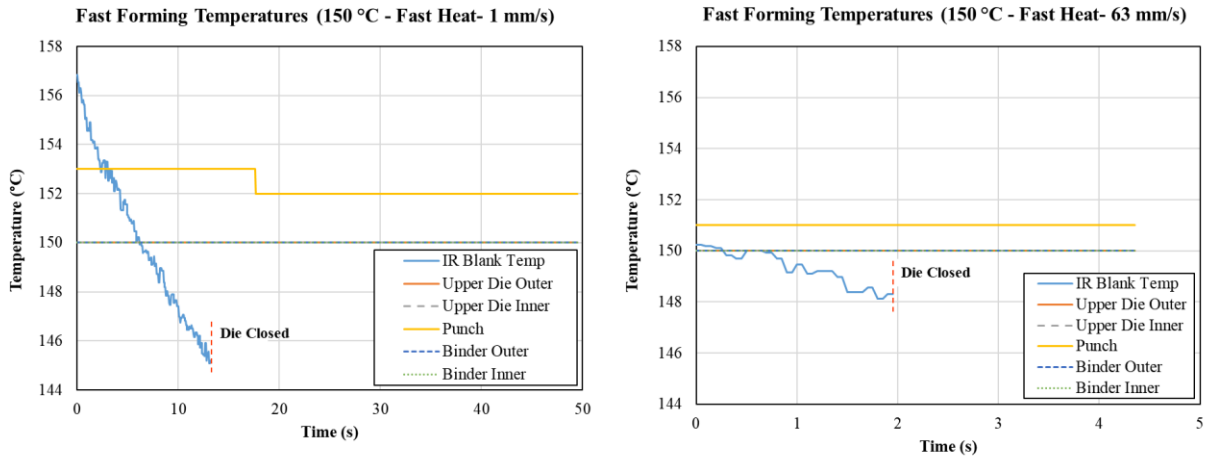

Figure 102. Warm forming cycle temperatures - 150 °C, Fast Heat.

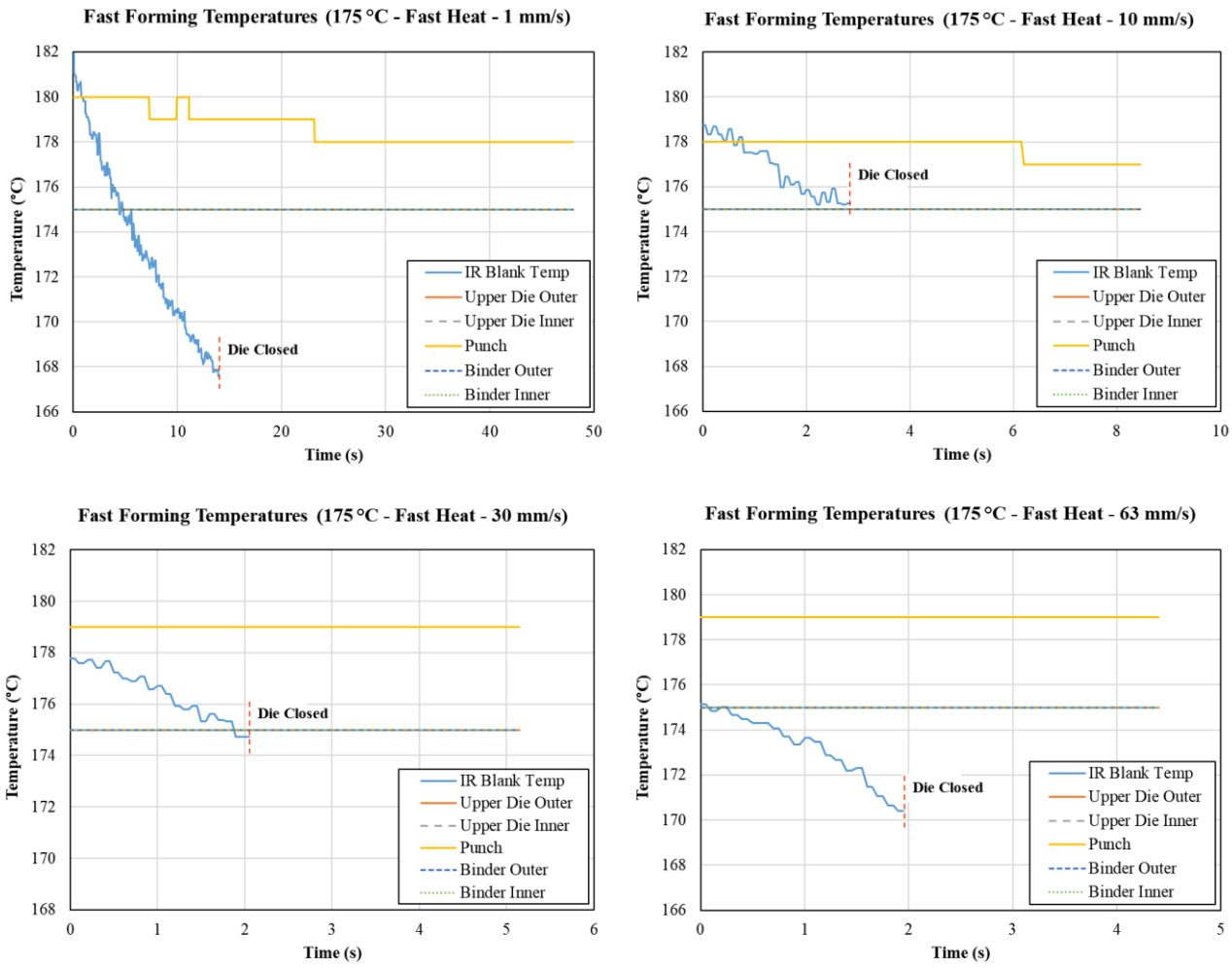

Figure 103. Warm forming cycle temperatures - 175 °C, Fast Heat.

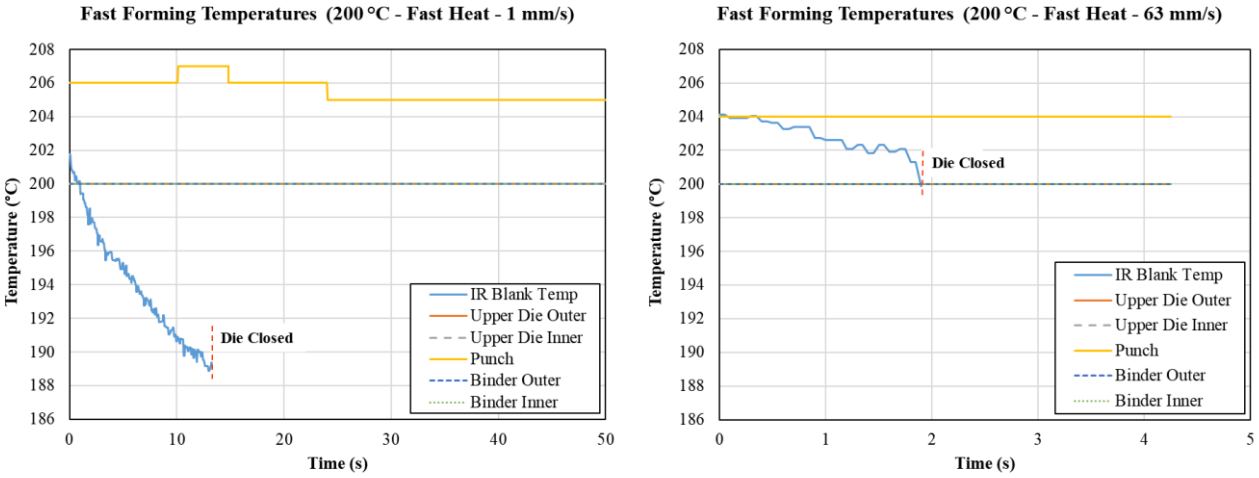

Figure 104. Warm forming cycle temperatures - 200 °C, Fast Heat.

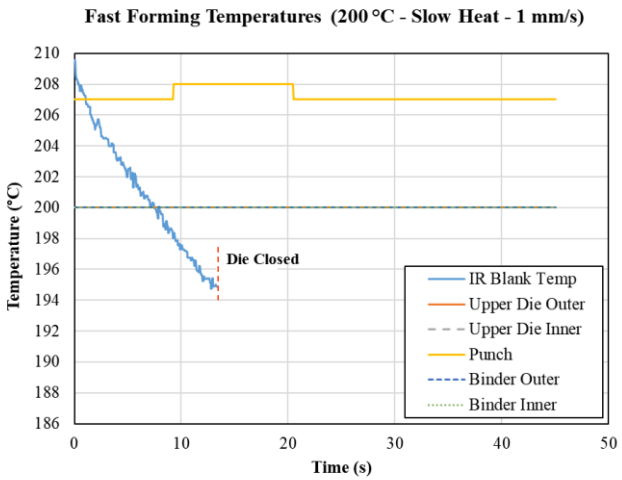

Figure 105. Warm forming cycle temperatures - 200 °C, Slow Heat.

B. Gleeble 3500 System Validation and Corrective Measures

B.1. Temperature Distribution

Given the excellent thermal conductivity of the aluminum specimens, conventional heat insulation methods, such as utilizing stainless steel grippers and minimizing the contact area, were not sufficient to maintain a uniform temperature distribution across the tensile specimen. As shown in Figure 106, a temperature drop of approximately 25 °C was observed across the small gauge length of 19.6 mm on an older (thermally optimized) tensile specimen geometry. This thermal gradient would further translate into a substantial strain non-uniformity within the gauge length, as illustrated in Figure 107.

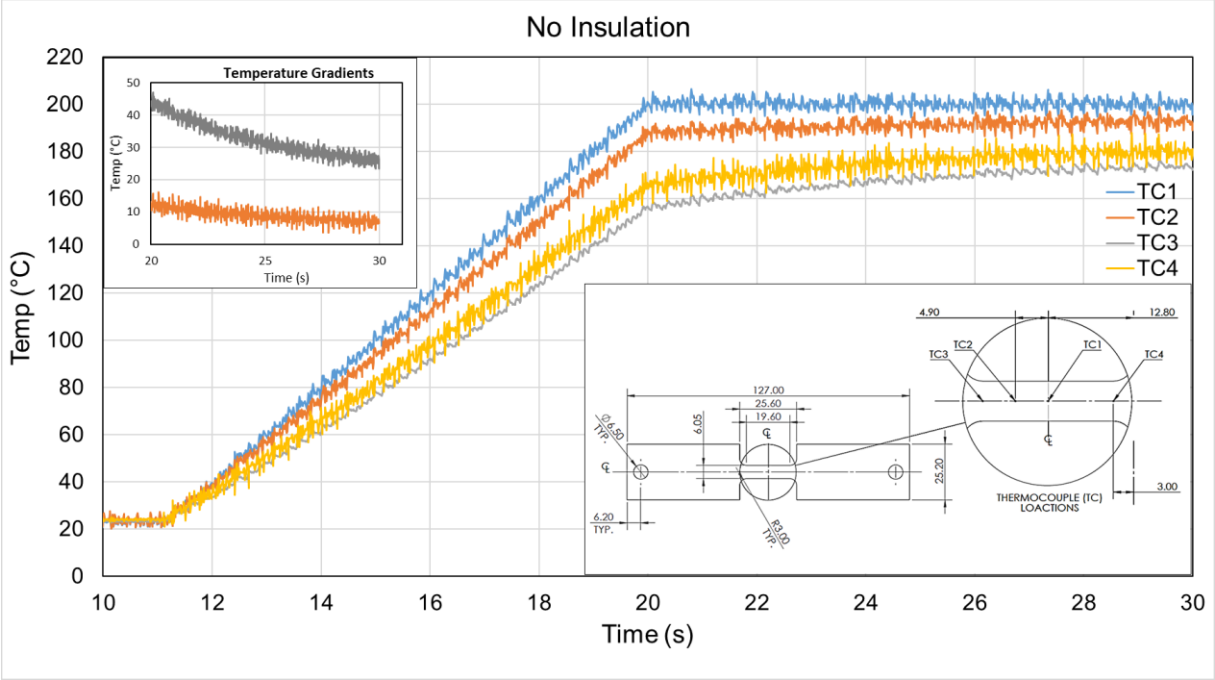

Figure 106. The thermal gradient across the initial specimen geometry with no insulation. Dimensions in mm.

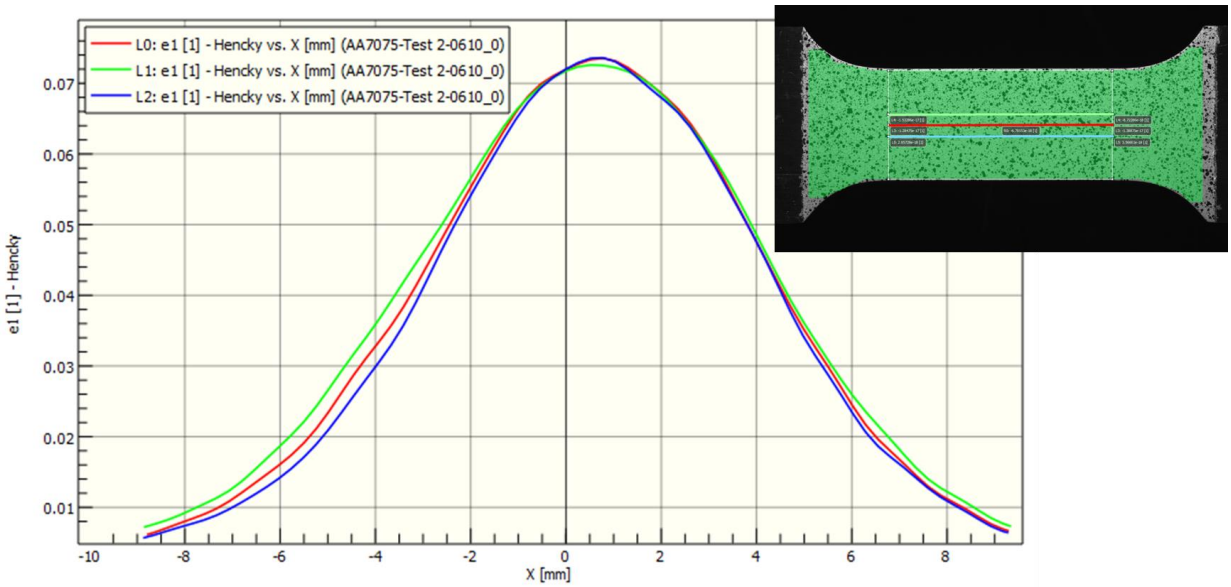

Figure 107. The strain distribution at UTS for a T6 specimen tested at the temperature of 200 °C and a strain rate of 0.01 s^{-1}, without insulation.

In order to reduce the variation in temperature across the specimen, a variety of gripper designs and materials, in addition to a number insulating materials were examined. The evaluation metrics used in this study were the overall thermal uniformity across the specimen and repeatability (which was an important factor as arcing across contact imperfections resulted in a large scatter in the data). The selected insulation was determined to be a thin sheet (0.4 mm) of white Muscovite, and the corresponding thermal gradient is shown in Figure 108. As illustrated, the thermal difference across the sample was reduced to approximately 5 °C, or 20% of the original value.

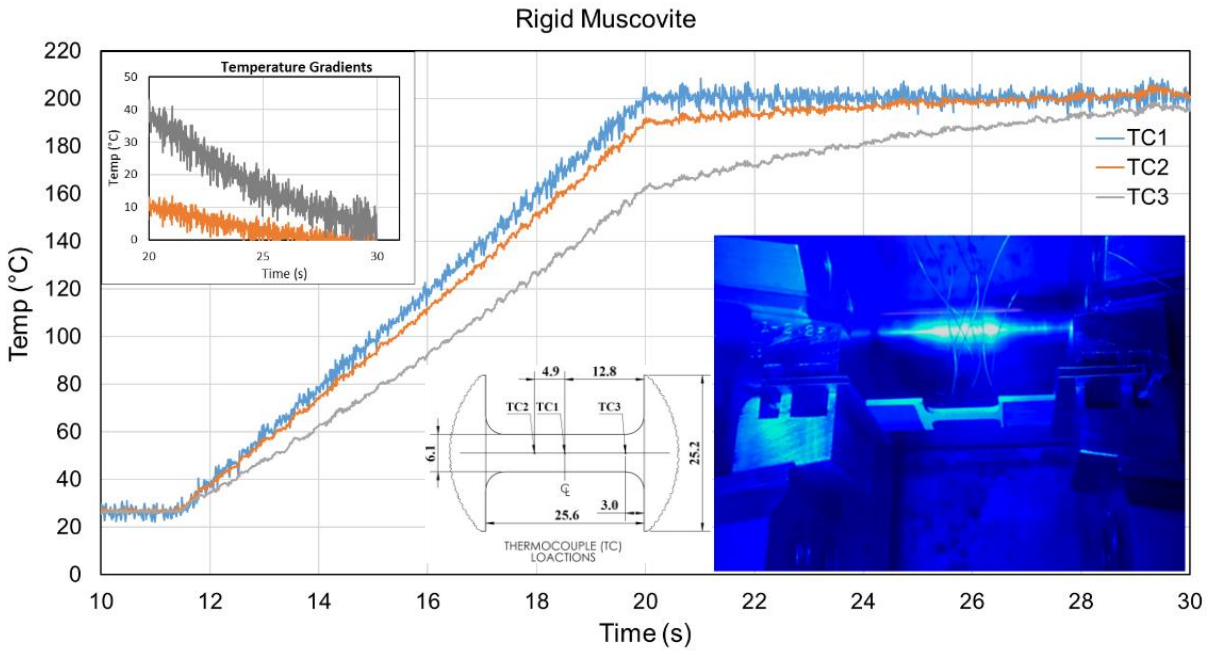

Figure 108. The thermal gradient across the initial specimen geometry with insulation. Dimensions in mm.

Moreover, a new geometry, developed in collaboration with Lu [107], was introduced in order to reduce the exaggerated bending effects within the small gauge region, produced by inherent alignment issues with the Gleeble apparatus. The new Gleeble specimen and the corresponding final gripper geometry (integrated into a nested gripper assembly designed by Lu [107]) are shown in Figures 36 and 109, respectively. This apparatus was used for the entirety of the warm constitutive characterization in this report.

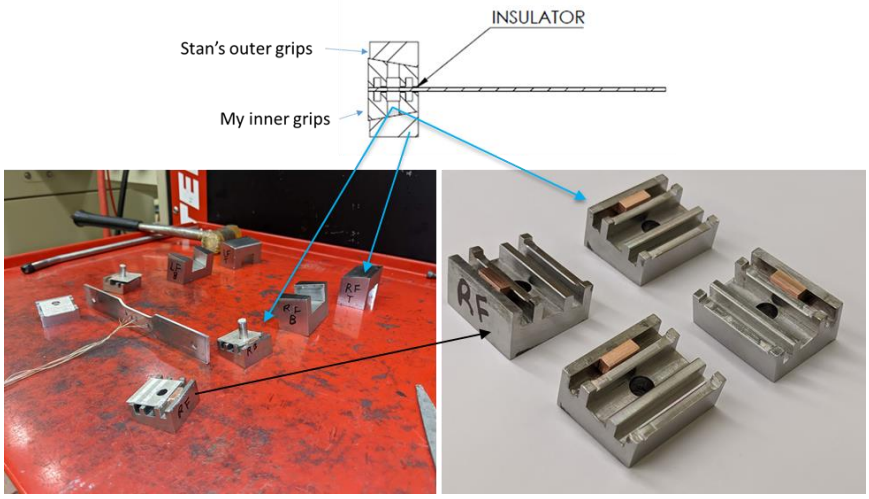

Figure 109. Gleeble specimen gripper and insulation subassembly.

The gauge length temperature distribution of the instrumented Gleeble specimen, shown in Figure 109, during a tensile test at a temperature of 200 °C and strain rate of 0.01 s^{-1}, is shown in Figure 110. The strain distribution for this condition is shown in Figure 111.

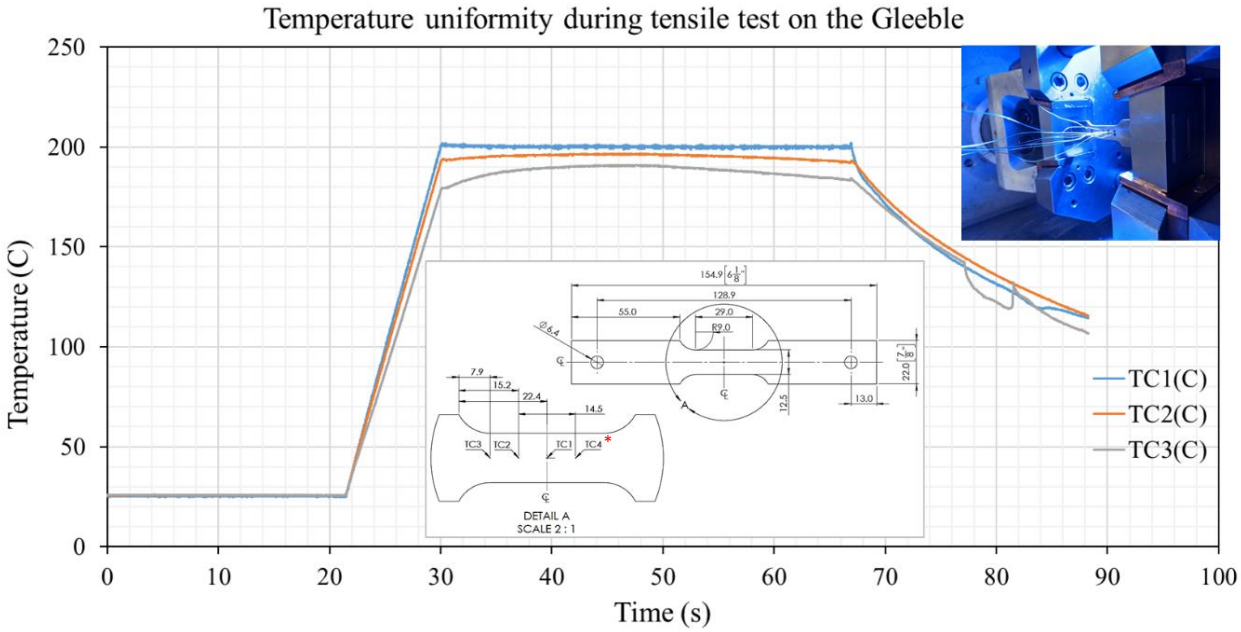

Figure 110. The thermal history of an instrumented specimen during a 200 °C test.
**Note: The fourth thermocouple, symmetric to TC2 had failed to record due to an input error.*

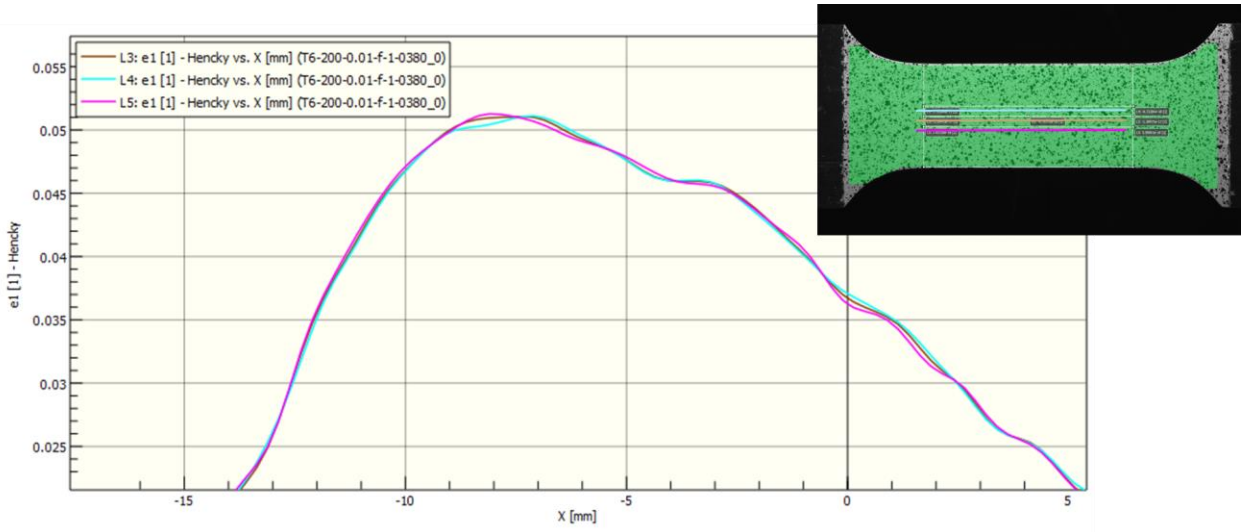

Figure 111.The strain distribution at UTS for a T6 specimen tested at the temperature of 200 °C and a strain rate of 0.01 s^{-1}, using insulation.

B.2. Area Reduction Method (ARM) Validation Approach

Although the strain uniformity was significantly improved by addressing the temperature gradient across the specimen, this issue was not completely resolved. Therefore, two solutions were proposed. The first was to reduce the region of interest (ROI) as shown in Figure 112. However, the concern with this approach was the consistency between various test conditions with different severity in strain gradients, and operator dependency error.

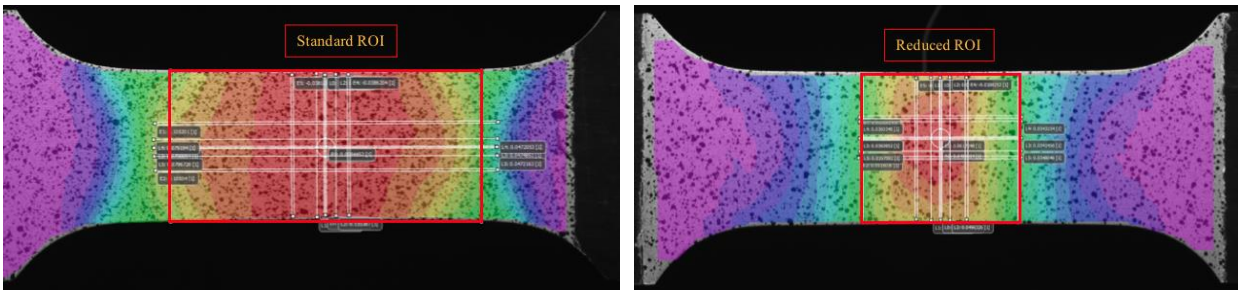

Figure 112. The reduced region of interest (ROI) due to the strain gradient in the gauge region.

An alternative approach was to use the novel area reduction method (ARM) proposed by Omer *et al.* [72], in which the local strains at the fracture point were used to evaluate the constitutive characteristics of the alloy. Nevertheless, this method also had its limitations, which were addressed by Omer *et al.* [72] and are validated with the existing dataset.

The two concerns, as discussed in Section 2.2.3, were the rapid increase in strain rate and the deviation of the strain path from a linear path, near the end of the local necking region. Similar to Omer *et al.*'s [72] approach, the data extraction was limited by physical limitations on achievable strain rates (which correspond to the deviations in strain paths) as illustrated in Figure 113.

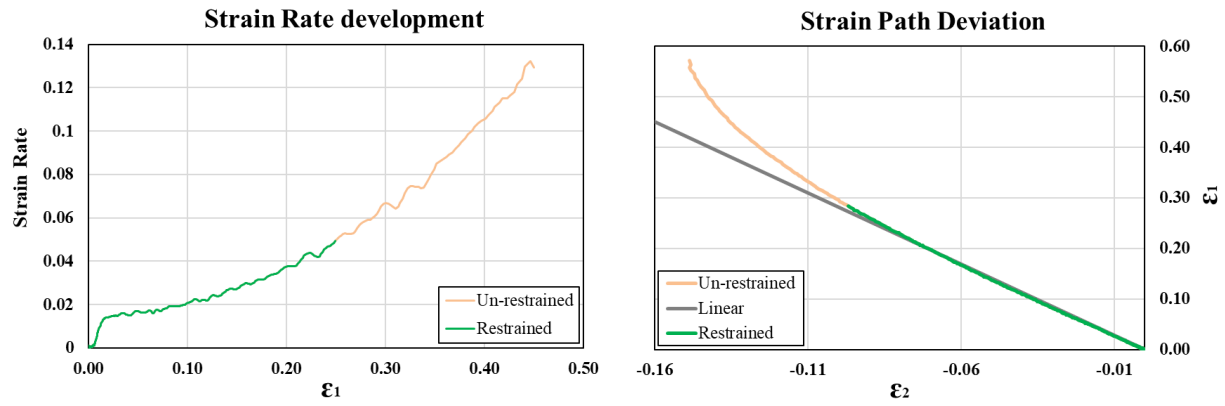

Figure 113. The Strain rate jump [Left, and Strain Path [Right] corresponding to the fast heating and slow forming (0.01 s^{-1} SR) of a T6 temper formed at 200 C

Furthermore, the extracted flow stress response obtained from the ARM was overlaid on top of the results obtained from the conventional data extraction method (using virtual strain gauges in the DIC VIC-3D software). Figure 114 shows the excellent correlation from the yield point up to the UTS limit.

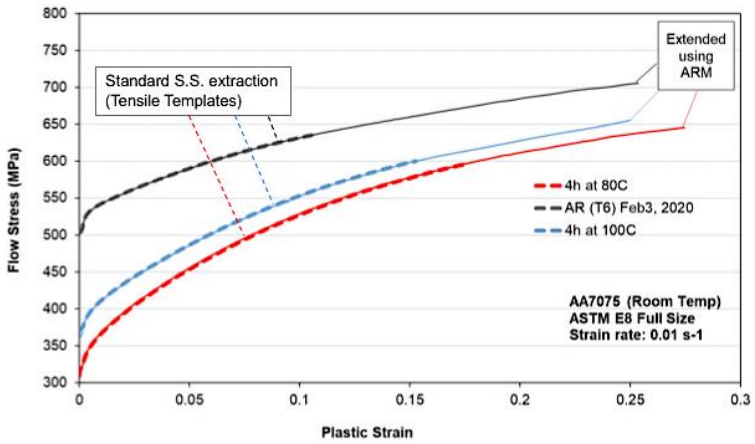

Figure 114. The flow curves of three different tests obtained from ARM versus the conventional (virtual strain gauge) method.

Finally, the analytical dimensions of the fractured section obtained from the ARM were compared to those measured using a Keyence VHX 5000 optical microscope. The errors were calculated to be < 2%, as shown below:

The average measured width for the ductile condition (80C-4h at 200 °C), as shown in Figure 115, was calculated as:

$$AVG_{Measured\ width} = \frac{11.072 + 10.925}{2}$$

$$\approx 11.00\ mm$$

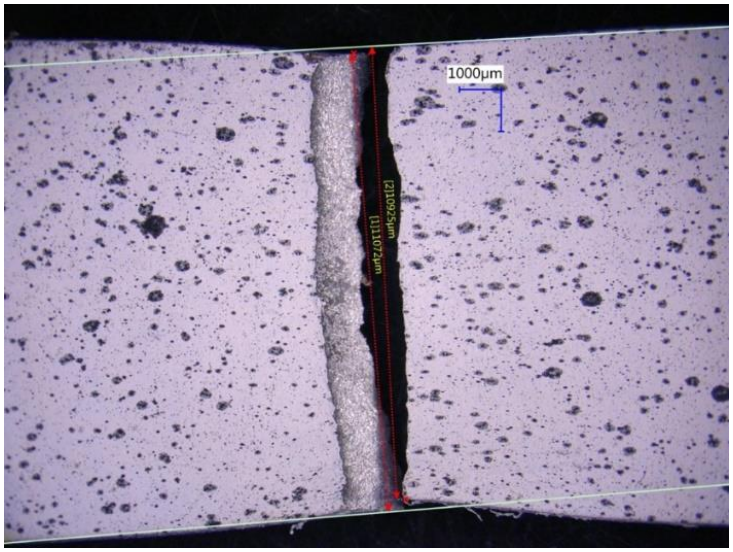

Figure 115. Optical measurements of the specimen's fractured width.

Moreover, the width approximation from the ARM was found as:

$$AVG_{ARM\ width} = Width_{DIC} * Widt\ Correction\ Factor \approx 10.89\ mm$$

Where, $Width\ Correction\ Factor = \frac{Initial\ Width_{Measured}}{Initial\ Width_{Detected\_by\_DIC}}$

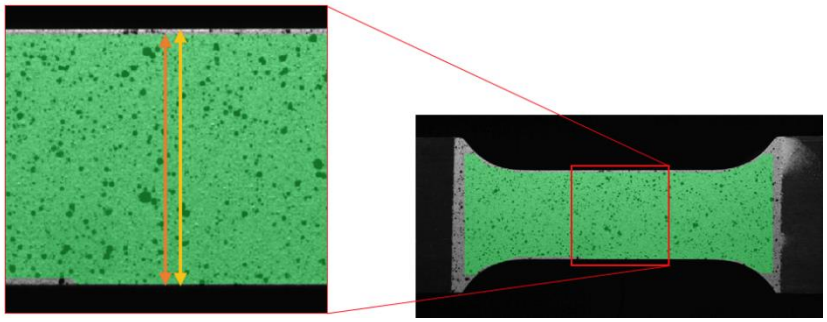

Figure 116. The width correction factor diagram.

Therefore, the error was calculated to be:

$$\%Error = \frac{AVG_{ARM\ width} - AVG_{Measured\ width}}{AVG_{Measured\ width}} \approx \mathbf{-0.95\%}$$

Similarly, the error in thickness prediction was found as:

$$\%Error = \frac{AVG_{DIC\ Thickness} - AVG_{Measured\ Thickness}}{AVG_{Measured\ Thickness}} = \mathbf{-1.92\%}$$

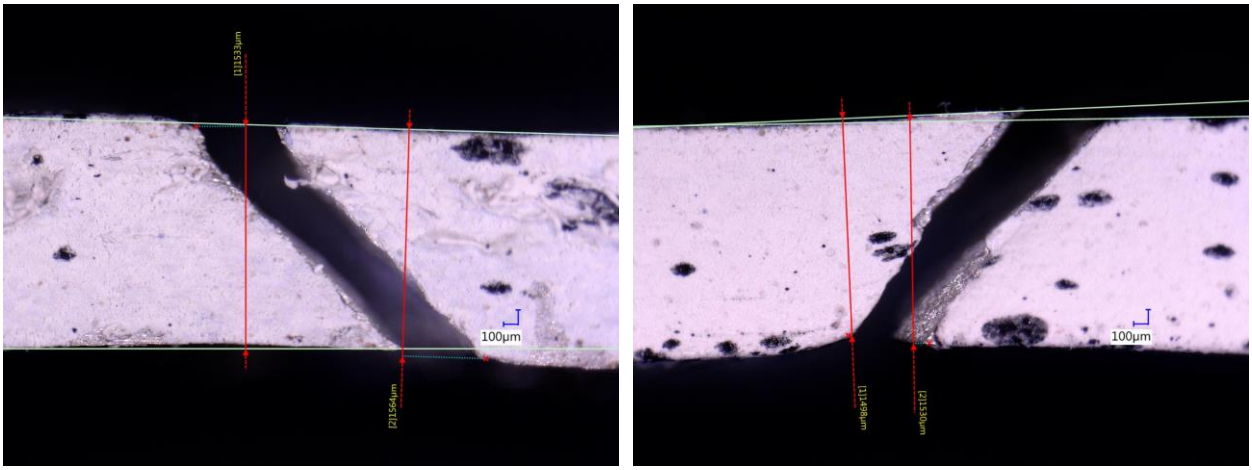

Figure 117. Optical measurements of the specimen's fractured thickness.

B.3. Noisy Load Signal

The Gleeble apparatus did not include an external load output for the DIC system, since this was a part of a module purchased separately. The signal from available analog output ports contained a significant amount of undesired electromagnetic noise induced by the resistive heating circuit of the Gleeble setup, as shown in Figure 118.

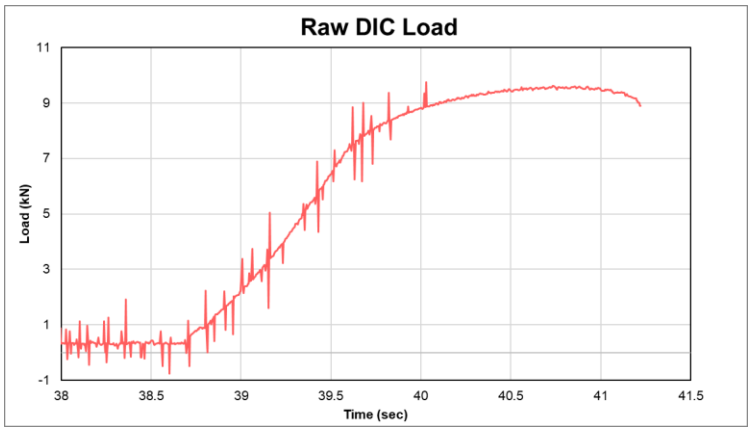

Figure 118. Raw load data obtained from the unfiltered Gleeble auxiliary ports by the DIC system.

There was, nevertheless, an output file for each test in the Origin software on the Gleeble computer (integrated with the Gleeble controls software), as shown in Figure 119. The data extracted from the Gleeble computer exhibited a substantial reduction in noise, given an acquisition rate harmonized with the power frequency of the heating circuit.

However, a few inconsistencies between the two data sources existed. First and foremost, the time scales were not synchronized. This concern was addressed using statistical regression correlations from the much cleaner stroke data, as shown in Figures 120 and 121. The second concern was the load magnitude correction factor that, although close, did not match the accuracy obtained from the original Gleeble data (red dotted line). Therefore, it was necessary and advantageous to make use of the existing data from the Gleeble PC.

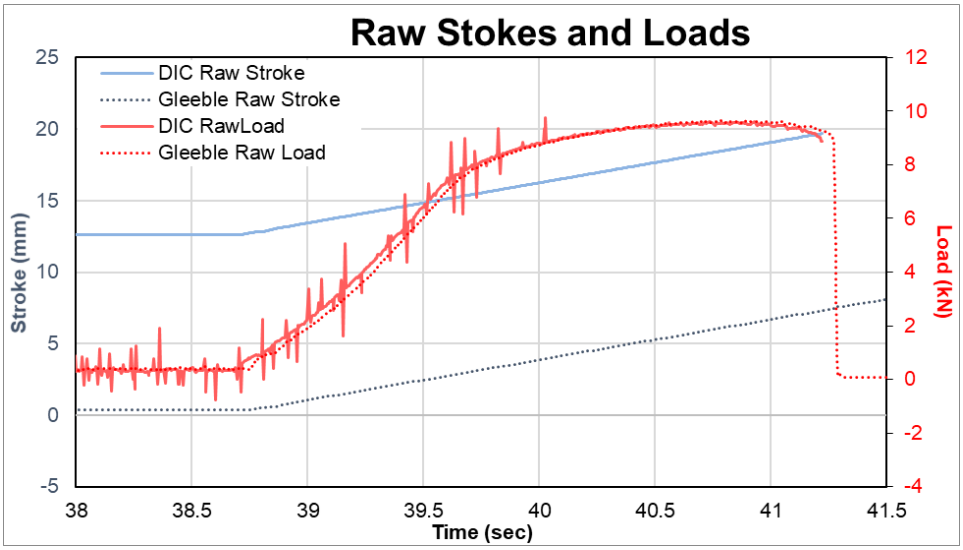

Figure 119. Raw outputs obtained by the DIC system from the unfiltered auxiliary ports on the Gleeble machine, and the filtered signals obtained from the Gleeble computer.

The synchronization was achieved by merging the interception of the two pairs of lines (overlaying the raw stroke data), as shown in Figure 120. The two lines labelled as ① are the linear best fits corresponding to the inclined region for each of the two data sources. The other two lines labelled as ② represented the local stationary region immediately before the start of the tensile test. The criteria used to identify this region were comprised of the co-occurrence of the lowest first derivative values (for a selection of neighbouring data points) that also display the highest regression correlation coefficient (R^2), as shown in Figure 121.

Aligning the intersection of the two pairs of lines yielded proper synchronization, independent of sampling frequency from either the DIC or Gleeble DAQs.

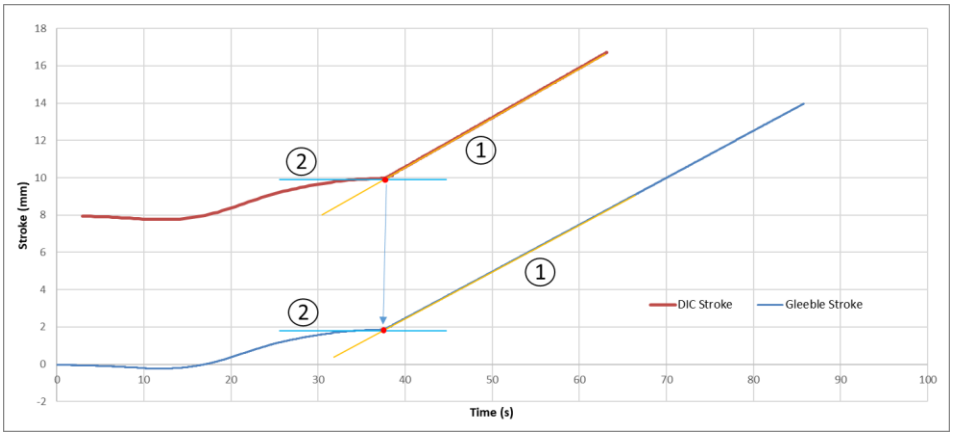

Figure 120. The illustration of the synchronization method using stroke data obtained from the unfiltered auxiliaries and the filtered data on the Gleeble PC.

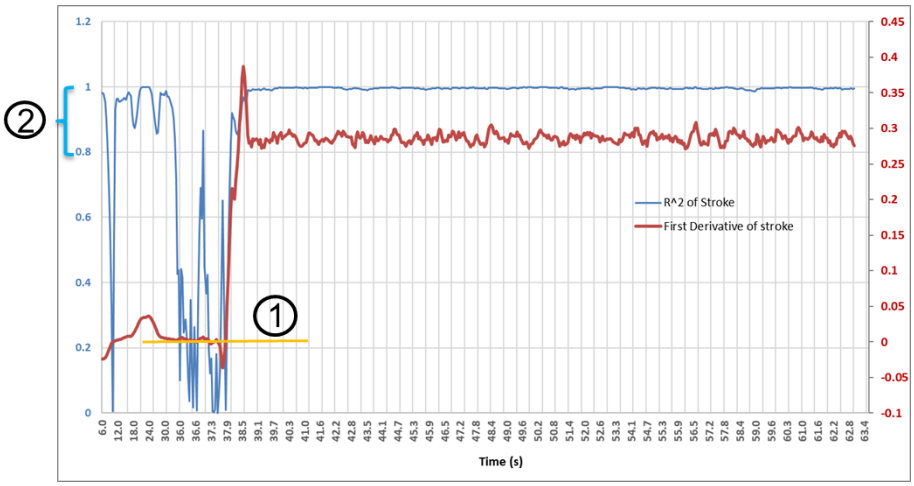

Figure 121. The statistical regression and first derivative conditions employed for the detection of the local static region prior to the start of a tensile test.

A final step to verify the synchronization results was carried out by means of a user interface window where manual adjustments were made, as shown in Figure 122. The final result of this synchronization technique is presented in Figure 123, overlaying the initial (noisy) load curve. The small error caused by the approximate load scale factor is also apparent in this figure.

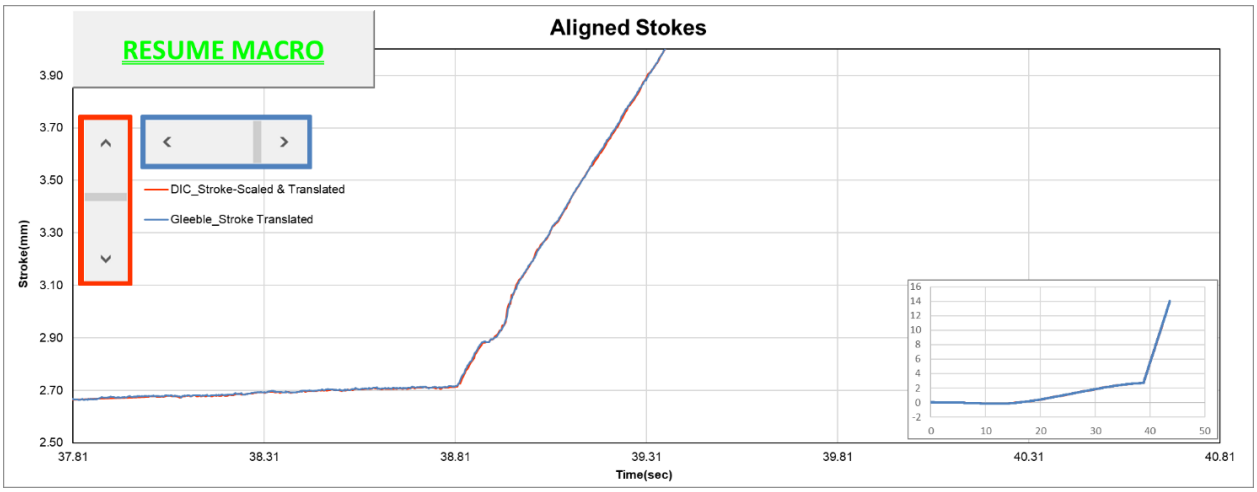

Figure 122. The user interface window for verifying and tweaking the synchronized data.

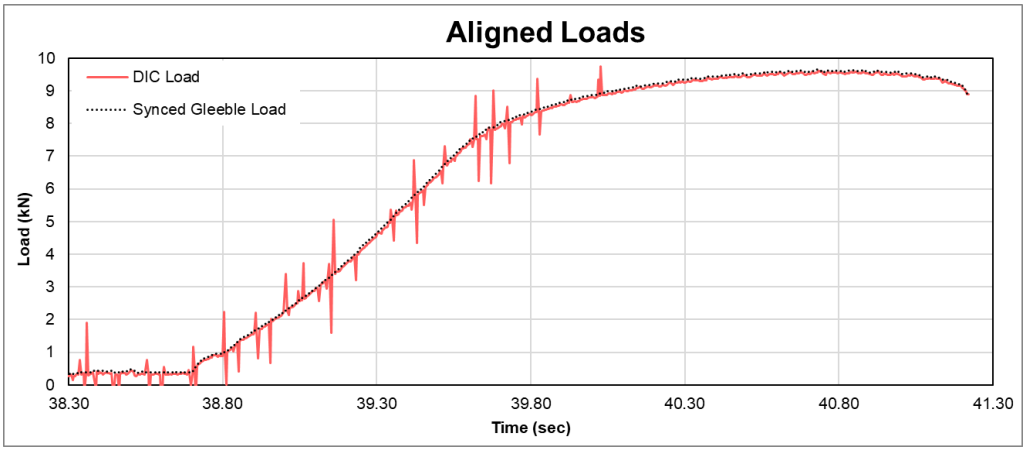

Figure 123. The synchronized filtered load curve, overlaying the initial noisy curve.

The synchronized load data was further smoothed, given the larger number of samples from the higher sampling frequency of Gleeble DAQ, using a 5 point weighted moving average method (see Figure 124).

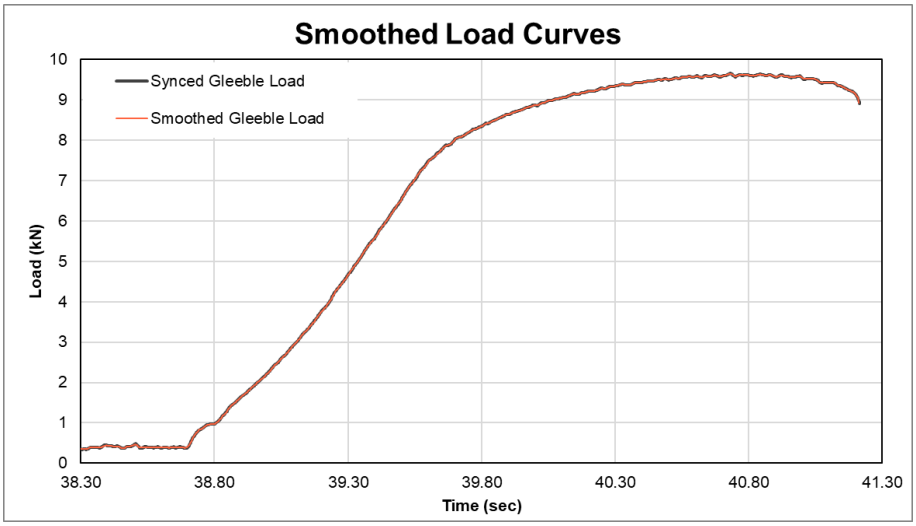

Figure 124. The 5-point weighted moving averaging of the load curve.

The extracted data combined with the DIC images were used to determine the appropriate constitutive behaviour of the specimens on the Gleeble setup.

B.4. Thermocouple Welding Effects on the Aging Kinetics of Specimens

The close loop thermal control system utilizes thermocouples spot-welded at the centre of the specimen. One concern was the heat treatment that some of the highly unstable specimens may go through. For this reason, two thermocouples were pre-welded to the specimen to evaluate the temperature spike caused by the welding process. One is welded right at the back and one right beside (1mm) the region of interest. The thermal response for a typical thermocouple welding process (which occasionally takes up to two attempts) is displayed in Figure 125.

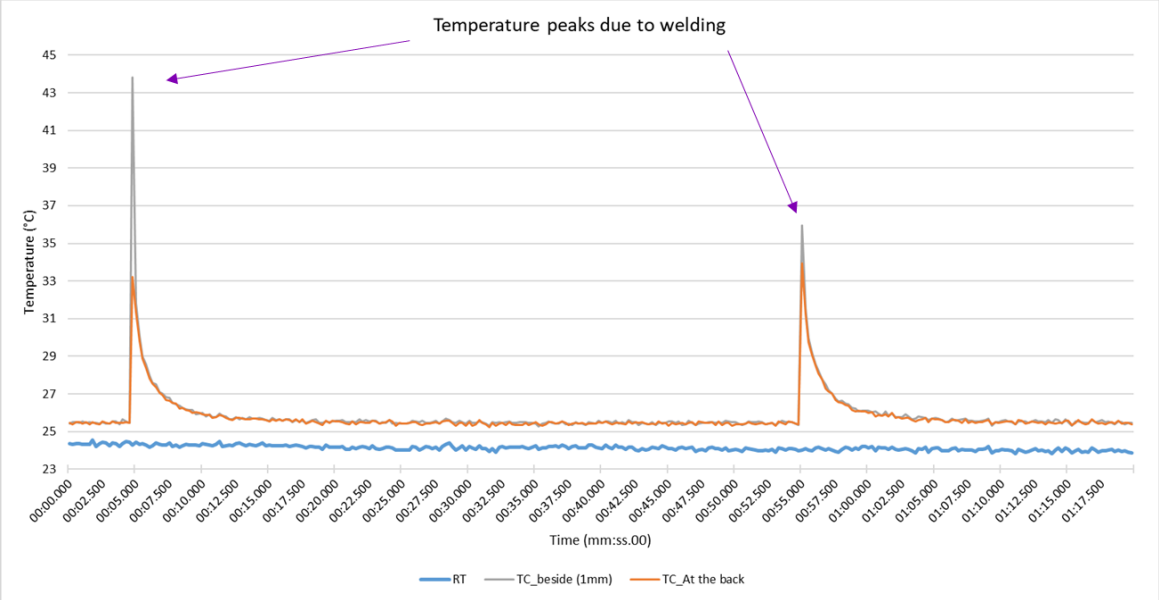

Figure 125. The thermal history of a Gleeble specimen during the thermocouple welding process

Therefore, given the short period and the relatively low peak temperatures, negligible aging was assumed at this spot.

C. Verification of the Modulus of Elasticity (E)

The yield point calculation requires the determination of the Young's modulus (E) which is examined in this appendix. Figure 126 [Left] is a scatter plot of the early (low-strain) stress-strain response for the median cases of all tested conditions, which highlights the extremes of the strengths considered in the constitutive modelling effort. This data was used to extract the slope of the elastic portion of the outlying curves – which have shown to deviate from the typical (or assumed) room temperature modulus [103]. These slopes correspond to the measured values of Young's Modulus as summarized in Figure 126 [Right] (black line with orange markers). In general, there is a reduction in modulus with increased test temperature, and reduced pre-aging. Also shown in the right hand figure are the estimated yield strengths that were calculated using the measured and assumed (71 GPa) moduli for the outlier conditions (orange and blue bars, respectively).

It was found that the difference in yield strengths calculated using the assumed *versus* the measured moduli resulted in a maximum error of less than 4%. Further, the errors pertaining to the elastic strains were determined to be less than 15% of the total elastic strains. However, given that the total plastic strains are all less than 1% strain (Figure 126 [Left]), it is not known whether this error is due to the natural scatter of the data or due to a real phenomena. It should be noted that although more accurate elastic moduli can be obtained using other advanced techniques such as piezo-electric sensors [116], the DIC approximations were deemed sufficient for this simple demonstrative study. Nevertheless, in spite of these small errors (specifically in the yield strengths, if the assumed modulus was to be used across all conditions), the measured moduli of elasticity were employed for all outlying cases.

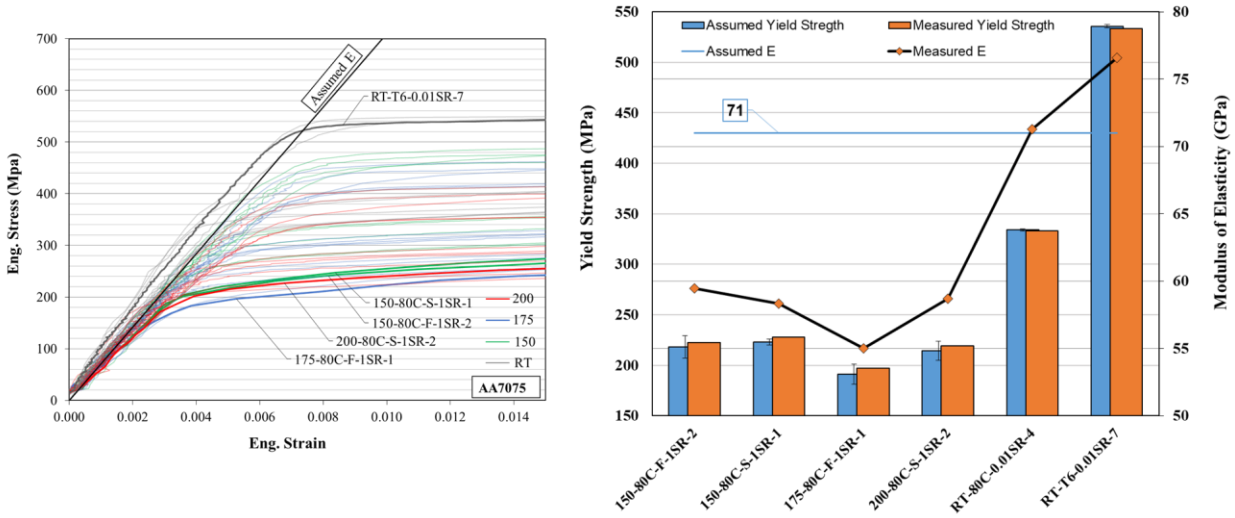

Figure 126. Evaluation of the elastic moduli for the outlying tempers. [Left] Demonstration of the variance in the elastic response for the various tempers. [Right] The comparison of the Assumed and Effective elastic moduli. Note that for the case of RT-T6, the slower strain rate data were used (as representative data) since the reduced scatter, and the larger number of data points provided a higher level of confidence with the calculated, or measured E.

D. Warm Forming Selection Criteria – Application of the Gleeble Constitutive Data

In order to narrow down the search for ideal forming conditions, a set of indicators were utilized. Such indicators were derived from the constitutive response of the alloy; these include: a) the uniform and total elongations (Figure 66), b) the instantaneous work hardening rate (WHR), c) the degree of work hardening (difference between the UTS and the yield strength), and d) the instantaneous work hardening exponent (n). The work hardening rates and exponents, b) and d), are graphically shown in Figures 127 and 128, while a) and c) can be obtained numerically, and therefore, can be measured quantitatively.

The quantitative measures and their combined responses were considered to rank and select the desired process routes. The different strain rate sensitivity results (when available) for each temper, heating rate, and test temperature was also considered in this comparison to provide a more informed prediction of forming performance for the different conditions.

Furthermore, the instantaneous work hardening responses were utilized as a graphical assessment of formability and are presented in Figure 127. The highlighted curves in this figure represent the conditions with the generally higher WHR, inspired by the aforementioned quantitative rankings. These selections group the data obtained at the different strain rates for each of the thermally treated states together. This is done to portray a more complete image of the expected forming response.

As shown, the pre-aged conditions take advantage of a higher extent of work hardening (areas under the curves) and the instantaneous WHR – especially at higher plastic strains, resisting the rapid growth of local necks. The sub-figure in Figure 127 displays the engineering curves corresponding to the lowest strain rate tests of each of these conditions.

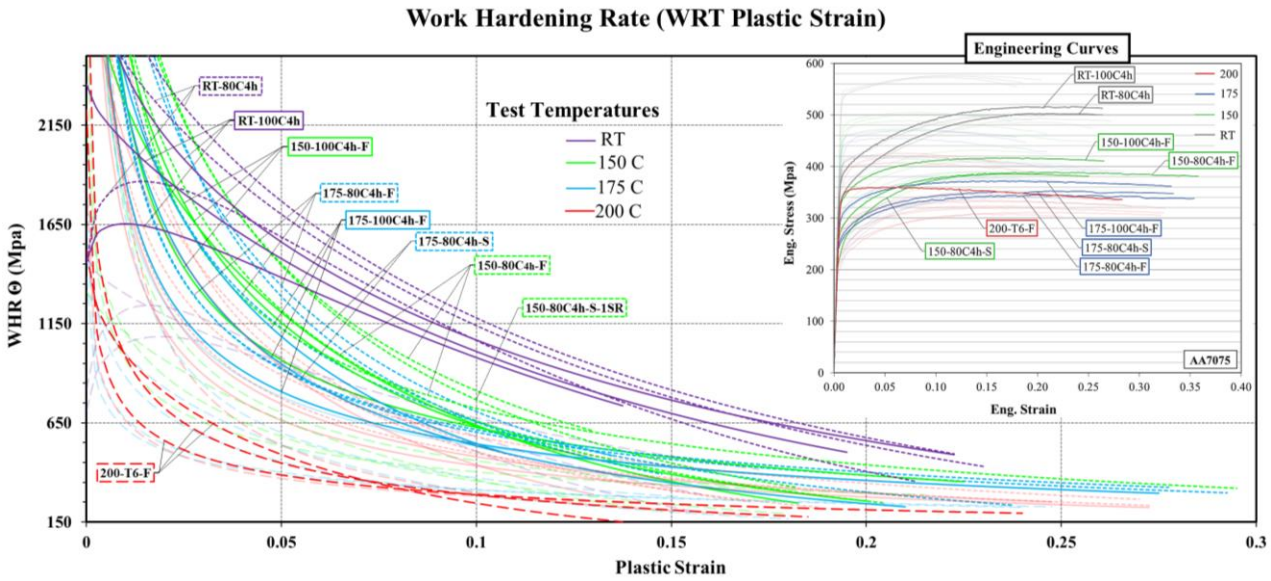

Figure 127. The work hardening response of the conditions tested on the Gleeble machine, with the conditions of interest highlighted.

It should be noted that although the grouping of strain rates is meant to identify the better pre-aged condition, the final precipitation aging states are not uniform across the specimens tested at different strain rates. The slower tests allowed a longer period of aging during deformation, as previously discussed.

The instantaneous strain hardening exponent as defined by Eq [2] for each of the selected conditions were plotted and evaluated in Figure 128. From this graph, it can be seen that although the n-values (work hardening exponents) are significantly lower for the case of T6, the steady increase of this variable helps with the elongated and extended necking region. The results for the two strain rates of 0.01 and 1 s^{-1} (when available) were utilized in the calculations to capture the effects of strain rates.

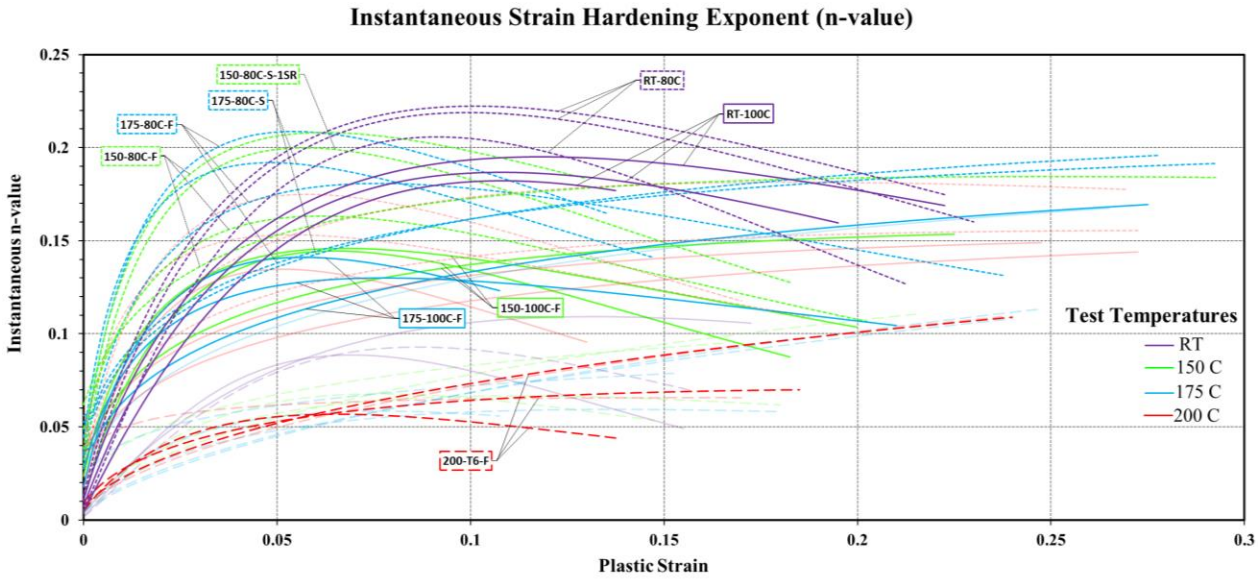

Figure 128. The instantaneous strain (work) hardening exponent history with respect to the plastic major strain for the selected tempers.

The process routes evaluated on the Gleeble apparatus are ranked and listed Table 10. Only the top 15 conditions were considered, in order to reduce the warm forming test matrix to a reasonable size. Further, the last column of this table normalizes the combined effects of work hardening potential and total elongation, with respect to the yield strength, in order to favor conditions with lower yield stresses. The rationale behind each selection is listed in the second column of this table.

Table 10. Quantitative measures for process route evaluation.

		Ranking in each metric & numeric values (Units)			
Condition	**Selection rationale**	Total e1	$(\mathrm{UTS}-\mathrm{YS})_{0.01+1\,SR}$ (MPa)	$((\mathrm{UTS}-\mathrm{YS})\times \mathrm{e1})_{0.01+1\,SR}$ (MPa)	$\left((\mathrm{UTS}-\mathrm{YS})\times \frac{\mathrm{e1}}{\mathrm{YS}}\right)_{0.01+1\,SR}$
RT-T6	Evaluated for reference.	14 (18)	11 (65.4)	14 (1191)	14 (2.2)
RT-80C4h	Great formability at RT	11 (26.4)	1 (297.4)	1 (7719)	5 (22.5)
RT-100C4h	Good formability at RT (selected for reference)	13 (26.4)	6 (239.2)	6 (5741)	6 (15)
150-80C4h-F	Excellent formability with reduced YS	1(35.8)	3 (280.3)	3 (7231)	2 (29.4)
150-80C4h-S	Beneficial HT during WF – Great formability (considering single SR of 1/s)	4 (21.3)	2 (162.3)	2 (3454)	3 (15.5)
150-100C4h-F	Repeatable	12 (26.6)	7 (191.8)	7 (4574)	11 (14)
150-100C4h-S	For reference	NA	NA	NA	NA
175-80C4h-F	Excellent formability with reduced YS	2 (35.4)	5 (251.5)	4 (6755)	1 (31.2)
175-80C4h-S	Beneficial HT during WF	3 (33.4)	4 (251.6)	5 (6515)	4 (29.3)
175-100C4h-F	Very repeatable, decent formability	5 (24.7)	8 (176.7)	8 (4138)	8 (14.2)
175-100C4h-S	Beneficial HT during WF – stable flow and large e1 (considering single SR of 0.01/s)	7 (31.5)	13 (72)	9 (2262)	10 (7.5)
200-100C4h-F	Stability - Reduced formability – stiff flow curve	8 (29.2)	9 (153)	10 (3724)	7 (14.2)
200-100C4h-S	Beneficial HT during WF stable and large e1 (considering single SR of 0.01/s)	6 (32.5)	14 (63.5)	11 (2066)	9 (7.62)
200-T6-F	Evaluated for reference. Excellent post UTS elongation.	9 (28.3)	12 (61.8)	13 (1423)	13 (4.2)
200-T6-S	Evaluated for reference.	10 (28)	10 (106)	12 (2379)	12 (7)